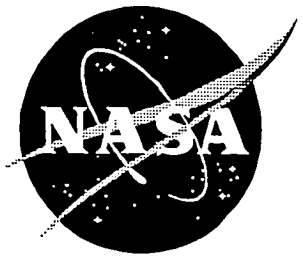

NASA Conference Publication 3314

NASA-CP-3314 19960003449

Second Annual Research Center for Optical Physics (RCOP) Forum

Edited by
Frank Allario and Doyle Temple

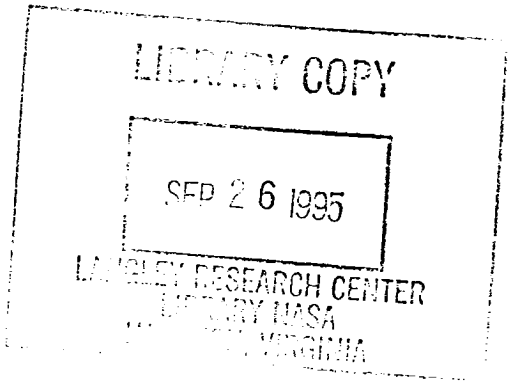

Proceedings of a forum jointly sponsored by the National Aeronautics and Space Administration, Washington, D.C., and Hampton University, Hampton, Virginia, and held in Hampton, Virginia
September 23–24, 1994

October 1995

NASA Conference Publication 3314

Second Annual Research Center for Optical Physics (RCOP) Forum

Edited by
Frank Allario
Langley Research Center • Hampton, Virginia

Doyle Temple
Hampton University • Hampton, Virginia

Proceedings of a forum jointly sponsored by the National Aeronautics and Space Administration, Washington, D.C., and Hampton University, Hampton, Virginia, and held in Hampton, Virginia September 23–24, 1994

National Aeronautics and Space Administration
Langley Research Center • Hampton, Virginia 23681-0001

October 1995

This publication is available from the following sources:

NASA Center for AeroSpace Information
800 Elkridge Landing Road
Linthicum Heights, MD 21090-2934
(301) 621-0390

National Technical Information Service (NTIS)
5285 Port Royal Road
Springfield, VA 22161-2171
(703) 487-4650

EXECUTIVE SUMMARY

The Research Center for Optical Physics (RCOP) held its Second Annual Forum on September 23–24, 1994. The forum consisted of two days of technical sessions with invited talks, submitted talks, and a student poster session. Dr. Demetrius Venable, Executive Vice President and Provost, delivered the welcome and opening remarks. He gave a brief history of the research programs in the physics department and their relationship to RCOP. Following the opening remarks, Dr. Frank Allario, Chairman of the Technical Advisory Committee, gave the technical overview of the collaboration between RCOP and NASA Langley; Dr. Doyle Temple, Director of RCOP, gave a review of technical programs in RCOP and the mission of the program.

Participants in the technical sessions included students and researchers from CCNY/CUNY, Fisk University, Georgia Institute of Technology, Hampton University, University of Maryland, the University of Michigan, NASA Langley Research Center, North Carolina A&T State University, Steven's Institute of Technology, and NAWC-Warminster. A speech by Dr. Lynwood P. Randolph, the Manager of Information Standards at NASA Headquarters, highlighted the closing of the banquet. This document is a compilation of the invited and contributed talks and student posters.

Sincere thanks go to Hampton University faculty and staff for their outstanding assistance in organizing the forum and to participating NASA personnel for their support and cooperation. Without their efforts the forum would not have been a success. Also, special recognition goes to all the students for their excellent presentations. Lastly, we greatly appreciate the NASA staff responsible for the publication of these proceedings.

Frank Allario
Chief, Information Systems Division
Langley Research Center

Doyle Temple
Director, Research Center for Optical Physics
Hampton University

Lee Lillard
Administrative Chairman
Information Systems Division
Langley Research Center

CONTENTS

Executive Summary iii

Controlling Chaotic Lasers 1
Zelda Gills and Rajarshi Roy

Actively Pumped Optical Filters at 532 nm 11
Richard I. Billmers, S.K. Gayen, Vincent M. Contarino, William J. Scharpf, Martin F. Squicciarini, and David A. Allocca

Subpicosecond Third Order Nonlinear Response in Polythiophene and Thiopene Based Thin Films 21
D. Harris, E. Royer, and R. Dorsinville

Crystal Growth and Spectroscopy of Diglycine 29
Taravia M. Taylor

Laser-Induced Photochromic Centers in Ce^{3+}:$La_2Be_2O_5$ 37
Y.M. Cheung, S.K. Gayen, and D.M. Gualtieri

Aggregation-Enhanced Raman Scattering by a Water-Soluble Porphyrin 45
Daniel L. Akins

Superradiance of J-Aggregated 2,2´-Cyanine Adsorbed onto a Vesicle Surface .. 59
Daniel L. Akins and Serdar Özçelik

Spectroscopic Investigation of Ce^{3+} Doped Fluoride Crystals 81
Donald H. Reinhart, Jr., Guzin Armagan, Waverly Marsh, James Barnes, and B.H.T. Chai

Study of Luminescence Characteristics of Trivalent Terbium in Silicate Glass 89
Mike S. West, Guzin Armagan, and William P. Winfree

Radiative and Nonradiative Transitions of the Rare-Earth Ions Tm^{3+} and Ho^{3+} in $Y_3Al_5O_{12}$ and LiYF4 99
Brian M. Walsh, Guzin Armagan, Baldassare Di Bartolo, and Edward A. Modlin

Thermal Line Shift and Broadening of Ho^{3+} in $Y_3Al_5O_{12}$ and $Lu_3Al_5O_{12}$ 109
Elizabeth R. Snoke, Guzin Armagan, Gary W. Grew, Norman P. Barnes, and Brian M. Walsh

CONTROLLING CHAOTIC LASERS

Zelda Gills and Rajarshi Roy
School of Physics
Georgia Institute of Technology
Atlanta, Georgia 30332-0430

INTRODUCTION

Irregular fluctuations in intensity have long plagued the operation of a wide variety of solid-state lasers. We are exploring the possibility of exploiting rather than avoiding a laser's chaotic output. As an important step in that direction, we have applied a novel control technique to stabilize a solid state laser. By making small periodic changes in only one input parameter of the laser, we are able to stabilize complex periodic waveforms and steady state behavior in the laser output. We demonstrate the application of this approach in a diode pumped Nd:YAG laser system.

CONTROLLING CHAOTIC LASERS

In recent years, chaotic intensity fluctuations have been identified in a number of laser systems [1-4]. The challenge now is to learn how to control, and perhaps even exploit, the chaotic behavior. "Control" refers to achieving periodic or stable output from a chaotic system without changing the parameters of the system, or the system itself, in a permanent way; only small time-dependent perturbations about the ambient parameter values are allowed.

Work done by Ott, Grebogi, and Yorke (OGY) in 1990 was a breakthrough in this direction and has been applied experimentally to a periodically driven magnetoelastic ribbon [5-6]. The basic concept involved in the OGY algorithm is that a chaotic attractor--the geometrical object toward which a system's trajectory in phase space converges--has a large number of unstable periodic orbits embedded in it. It should therefore serve as a rich source of complex periodic wave forms, if an appropriate dynamical control technique can be implemented to stabilize the system. Using occasional proportional feedback (OPF)--a variant of the OGY approach, Earle Hunt (Ohio University) developed an analog circuit to control a chaotic diode resonator circuit [7]. The name arose from the fact that the feedback consisted of a series of perturbations of limited duration dt ("kicks") delivered to the input drive signal at periodic intervals (T) in proportion to the difference of the chaotic output signal from a reference value.

In this paper, we describe application of the OPF technique to an autonomously chaotic multimode laser, a higher dimensional system not characterizable by a two-dimensional map. Further, application of the control signal is performed on relatively fast time scales of the order of a few microseconds. In these circumstances, the OPF scheme provides an attractive means to attempt control of an autonomously chaotic laser. Though the OPF scheme does not require any detailed model of laser operation, a knowledge of the relaxation oscillation frequency-- the characteristic time scale of energy exchange between the active medium and the light in the laser cavity--was important for its implementation in this system.

The laser used in our experiments is a diode-laser-pumped solid-state Nd-doped yttrium aluminum garnet (Nd:YAG) system that contains a KTP (potassium titanyl phosphate) doubling crystal within a cavity of length ~ 3.5 cm (Fig. 1). This system has been studied extensively and the equations that describe the laser operation in several longitudinal modes are well known [8-10]. However, in the experiments reported here, it was not necessary to utilize a detailed model of the system. The laser was pumped at 60 mW, about 3 times above threshold (~ 20 mW), and the chaotic operation was observed for a given rotational orientation between the YAG and KTP crystals [9]. At this level of excitation, the laser operates in anywhere from five to ten longitudinal modes, depending on the rotational orientation of the crystal and length of the laser cavity.

The Nd:YAG laser operates in a stable steady state without the intracavity doubling (KTP) crystal which is used to generate green light (532 nm) from the system. The source of chaotic behavior in this laser is the coupling of the longitudinal modes through the nonlinear process of sum-frequency generation. This process destabilizes the relaxation oscillations which are normally heavily damped in a system without the intracavity crystal. Autocorrelation functions of the infrared intensity (1064 nm) reveal clear oscillations at the relaxation oscillation frequency even when the laser is chaotic [10]. Alternatively, one may discern a peak at the relaxation oscillation frequency in a fast Fourier transform (FFT) of the total intensity fluctuations.

The basic technique for achieving dynamical control is as follows. The laser intensity was detected with a fast photodiode and this signal provided the input for the control circuit. The output of the control circuit modified the injection current of the diode laser used to pump the Nd:YAG crystal. This seemed to be the most natural and convenient choice of control parameter. To adapt Hunt's circuit for control of the

autonomously chaotic laser, we had supplied an external timing signal from a function generator. This determined the interval T between "kicks" applied to the pump laser injection current. Although there was no external periodic modulation responsible for the chaotic dynamics, the relaxation oscillations of the laser intensity provided a natural time scale for perturbative corrections. The interval between kicks was thus adjusted to be roughly at the relaxation oscillation period (approximately 100 kHz), or a fractional multiple of it. The OPF algorithm is shown schematically in Fig. 2. The four parameters of the control circuit are: the period T, duration of the kicks dt, reference level I_{ref}, which measures the deviation of the signal, and the proportionality factor p, which determines the amplitude of the kicks.

The results of application of OPF to the laser were quite remarkable [11]. We were able to demonstrate stabilization of a large variety of periodic waveforms with perturbations of a few percent applied to the pump laser injection current. A typical chaotic waveform, together with several periodic waveforms stabilized in this way, is shown in Fig. 3. The control signal fluctuations are shown above the intensity waveforms. The particular waveforms stabilized can be selected by changes of control circuit parameters, mainly the time period T and the reference level I_{ref}. We note here that the laser had to be operated so as to generate very little green light for the control circuit to work successfully; the laser is "weakly" chaotic in this regime. If a significant amount of green light was generated, and the laser was highly chaotic, the circuit was unable to stabilize the laser.

We have also stabilized steady state behavior in the laser output using OPF. It is of great relevance for practical applications that a stabilized steady state be maintained. Steady state behavior is obtained by adjustment of the reference level to the mean of the chaotic fluctuations and the period T to match the relaxation oscillation period. The control voltage fluctuations become extremely small once the steady state is controlled. In Fig. 4 is shown the transient behavior of the laser intensity fluctuations as they are reduced to small fluctuations about the steady state as well as the control signal fluctuations during the stabilization process.

If the control parameters are fixed and the pump power of the laser is increased or decreased after the steady state is stabilized, the control signal fluctuations increase rapidly, and control is lost as the laser goes into periodic or chaotic oscillations. Clearly, one needs to change the control circuit parameters as the laser pump power is changed. A procedure called "tracking" accomplishes this change of control parameters in a systematic fashion. We applied such a tracking procedure to our laser; the control circuit parameters are varied so as to minimize the control signal fluctuations at each value of the pump power, which is increased in small increments. Our experiment was an illustration of the general algorithms for tracking periodic orbits developed recently by Ira Schwartz and his colleagues at the Naval Research Laboratory [12-13]. We were able to show that a combination of stabilization and tracking could maintain a stable steady state (Fig. 5) as the laser pump power is increased from threshold (21 mW) to more than three times above threshold (about 80 mW) [14]. Without the control circuit, the laser intensity went into periodic oscillations at a pump power of about 25 mW, and then into chaotic fluctuations, etc., as indicated in the figure by open circles and crosses.

In conclusion, we have demonstrated dynamical control of an autonomously chaotic, higher-dimensional optical system for the first time on microsecond time scales. The multimode laser system studied is an example of a globally coupled system of nonlinear oscillators. The proportional control signal applied to the pump excitation results in stabilization of both a rich variety of periodic orbits and the steady state. The results reported here indicate that the technique of occasional proportional feedback should be

widely applicable to a variety of physical, chemical, and biological systems, including arrays and networks or coupled elements.

Acknowledgments: Z. Gills is supported by an AT&T Bell Laboratories Graduate Fellowship. R. Roy acknowledges support from the National Science Foundation Grant ECS-9114232.

References

1. McMackin, I. *et al.*: Instabilities and chaos in a multimode, standing-wave, CW dye laser. *Phys. Rev.*, vol. A36, 1988, pp. 320-332.

2. Sacher, J. *et al.*: Intermittency in the coherence collapse of a semiconductor laser with external feedback. *Phys. Rev. Lett.*, vol. 63, 1989, pp. 2224-2227.

3. Arecchi, F. T. *et al.*: Experimental evidence of subharmonic bifurcations, multistability, and turbulence in a Q-switched gas laser. *Phys. Rev. Lett.*, vol. 49, 1982, pp. 1217-1219.

4. Winful, H. G. *et al.*: Frequency locking, quasiperiodicity, and chaos in modulated self-pulsing semiconductor lasers. *Appl. Phys. Lett.*, vol. 48, 1986, pp. 616-618.

5. Ott, E. *et al.*: Controlling chaos. *Phys. Rev. Lett.*, vol. 64, 1990, pp. 1196-1199.

6. Ditto, W. L. *et al.*: Experimental control of chaos. *Phys. Rev. Lett.*, 1990, pp. 3211-3214.

7. Hunt, E. R.: Stabilizing high-period orbits in a chaotic system: The diode resonator. *Phys. Rev. Lett.*, vol. 67, 1991, pp. 1953-1955.

8. James, G. E. *et. al.*: Elimination of chaos in an intracavity-doubled Nd:YAG laser. *Opt. Lett.*, vol. 15, 1990, pp. 1141-1143.

9. Wiesenfeld, K. *et. al.*: Observation of Antiphase States in a Multimode Laser. *Phys. Rev. Lett.*, vol. 68, 1992, pp. 1259-1262.

10. Bracikowski, C.; and Roy, R.: Chaos in a multimode solid-state laser system. *Chaos*, vol. 1, 1991, pp. 49-64.

11. Roy, R. *et. al.*: Dynamical control of a chaotic laser: Experimental stabilization of a globally coupled system. *Phys. Rev. Lett.*, vol. 68, 1992, pp. 1259-1262.

12. Schwartz, I. B.; and Triandaf, I.: Tracking unstable orbits in experiments. *Phys. Rev.*, vol. A46, 1992, pp. 7439-7444.

13. Carroll, T. *et. al.*: Tracking unstable orbits in an experiment. *Phys. Rev.*, vol. A46, 1992, pp. 6189-6192.

14. Gills, Z. *et. al.*: Tracking unstable steady states: Extending the stability regime of a multimode laser system. *Phys. Rev. Lett.*, vol. 69, 1992, pp. 3169-3172.

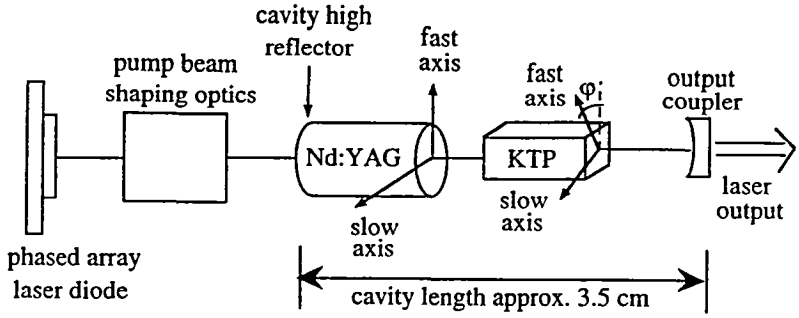

Figure 1. Diode pumped, intracavity frequency doubled Nd:YAG laser system.

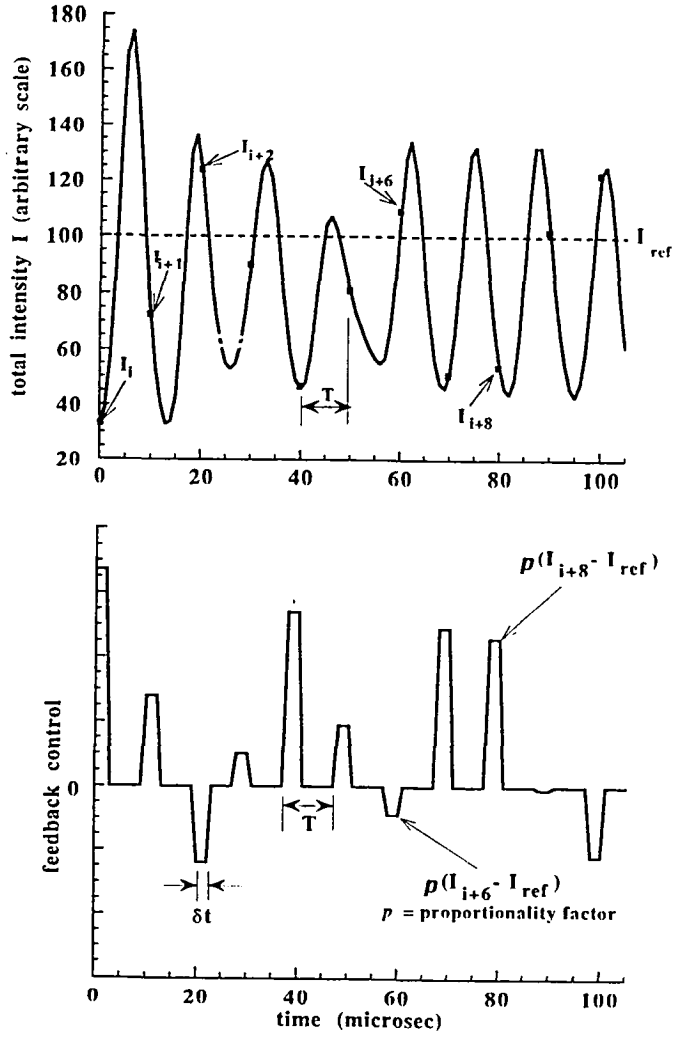

Figure 2. The occasional proportional feedback (OPF) algorithm used for control of the chaotic laser. Shown are the four parameters of the control circuit: the period T, duration of the kicks d*t*, reference level I_{ref}, and the proportionality factor *p*.

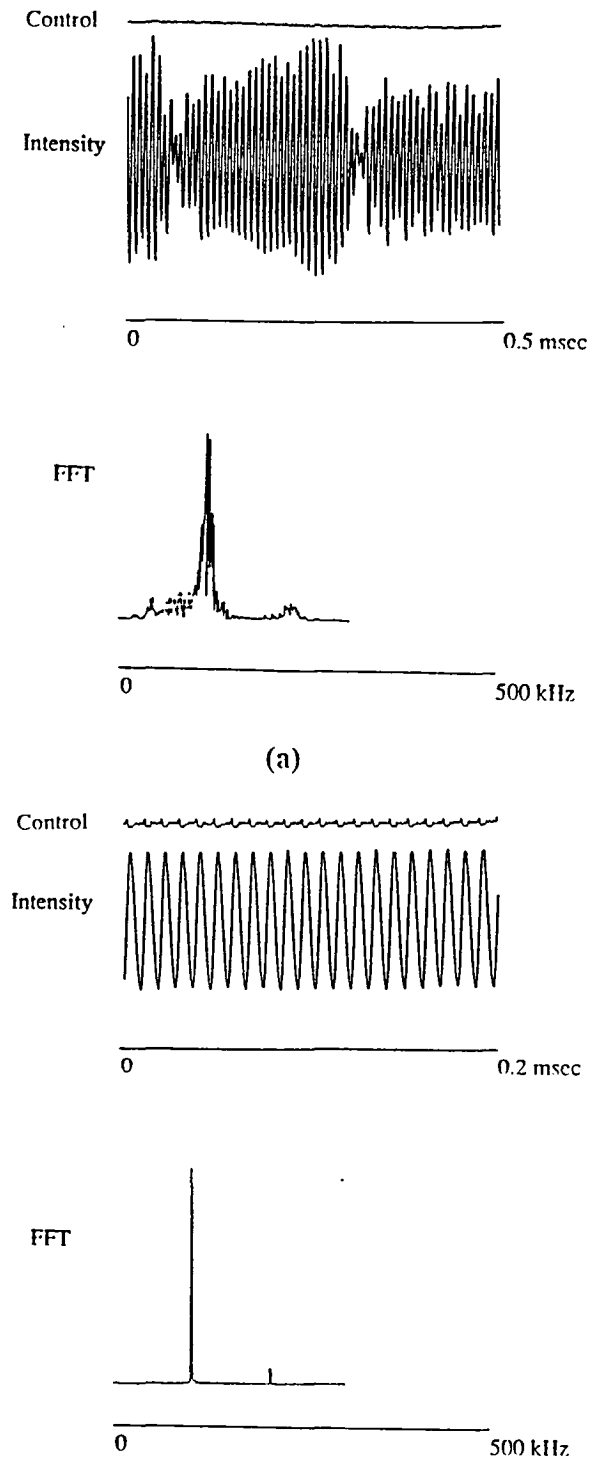

Figure 3. An example of stabilization of periodic orbits or waveforms. A typical chaotic time trace for the fundamental (1064 nm) is shown in (a), in which the underlying relaxation oscillations are present. The FFT in (a) shows a broad relaxation oscillation peak around 100 kH. The feedback control signals, waveforms and the corresponding FFT's for three periodic orbits that have been stabilized are shown in (b), (c) and (d). The relative fluctuations of the control signal about the ambient value are of the order of a few percent. (Ref. 11)

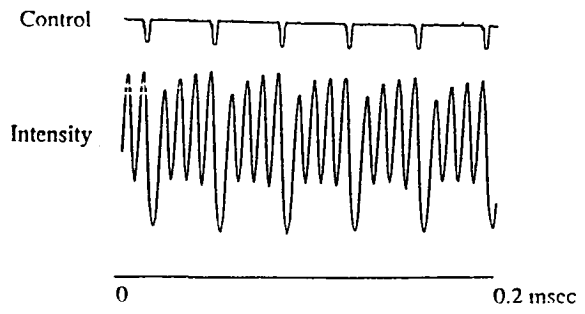

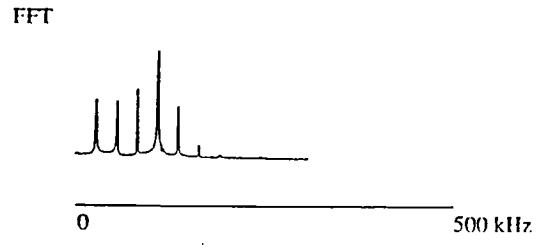

(c)

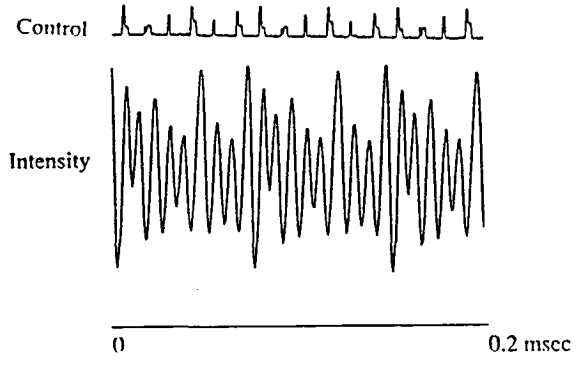

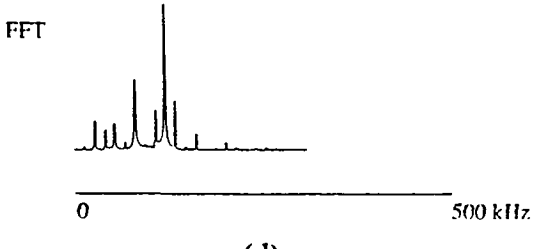

(d)

Figure 3. Concluded.

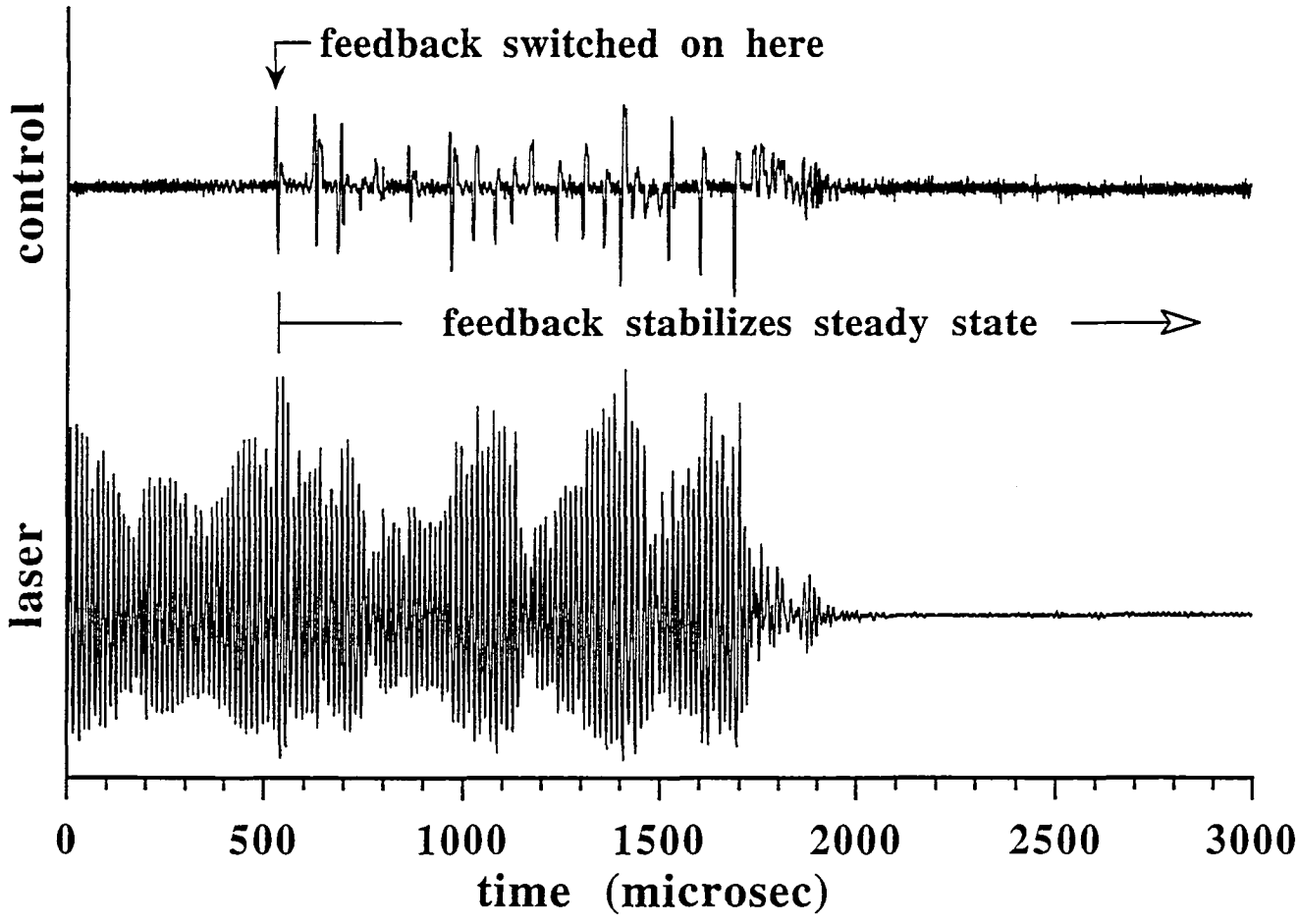

Figure 4. Stabilization of the steady state. Shown is an example of transient behavior towards the steady state when the control is switched on.

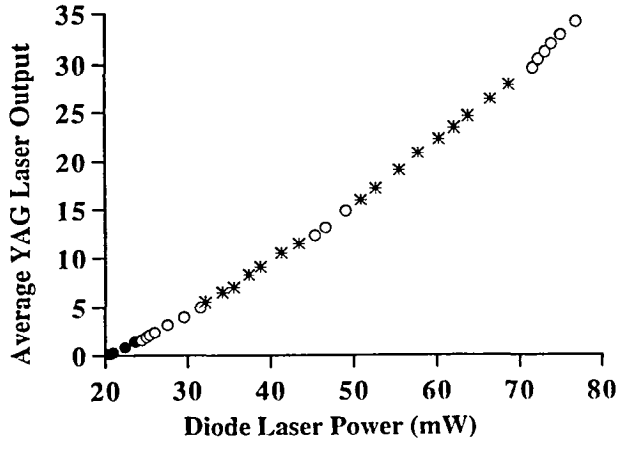

(a)

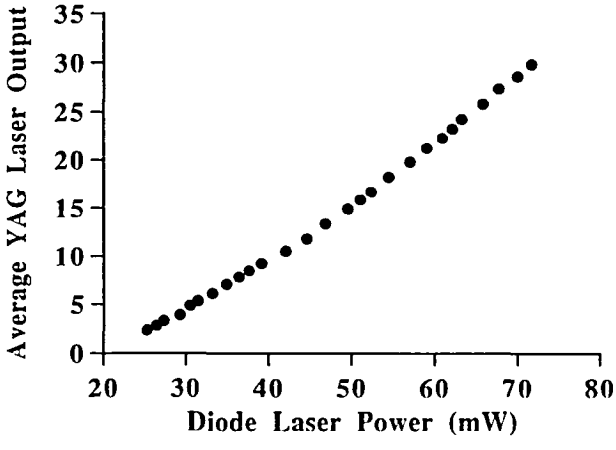

(b)

Figure 5. Control combined with a tracking algorithm allowed us to extend the stability regime of the laser. The average laser output without control is shown in (a) where the solid circles represent stable output, the open circles periodic oscillations, and the crosses chaotic fluctuations. In (b), stable output is obtained over the entire pump power range with control and tracking. The y-axis shows the Nd:YAG 1064 nm output on a relative scale. (Ref. 14)

ACTIVELY PUMPED OPTICAL FILTERS AT 532 nm

Richard I. Billmers, S.K. Gayen*,Vincent M. Contarino,
William J. Scharpf, and Martin F. Squicciarini
Naval Air Warfare Center - AD
Code 5012
Warminster, PA. 18974-0591

David A. Allocca
Ampac Inc.
26 Amy Dr.
Norristown, PA.

ABSTRACT

The operation of two narrow-band optical filters at 532.33 nm is presented. Both of these filters operate on the $4P_{1/2}$ to $8S_{1/2}$ excited-state transition in potassium vapor. One of the filters is based on excited-state Faraday effect, and requires the application of an external axial magnetic field. The peak transmission of this filter is approximately 3.5% with a linewidth of less than 10 GHz. The second filter does not require a magnetic field for its operation, but readily attains peak transmissions of 25-30%. The $4P_{1/2}$ state is excited by a 769.9 nm light pulse which is linearly polarized for the first scheme and circularly polarized for the second.

* Permanent address is Dept. of Physics and Engineering Physics
Stevens Institute of Technology, Hoboken, NJ 07030

INTRODUCTION

Narrow-linewidth, high transmission optical filters are essential components of a lidar system. Several schemes such as Faraday anomalous dispersion optical filters (FADOF) (refs. 1 & 2), atomic line filters (ALF) (ref. 3) and actively-pumped ALF's use sharp optical transitions in atomic vapors to meet the requirement of narrow linewidth. Except for actively-pumped ALF's (refs. 3 & 4), these filters commonly use transitions originating from the ground state of atomic vapors. Excited-state (ES) transitions have not yet been explored in any detail for filter application (refs. 3 & 4). Efficient operation of an optical filter, on the other hand, requires a rugged and reliable laser. The Nd-doped yttrium aluminum garnate (YAG) is the most well developed solid-state laser to date. Its second-harmonic radiation at 532 nm has good atmospheric and underwater transmission. So, a filter operating at 532 nm is of considerable practical interest. In this article, we report on experimental demonstrations of two optical filters that operate at 532.33 nm, a wavelength readily attainable by temperature tuning the YAG crystal (ref. 5).

The operation of both filters is based on the $4P_{1/2}$ to $8S_{1/2}$ excited-state transition in potassium vapor. The change induced in the state of polarization of a linearly-polarized probe beam by resonant interaction with the K-vapor is the mechanism behind operation of both filters. However, the schemes used for altering the polarization characteristics of the probe beam are different in the two cases. The first scheme is based on the anomalous Faraday effect. FADOF's operating on transitions from the ground state are well understood. The same principle is extended to transitions from the excited state. The cell containing the atomic vapor is placed between two crossed-polarizers and an external axial magnetic field is applied. The transition from the $4S_{1/2}$ ground state to the $4P_{1/2}$ initial state of the filter transition is excited by a linearly polarized 769.9 nm pump pulse for the operation of this excited-state FADOF (ESFADOF). A simplified and partial energy-level diagram of K-vapor showing only the relevant levels and transitions is shown in figure 1. In the second scheme, the $4P_{1/2}$ state is populated by a circularly polarized 769.9 nm pulse and no external magnetic field is required. The polarization state of the linearly-polarized probe beam is altered due to nonlinear interaction in the atomic vapor

resulting in transmission through the cross-polarizers. The exact physical mechanism behind the operation of this excited state polarization altering filter (ESPAF) is still under investigation. In the subsequent sections we first present the experimental arrangements used for demonstrating the operation of the filters. The transmission spectra of the filters are then presented, and the issue of noise is discussed.

EXPERIMENTAL ARRANGEMENT

The operation of both of the excited-state optical filters require: (a) exciting population from the $4S_{1/2}$ ground state to the first-excited $4P_{1/2}$ state, and (b) inducing a transition from the excited $4P_{1/2}$ to the $8S_{1/2}$ state in potassium vapor. The experimental arrangement for ESFADOF is shown schematically in figure 2. Potassium vapor was generated by heating a 7.5 cm long cell to 230 C while maintaining the sidearm temperature at 200 C. The number density in the vapor phase is controlled by the sidearm temperature, and was 1.5×10^{14} atoms/cm^3 at 200 C.

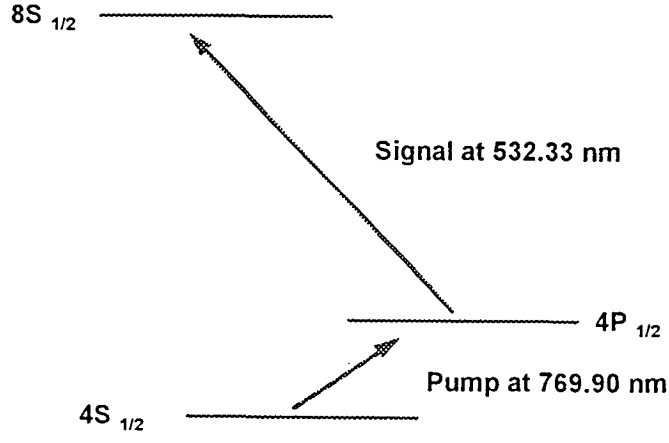

Figure 1 - Simplified energy level diagram of excited-state optical filters in K vapor.

The cell axis was aligned with that of a Helmholtz coil, which provided a 100-gauss dc magnetic field when 3A of current was passed through it. The 769.9-nm pump pulse used to excite the K-atoms to the $4P_{1/2}$ state was obtained from a dye laser (Spectra Physics PDL-1) pumped by the second harmonic of a Nd:YAG laser (Spectra-Physics DCR 2). The laser operated with a solution of the organic dye LDS 751 (Exciton Chemical) in methanol. A second dye laser operating with a solution of Coumarin 500 in methanol and pumped by the third harmonic of the same Nd:YAG laser generated the 532.33-nm probe pulse. The outputs of both the dye lasers were linearly polarized, with a nominal linewidth of ~ 4 GHz. The pulse repetition rate of 10 Hz for both the dye lasers was determined by that of the pump laser. The probe pulse was passed through a Glan-Thompson polarizer and traversed the cell collinearly with the pump pulse. Both the pulses were multimode. However, a measurement of their spatial profiles using a scanning razor blade revealed that those could be approximated as Gaussians. The beam diameters of the pump and the probe pulses were 1.1 and 0.65 mm, respectively. The intensity of the probe pulse was maintained at 5 mW/cm^2. The maximum intensity of the pump pulse was 8 MW/cm^2 and was controlled by a set of calibrated neutral-density filters. The two turning prisms in the path of the probe beam served as an optical delay line to ensure the proper timing of the pump and probe pulses. The beams then exited the cell where they were blocked by a Glan-Thompson cross polarizer. The transmission of the probe pulse through the crossed polarizers when the cell was not pumped was less than 0.001%. A photomultiplier (BURLE 31034A) was used to detect the transmitted light. A narrow band-pass filter before the detector ensured that no pump radiation interfered with the detection of green light passing through the second polarizer. The signals from the photodiode were digitized, averaged over 30 laser shots, and stored for display on an IBM AT compatible computer. The computer was also interfaced to stepper motors that scanned the dye lasers by angle-tuning the gratings used as back mirrors of the dye-laser cavities.

The experimental arrangement for ESPAF was very similar to that of ESFADOF except for the following changes. First, a quarter-wave plate was placed before the cell in the path of the 769.9 nm beam to convert its polarization from linear to circular. The Glan-Thompson polarizer before the cell was placed in the path of the probe beam only. Since the magnetic field was not necessary for filter operation, no current was passed through the Helmholtz coil.

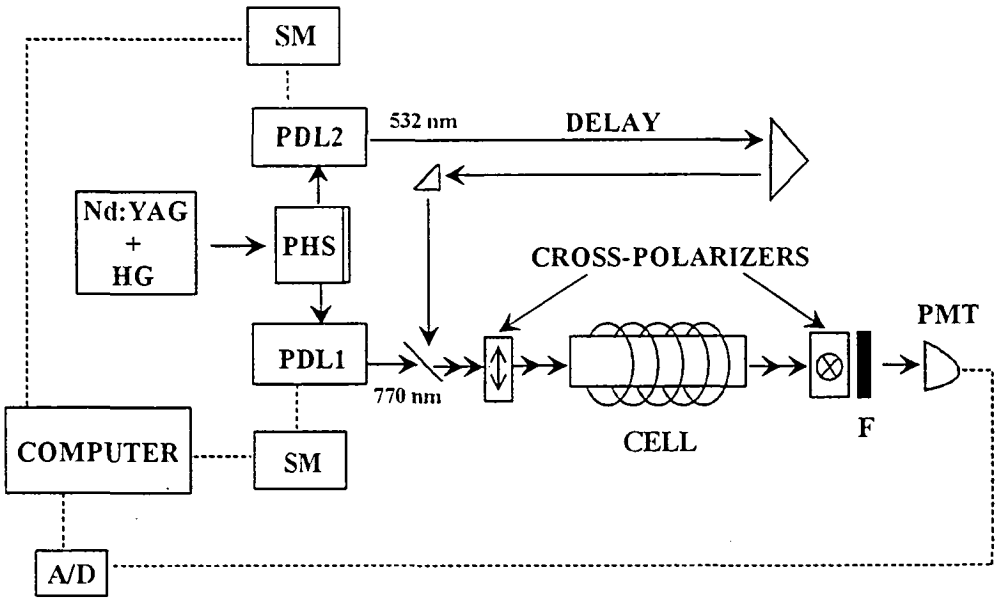

Figure 2 - Experimental setup for excited-state optical filters in potassium vapor. HG=Harmonic Generator, PHS = Prism Harmonic Separator, SM = Stepper Motor, PDL = Pulsed Dye Laser, F = Bandpass Filter, PMT = Photomultiplier tube.

RESULTS

A. ESFADOF Transmission Spectra

The experimental results for the excited-state Faraday optical filter are shown in figure 3. The top trace represents the excited-state filter spectrum. An 80 kW/cm^2 optical excitation pulse was tuned to the $4S_{1/2}$ - $4P_{1/2}$ absorption linecenter at 769.33 nm and the magnetic field was applied. A very low intensity probe pulse collinear with the excitation pulse was scanned through the $4P_{1/2}$ - $8S_{1/2}$ transition wavelength. The resultant 3.5% peak transmission was a ratio of the maximum photodetector signal to the signal at the detector with the pump beam blocked and the polarizers uncrossed. The bottom trace shows that the excited-state filter transmission disappears when the optical excitation is turned off.

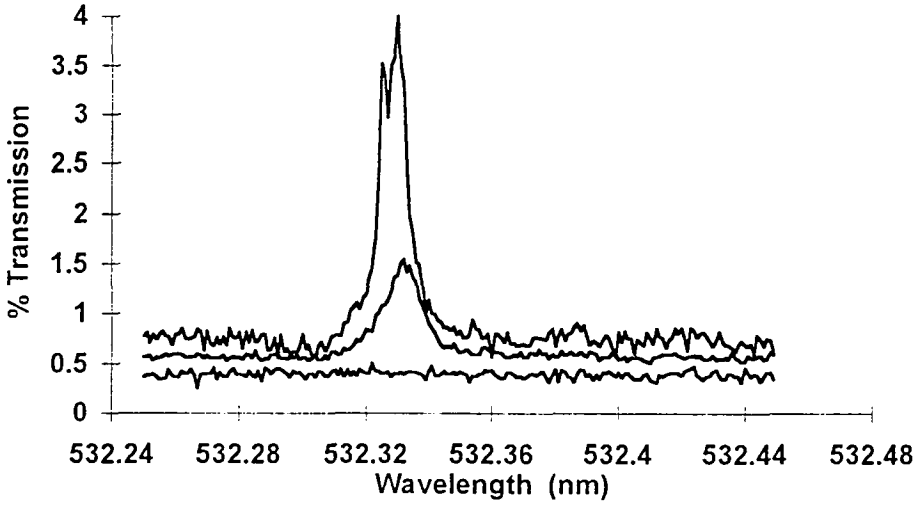

Figure 3 - Excited-State Faraday filter transmission spectrum. The top trace represents the pump beam, probe beam and external magnetic field all on. The middle trace represents only the pump and probe beams on but no external magnetic field applied. The bottom trace represents the probe on and a magnetic field applied but no pump beam.

The transmission also disappears when the optical excitation is tuned away from the $4S_{1/2}$ - $4P_{1/2}$ absorption linecenter at 769.33 nm. The middle trace shows that the transmission at 532.33 nm does not disappear when the axial magnetic field is removed from the Faraday filter. This is an indication of the ESPAF effect. We have witnessed similar behavior for the ground-state Faraday filter at intensities above 10 KW/cm^2. This effect is still under investigation. The measured peak transmission of 3.5% is not optimal. The 4 GHz linewidth of the green probe laser is much wider than the Doppler linewidth of the transition. A preliminary theoretical model along the line of reference 6 predicts that the transmission could be optimized by increasing the magnetic field and the number density, and that 70-80% transmission is possible.

B. ESPAF Transmission Characteristics

Typical ESPAF transmission spectra for two different intensities are shown in figure 4. The salient features of the spectra are: (a) approximately an order-of-magnitude higher transmission, and (b) a factor-of-2 broader linewidth compared to that of the ESFADOF. The shape of the transmission spectrum depends strongly on the intensity of the pump beam. At higher intensities, a broad shoulder appears at shorter wavelengths which changes position and shape with intensity. At intensities below 1 MW/cm^2 the shoulder collapses into the larger main peak. The position and shape of the main peak seem to be much less sensitive to pump intensity. The FWHM of these peaks is approximately 5 GHz which is a factor of 2 to 3 larger than the Doppler width of the peaks in the Faraday transmission spectrum. The main peak at 532.33 nm shows the same double-hump shape as that of the Faraday transmission peak in figure 3. This may suggest that there is some structure in this peak that cannot be resolved with the current probe laser configuration. The peak transmission is dependent on both pump intensity and sidearm temperature. The transmission increases nonlinearly with the pump intensity until saturation is reached at approximately 800 KW/cm^2 where the transmission levels off at

25-30%. The transmission also increases with sidearm temperature from 180 to 205 C. Initial results suggest that the transmission may decrease at sidearm temperatures above 205 C; however, further investigations are necessary to confirm this result.

C. Noise Considerations

Preliminary measurements were done to determine whether noise photons at 532.33 nm are being generated due to the optical excitation in either filter configuration. An 8 MW/cm^2 optical excitation pulse was tuned to the $4S_{1/2}$ - $4P_{1/2}$ resonance at 769.33 nm and a photomultiplier tube (BURLE 31034A) was set up orthogonal to the optical axis to detect fluorescence photons at 532.33 nm.

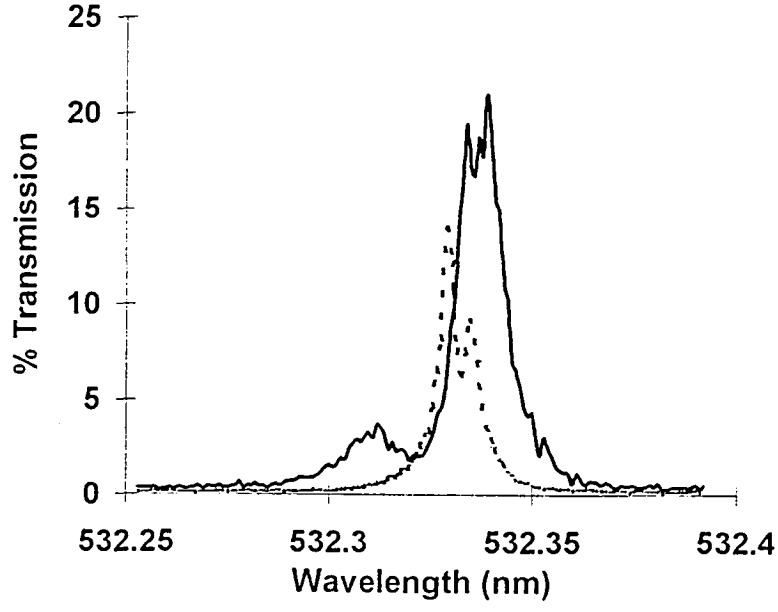

Figure 4 - Excited-State Polarization Altering Filter transmission spectrum at two different pump intensities. The solid line represents the spectrum taken at a pump intensity of 4 MW/cm^2 and the dashed line at 250 KW/cm^2.

The results showed no such measurable noise down to ~100 photons/pulse which was the limit set by scattered light from the doubled YAG pump laser. Since operation of both filters is based on monitoring the transmitted probe beam at 532.33 nm, photons that may be generated at other wavelengths due to relaxation of the excited states may be effectively discriminated against, and may not contribute to the noise problem as was the case for the atomic line filter based on these transitions (ref. 4).

SUMMARY AND CONCLUSION

In summary, we have demonstrated two optical filters based on excited-state transitions in potassium vapor at the second-harmonic wavelength of the Nd:YAG laser. A major implication of this result is that the excited-state transitions may be employed to develop frequency-agile filters to match specific wavelengths of interest. The demonstration of ESPAF presents a new physical mechanism for optical filter design that, to the best of our knowledge, has not been used before. Detailed understanding of the physics behind the operation of this filter and the development of models to predict filter characteristics are interesting and challenging problems for further investigation.

REFERENCES

1. Dick, D. J.; and. Shay, T.M: Ultrahigh-Noise Rejection Optical Filter, *Opt. Lett.*, vol. 16, 1991, pp. 867-869.

2. Menders, J.M.; Benson, S.H.; Liu, C.S.; Korevaar, E.: Ultranarrow Line Filtering Using a Cs Faraday Filter at 852 nm, *Opt. Lett.*, vol. 16, 1991, pp. 846-848.

3. For a review of ALF's, also known as atomic resonance filters, see Gelbwachs, J.A.: Atomic Resonance Filters, *IEEE J. Quantum. Electron.*, vol. 24, 1988, pp. 1266-1277. Excited-state ALF's also referred to as active ALF's.

4. Marling, J.B.; Nilsen, J; West, L.C.; Wood, L.L: An Ultrahigh-Q Isotropically Sensitive Optical Filter Employing Atomic Resonance Transitions, *J. Appl. Phys.*, vol. 50, 1979, pp. 610-614.

5. Marling, J. B.: 1.05-1.44 μm Tunability and Performance of the CW Nd^{3+}:YAG Laser, *IEEE J. Quantum. Electron.*, vol. 14, 1978, pp. 56-62.

6. Yeh, P.: Dispersive Magnetooptic Filters, *Appl. Opt.*, vol. 21, 1982 , pp. 2069-2075.

Subpicosecond Third Order Nonlinear Response in Polythiophene and Thiopene Based Thin Films

D. Harris, E. Royer, and R. Dorsinville

Department of Electrical Engineering

The Center for Analysis of Structures and Interfaces,

and Center for Advanced Technology

The City College of the City University of New York

ABSTRACT

Ultrafast relaxation kinetics of the third order nonlinear susceptibility of polythiophene and polycondensed thiophene-based polymer was determined by the forward degenerate four-wave mixing technique. Deep into the absorption band the nonlinear response shows only a fast component (< 900 fs at 587nm) while at the edge of the absorption band at 642nm a much slower and complex decay was measured.

INTRODUCTION

Investigation of the nonlinear optical (NLO) properties of organic systems possessing delocalized π electrons still attracts considerable interest because of the large and fast NLO response of such systems. The dynamics of the excited states of polythiophene (pT) and its derivative has been extensively studied by Z. Vardeny et al. [1], Prasad et al. [2], and Kobayashi et al. [3] using picosecond and femtosecond pump and probe techniques. Four wave mixing techniques were used to determine the magnitude of the nonlinear optical coefficient by Dorsinville et al. [4] However their time resolution (< 15 ps) did not allow for a comparison with the pump and probe subpicosecond measurements. Surprisingly, Prasad et al. [5] reported no measurable slow components in their subpicosecond four wave mixing measurements in several thiophene based polymers in contradiction with the pump and probe results.

In this paper we present studies of the subpicosecond relaxation dynamics of the third-order nonlinear optical effects at 587 nm and 642 nm for pT and polydithieno(2-b;2',3'-d)thiophene (pDTT). The samples were thin films (~ 2 μm thickness) prepared by electrochemical polarization. [6] In order to determine the dynamics, different polarization configurations (xyxy and xxxx) were used. The reported measurements are focused on the dynamics of the DFWM response in pT and pDTT, in contrast with our earlier work, which emphasized the magnitude of the nonlinear response [4].

EXPERIMENTAL TECHNIQUES

The technique used in this experimental study of the dynamics is degenerate four-wave-mixing (DFWM) in the folded boxcar geometry. [7] The experimental setup is shown in fig. 1. A cw mode-locked Nd:YAG oscillator

provides 1.06 um pulses at 76 MHz with a pulse duration of about 100 ps and average power of about 26 watts. About 4 watts at 532 nm are generated after frequency doubling in a KTP crystal and then divided into two 2 watt laser beams. The second harmonic beams are used to synchronously pump a linear cavity dye laser and an intracavity-dispersion compensation dye laser. The pulse duration of the dye lasers' output varied between 900 fs and 150 fs. With Rhodamine 6G, the output wavelength was set at 587 nm and maximum average power was about 250 mW. With Kiton red the wavelength was set at 642 nm and the maximum average power was 150 mW. The output of the dye lasers was synchronously amplified to several microjoules per pulse at 1 kHz repetition rate through a two and three stage amplifier dye chain, respectively. The amplification pump source is the second harmonic of a regenerative amplifier seeded by about 1% of the fundamental output of the cw Nd:YAG. The output beam of the dye amplifier is divided into almost three equal power using two beam splitter. The polarization of all three interacting laser beams and the DFWM signal beam was adjusted with half-wave plates and polarizers. Delay lines were used to obtain the temporal information. The beam geometry is shown in fig. 2. The signal wavelength was selected by a spectrometer and detected with a cooled PMT.

RESULTS AND DISCUSSION

A typical time resolved DFWM profile at 587 nm and 642 nm from pT is shown in fig. 3. For these measurements, all beams were polarized parallel to each other (xxxx). Similar curves were obtained for pDTT at 587 nm and 642 nm. At 587 nm the profile is essentially resolution limited and reveals a fast nonlinear response (< 900 fs). At 642 nm there is a strong slow component. No significant change in the value of the FWM signal was observed when the samples were rotated, indicating that the films were isotropic. In the xxxx polarization

combination, three gratings are formed: one grating is from the two pump beams (1 and 2) and the other two gratings are created by each one of the pump beams and the probe beam. All three gratings contribute to the signal at zero delay. However, only the grating generated by the two pumps contributes to the signal away from zero delay. The contribution from that single grating can be isolated by having the probe and signal beams polarized perpendicular to the two pumps. [8] This polarization arrangement (yxyx) should lower the contribution of the fast electronic response to the FWM signal and allow for the study of the slow component of the DFWM signal intensity from both pT and pDTT. Fig. 4 (a and b) shows the FWM signal as function of delay between the pumps and the probe for pT and pDTT for the yxyx configuration at 642 nm. The curves have clearly a slow decay component. At 587 nm the yxyx curves were identical to the xxxx curves and no slow component could be detected. The difference in the kinetics at the two wavelengths is probably due to the fact that 587 nm is well above the bottom of the first excited state and 642 nm is close to the band edge energy (1.9 eV). As a result the response time at 587 nm is controlled by the thermalization time within the excited state while the kinetics at 642 nm is controlled by the different carrier lifetimes. According to the model proposed by Kobayashi et al.[3] for polythiophene, after excitation above the absorption edge, free excitons are first created which decay within femtoseconds into self-trapped (ST) excitons with a lifetime of about 800 fs. The ST excitons in turn decay into long-lived species, probably polarons and/or bipolarons, with possible contributions from triplet excitons generated through two photon absorption. [3] The FWM results at 642 nm seem to fit this model quite well as shown in figure 4 (a and b) where the experimental curve has a subpicosecond response followed by a long lasting tail. However, attempts to fit the FWM decay to a power law $t^{-\alpha}$, as expected from the polarons/bipolarons conversion model, were only partially successful as seen in

figure 4 where the best power law fit (α = 0.7) is shown. A good fit to the data is only achieved between 1 and about 30 picoseconds and fails for longer times. An acceptable fit can be obtained by assuming a double exponential decay with a relatively fast time constant τ = 7 ps and a slower time constant τ = 50 ps. These results seem to suggest the existence of a complex combination of long lived species. A precise identification of these species needs additional measurements at different wavelengths which are currently in progress. In conclusion, the third-order optical nonlinearities in pT and pDTT were studied by time-resolved degenerate four-wave mixing measurements at 587 nm and 642 nm. Both xxxx and yxyx polarizations configurations were investigated. The DFWM measurements in both materials confirm results from previous pump and probe absorption measurements and show that near the band edge the DFWM signal response follows closely the charge carrier dynamics.

ACKNOWLEDGEMENTS

We would like to thank Dr. C. Taliani (CNR, Bologna, Italy) and its group for providing some of the samples used in these studies. This work is supported by NSF under grants # HRD-8802964 and ECS-9212310 and New York State Technology Foundation.

REFERENCES

1 Z. Vardeny, H. T. Grahn, A. J. Heeger and F. Wudl, Synth. Met., 28, C299 (1989)

2 M-T. Zhao, Bhanu P. Singh, Paras N. Prasad, J. Chem. Phys, 89, 5535 (1988)

3 T. Kobayashi, M. Yoshizawa, U. Stamm, M. Taiji, M. Hasegawa, JOSA B, 7, 1558 (1990)

4 R. Dorsinville, Lina Yang, R. R. Alfano, R. Zamboni, R. Danieli, G. Ruani, and C. Taliani, Optics Letters. 14, 1321 (1989).

5 B. P. Singh, M. Samoc, S. Nalwa, and P.N. Prasad, J. Chem. Phys. 92, 2756 (1990).

6 P. Di Marco, Mastragostino, C. Taliani, Mol. Cryst. Liq. Cryst., 118, 241 (1985)

7 L.Yang, Q.Z. Wang, P.P. Ho, R.Dorsinville and R.R.Alfano, Appl. Phys. Lett. 53 (1988) 1245

8 W. Kaiser, Ultrashort laser pulses and applications (Springer,Berlin,1988)

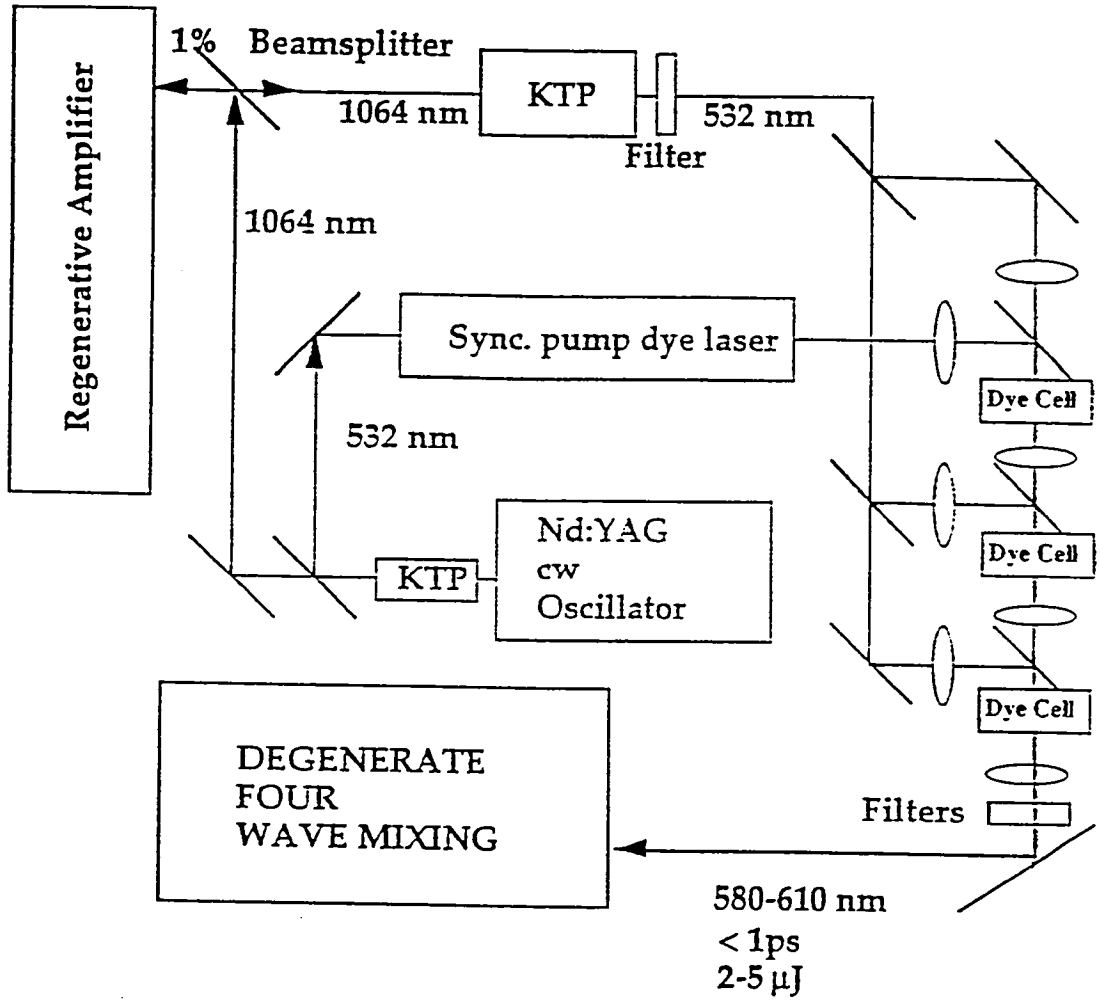

Figure 1. Schematic diagram of the experimental setup .

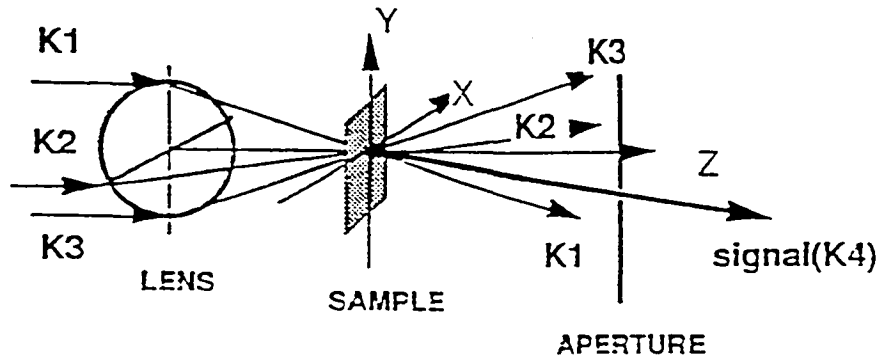

Figure 2. Schematic shows the beam geometry of the four wave mixing experiment. K_1, K_2, and K_3 are the two pump and probe beams, K_4 is the signal beam. The signal wavelength was detected with a cooled PMT.

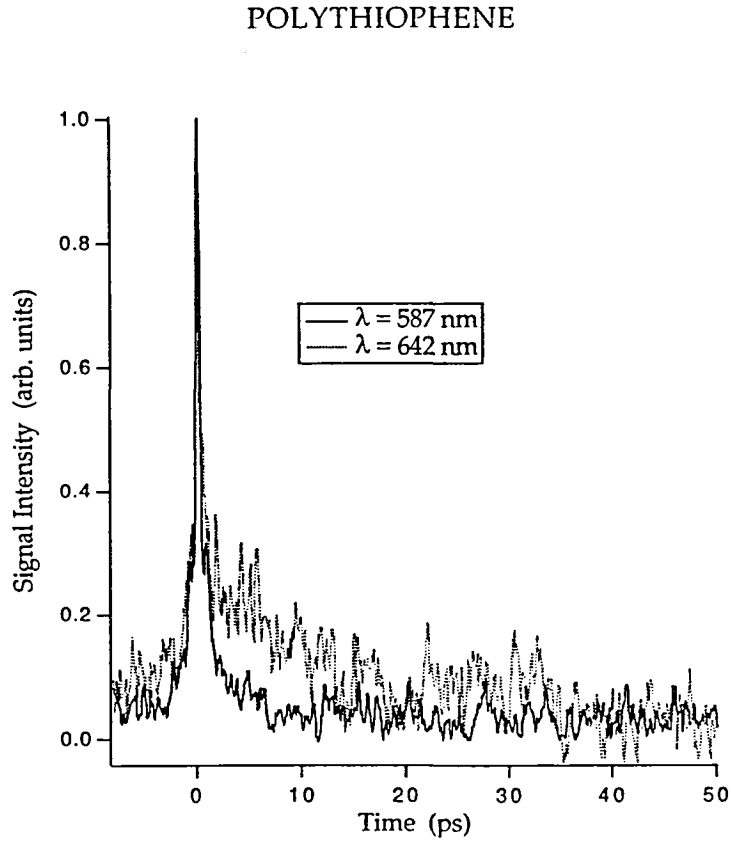

Figure 3. Typical time resolved degenerate four wave mixing signal versus time delay at 587 nm and 642 nm from pT. The beams polarization configuration is **XXXX.**

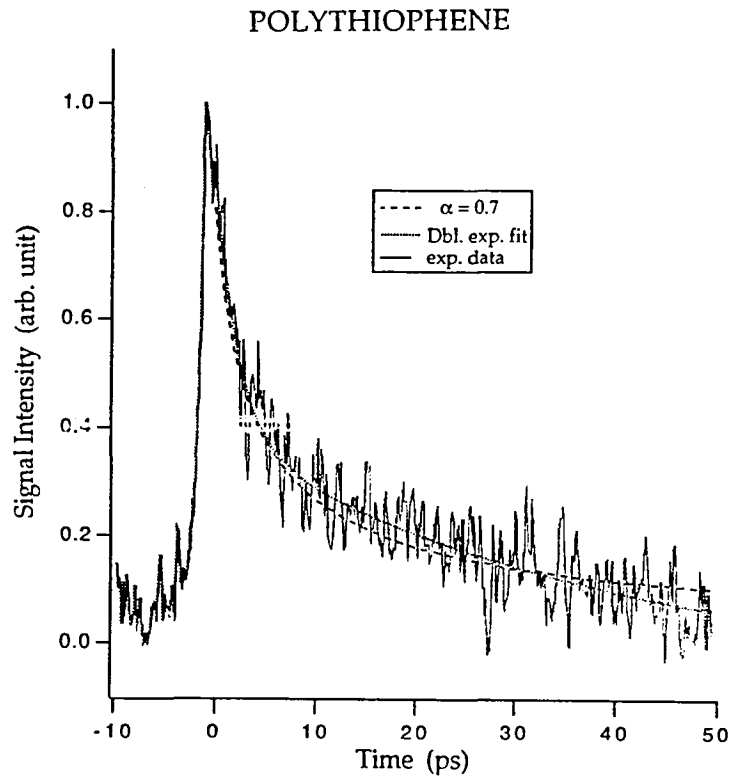

Figure 4a. FWM signal as a function of delay between the pumps and the probe for pT for the YXYX configuration at 642 nm. The dashed line shows a fit to the data achieved by calculating the double exponential decays and power law.

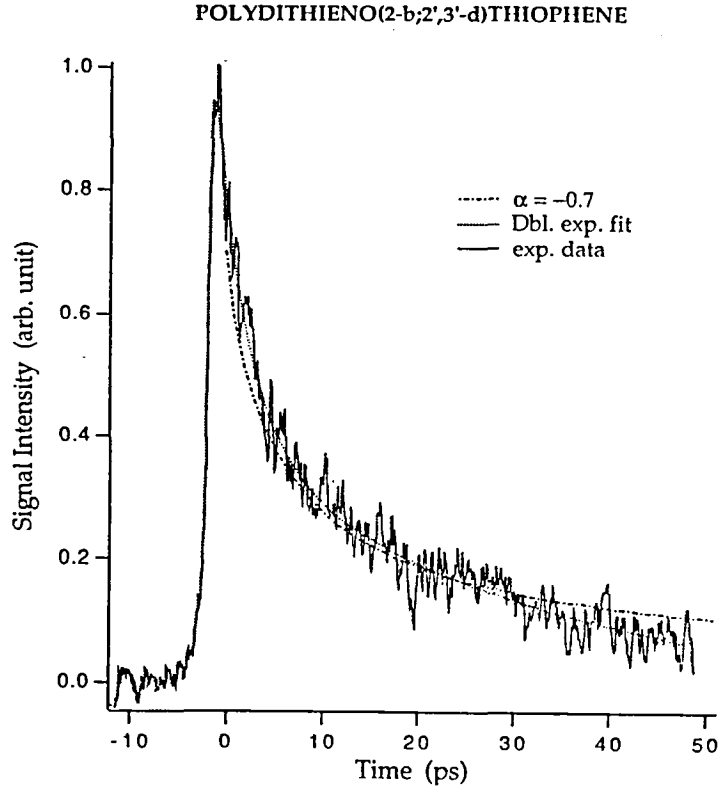

Figure 4b. FWM signal as a function of delay between the pumps and the probe for pDTT for the YXYX configuration at 642 nm. The dashed line shows a fit to the data achieved by calculating the double exponential decays and power law.

CRYSTAL GROWTH AND SPECTROSCOPY OF DIGLYCINE

Taravia M. Taylor
Fisk University
Physics Department
Nashville, TN

INTRODUCTION

Raman and infrared spectra have been obtained for α-diglycine ($C_4H_8N_2O_3$) single crystals. These dipeptide crystals are being grown as a model system for protein crystal growth studies. There have been previous Raman measurements on diglycine powder samples recorded (refs. 1, 2), but there is no reference to measurements on oriented diglycine single crystals. Diglycine can grow in one of three forms α, β, or γ . The ß and γ transform to α at approximately 100° C in one day (ref. 3). The crystals are monoclinic with four molecules per unit cell and a calculated density of 1.516 g/cm^3. α-diglycine has been assigned to a $P2_1/a$ or C^5_{2h} space group (refs. 4, 5). The diglycine crystal has 201 vibrational modes ($51A_g + 50A_u + 51B_g + 49B_u$) of which 21 ($6A_g + 6B_g + 5A_u + 4B_u$) are lattice modes. Vibrations belonging to the A_g and B_g symmetry species are Raman active, while vibrations having A_u and B_u symmetry are observable only in the infrared.

Table 1. Crystal Character Table

C_{2h}	E	C_2	i	σ_h	IR	Raman
A_g	1	1	1	1	R_z	x^2,y^2,z^2 xy
B_g	1	-1	1	-1	R_x, R_y	xz,yz
A_u	1	1	-1	-1	z	
B_u	1	-1	-1	1	x,y	

EXPERIMENT

The crystals were grown through evaporation from an aqueous solution at room temperature. Transparent crystals about 1cm x 1cm x 2 mm with minor defects were obtained. These crystals were bounded by six faces of the forms {1 0 0} and {0 1 1}. The diglycine crystals, when exposed to the atmosphere, changed from transparent to a white chalky texture. The growth process took approximately two weeks. To begin the process there was an approximate one to six ratio of diglycine to water mixed together in a flask. The starting material was a minimum 99% grade of a free base diglycine powder packaged by the Sigma Chemical Co. Once the diglycine powder dissolved additional powder was added until the solution saturated. After the solution was saturated it was poured into a beaker and the water was allowed to evaporate. After the first set of crystals were grown a seed crystal from this batch was placed in the other growth setups. When good quality crystals were grown they had to be stored in a cold or moist atmosphere, because at room temperature in low humidity the crystals turned white. Once we were able to get a good transparent crystal the b-crystallographic axis was identified from the crystal habit. From symmetry, the b-axis corresponds to one of the principal axes of the refractive index ellipsoid. In monoclinic crystals the other two axes are not fixed by symmetry but may lie anywhere in the ac-plane. A section perpendicular to the b-axis was cut on a low speed diamond saw and placed under a polarizing microscope. The other two principal axes were determined by locating the extinction directions. After the extinctions were detected the crystal was cut again parallel and perpendicular to the extinction directions, and then polished using conventional techniques. A coordinate system with Z parallel to the b-axis was chosen and Raman spectra were taken rotating the polarizer and crystal.

The Raman spectra were obtained using a 90° scattering geometry on a Spex Model 1403 Raman spectrometer with a photon counting detection system. Excitation was provided by a Coherent Innova 90 argon ion laser operating at 514.5 nm and 500 mW. For reference, spectra of the as-purchased diglycine powder, crushed transparent crystal, and crushed white crystal were obtained. Differential Scanning Calorimetry (DSC) measurements were also made on the transparent crystal. A peak was detected at 100°C and the crystal was no longer transparent after the measurements were taken. Infrared reflection spectra were obtained from 400 - 4000 cm^{-1} at 1 cm^{-1} resolution using a Bomem model MB-100 infrared spectrometer. Raman spectra were measured from 10 cm^{-1} to 4000 cm^{-1} at 5 cm^{-1} resolution.

RESULTS AND DISCUSSION

The habit of the crystals obtained during the growth experiments was consistent with descriptions in the literature of α-diglycine crystals (refs. 3, 4, 5). The DSC measurements on these crystals indicated a transition near 100 °C, after which the crystal turned white.

Low frequency Raman measurements of the diglycine crystalline powder samples are shown in Figure 1. As can be seen from the figure, the spectra of the crushed white crystal and the as-purchased powder are identical, and differ from the spectra of the crushed transparent crystal. Raman spectra for

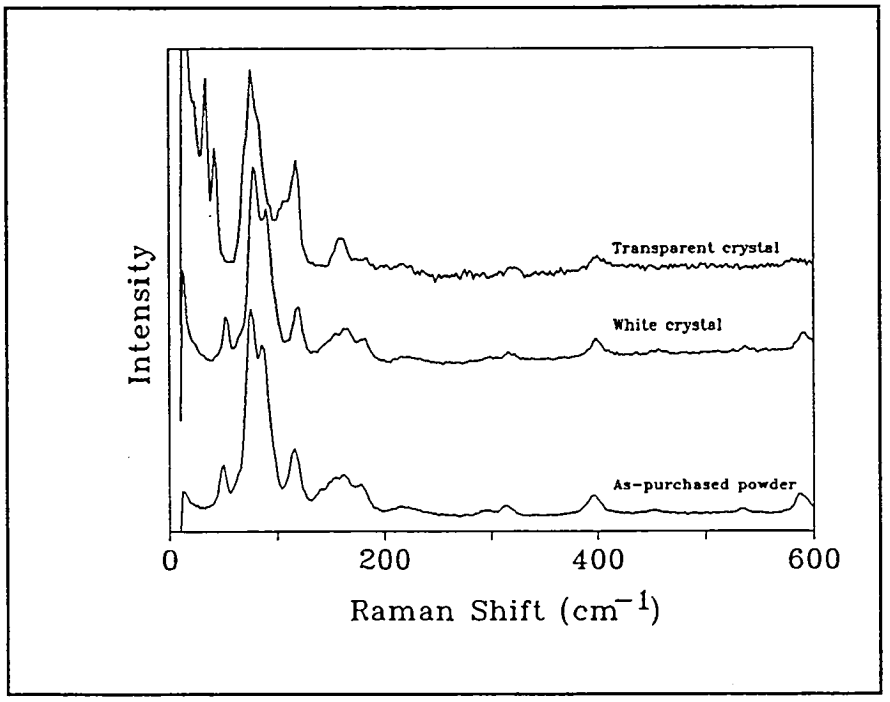

Figure 1. Low frequency Raman spectra of diglycine powders.

the same samples in the region near 3000 cm^{-1} , as seen in Figure 2, show no evidence for O-H vibrations, indicating that this transition is not due to hydration or dehydration. This result was confirmed by infrared reflectance measurements. Powder Raman spectra of α-diglycine reported in the literature (refs. 1, 2) correspond to our spectra of the crushed white crystal and the as-purchased powder. They do not agree with our spectra of the crushed transparent crystal, differing primarily in the low-frequency lattice-mode region. Lagant, et.al. (ref. 2) use their Raman frequencies, along with crystal structure information

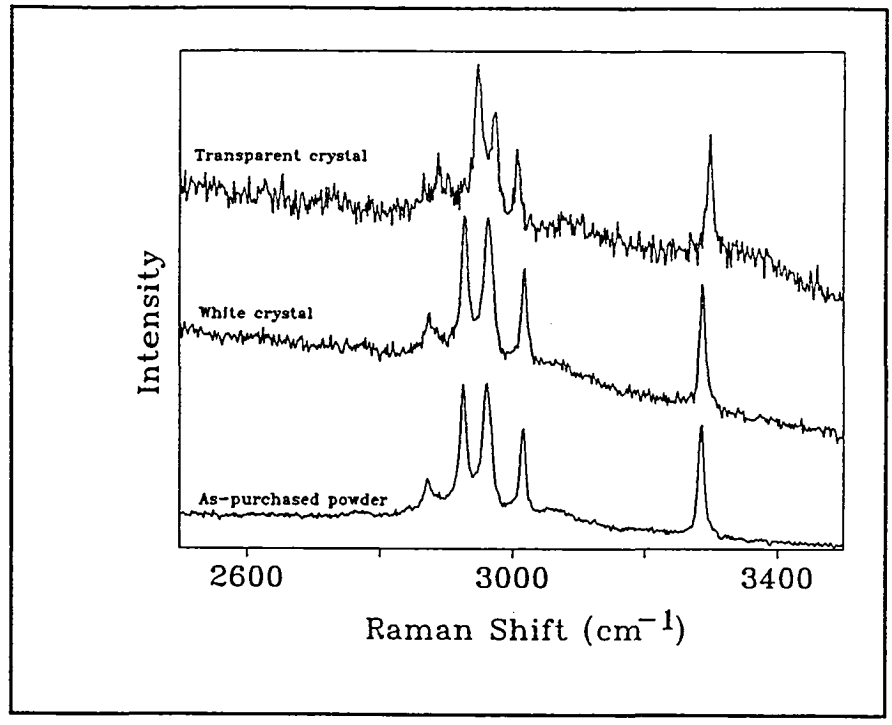

Figure 2. High frequency Raman spectra of diglycine powders.

from x-ray diffraction experiments (ref. 5), in a normal-coordinate analysis in order to determine the intermolecular potential for diglycine. Our results suggest that the crystal structure of their Raman sample may be different from that obtained in the x-ray diffraction studies.

Figures 3, 4, and 5 show the Raman active A_g and B_g modes of the oriented diglycine crystal. We were not able to observe all of the 51 A_g and 51 B_g modes predicted by group theory. The most probable reason for this is that some of the modes are inherently weak and may not be visible, or may be buried under more intense peaks. Group frequency assignments have been reported by a number of authors (refs. 1, 2, 6, 7) and are not included here. A_u and B_u modes can be observed by measuring the infrared reflectance of an oriented single crystal, followed by a Kramers-Kronig analysis. After orienting and cutting, however, our crystal was too small to obtain good signal-to-noise in this type of measurement.

CONCLUSIONS

Good quality, transparent, single crystals of diglycine were grown from aqueous solution by slow evaporation. Based upon the description of the crystal habit in the literature, these crystals were

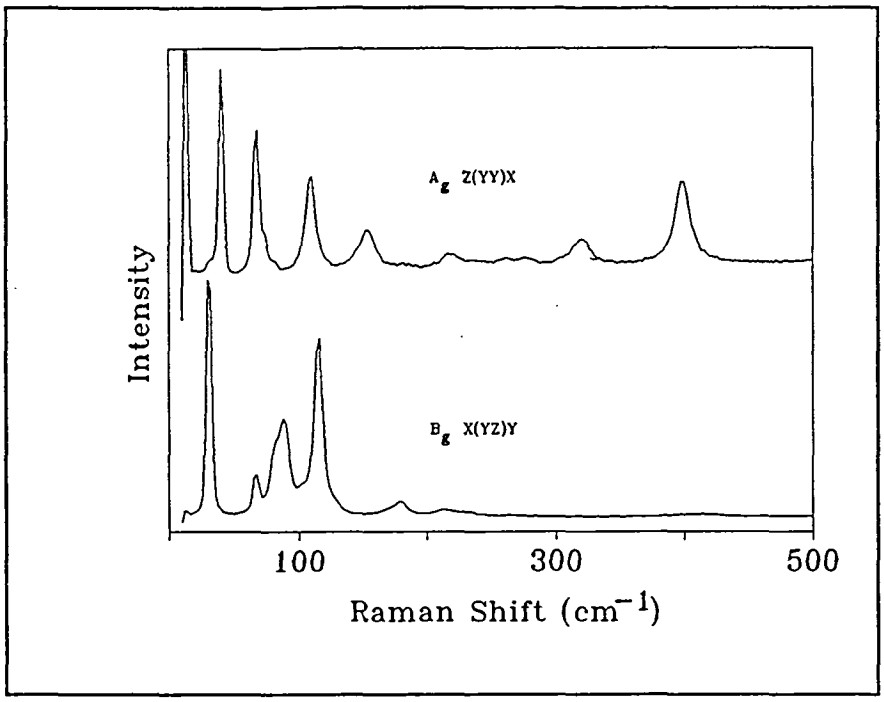

Figure 3. Raman spectra from 0-500 cm^{-1} of A_g (top trace) and B_g (bottom trace) modes of diglycine single crystal

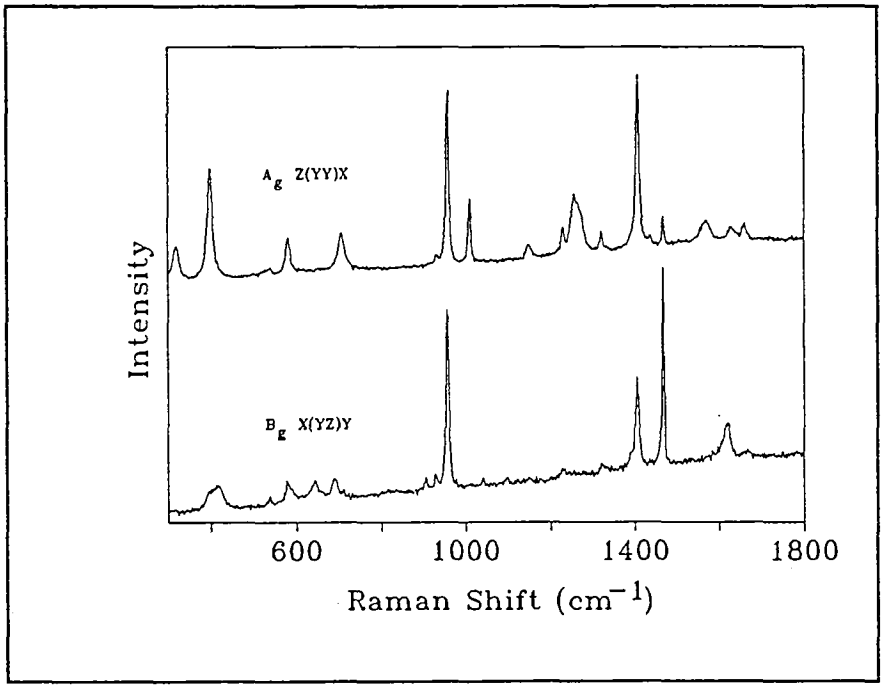

Figure 4. Raman spectra from 300-1800 cm^{-1} of A_g (top trace) and B_g (bottom trace) modes of diglycine single crystal

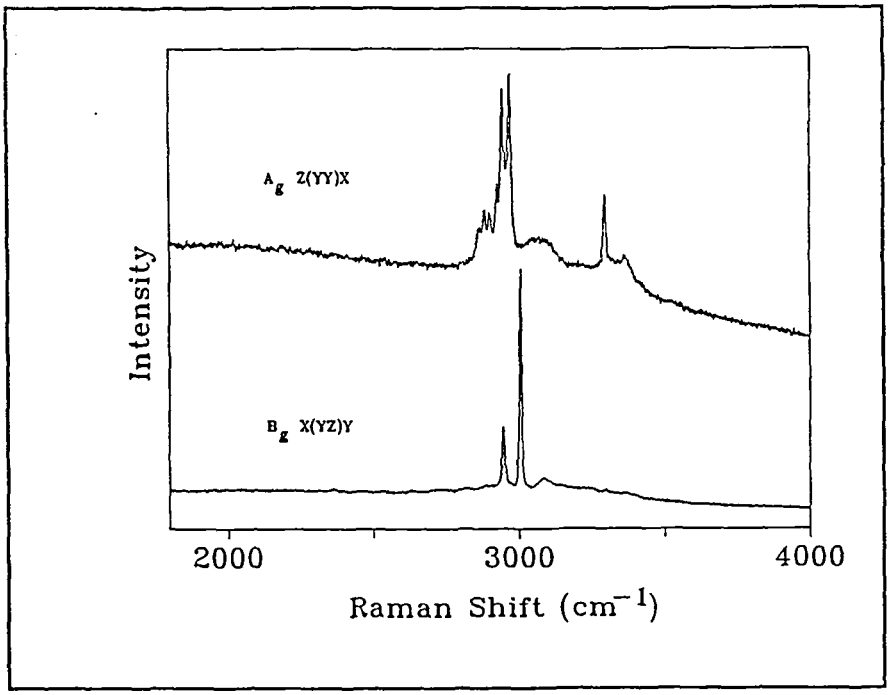

Figure 5. Raman spectra from 1800-4000 cm^{-1} of A_g (top trace) and B_g (bottom trace) modes of diglycine single crystal

determined to be the α form of diglycine. Under ambient temperature and humidity, the crystals became white and opaque in approximately 24 hours. DSC measurements show a transition at approximately 100 °C, after which the crystals turned white. Raman spectra of powder obtained from crushed transparent crystals were not consistent with Raman spectra of α-diglycine powder previously reported. Raman spectra of powder obtained from crushed white crystals were identical to the spectra of as-purchased material, and did agree with the previously published spectra. This suggests that previous analyses of the intramolecular potentials of diglycine may have been based upon the incorrect crystal structure. Further experiments will be necessary to determine the exact nature of this transition, and the structure of the white polycrystalline phase.

The A_g and B_g modes of α-diglycine were obtained through single crystal Raman measurements and are reported here for the first time. Determination of the A_u and B_u modes from infrared reflection measurements will begin as soon as crystals of a sufficient size have been grown.

ACKNOWLEDGEMENT:

The authors would like to acknowledge the support of NIH- MBRS Grant number SO6-GM08062.

REFERENCES

1. Destrade, Christian; Dupart, Elaine; Joussot-Dubien, Monique; and Garrigou-Lagrange, Chantal: Champ de Force de Valence et Modes Normaux de Vibration de la Glycylglycine et du Monochlorhydrate Monohydrate de Glycylglycine, *Can. J. Chem.*, vol. 52, 1974, pp. 2590-2602.

2. Lagant, P.; Vergoten, G.; Loucheux-Lefebvre, M.H.; and Fleury, G.: Raman Spectra and Normal Vibrations of Dipeptides. I. Glycylglycine, *Biopolymers*, vol. 22, 1983, pp. 1267-1283.

3. Hughes, Edward W.; and Moore, Walter J.: The Crystal Structure of β-Glycylglycine. Journal of the American Chemical Society, vol. 71, 1949, pp. 2618-2623.

4. Bernal, J.D.: The Crystal Structure of the Natural Amino Acids and Related Compounds, *Z. Kristallogr.*, vol. 78, 1931, pp. 363-369.

5. Biswas, A. B.; Hughes, Edward W.; Sharma, Brahama D.; and Wilson, J. Norton: The Crystal Structure of α-Glycylglycine, *Acta. Cryst.*, vol. B24, June 12, 1967, pp. 40-50.

6. Dwivedi, A. M.; and Gupta, V. D.: Normal Vibrations of α-Glycylglycine. *Biopolymers*, vol. 11, 1972, pp. 2091-2098.

7. Smith, M.; Walton, A.G.; and Koenig, J.L.: Raman Spectra of Polyglycines, *Biopolymers*, vol. 8, 1969, pp. 29-43.

LASER-INDUCED PHOTOCHROMIC CENTERS IN Ce^{3+}:$La_2Be_2O_5$

Y. M. Cheung and S. K. Gayen
Department of Physics and Engineering Physics, Stevens Institute of Technology
Hoboken, NJ 07030

and

D. M. Gualtieri
Applied Physics Laboratory, Allied Signal Research and Technology
P.O.Box 1021, Morristown, NJ 07962-1021

ABSTRACT

Intense 355-nm excitation of the lowest *4f*-->*5d* transition of Ce^{3+}:$La_2Be_2O_5$ leads to a brownish coloration of the crystal due to the formation of stable photochromic centers. These centers are characterized by a broadband absorption spectrum that spans the 220-840 nm spectral range. Since they can be readily bleached by optical excitation into their absorption bands, the centers are photochromic. They are produced by a two-step photoionization of Ce^{3+} ions followed by attachment of the detached electrons at trapping sites in the crystal. The dependence of the number of centers on laser intensity and length of exposure have been measured, and the kinetics of growth have been studied.

INTRODUCTION

Single crystals doped with trivalent cerium (Ce^{3+}) are prospective materials for the development of tunable solid-state lasers in the blue-green and near-ultraviolet spectral regions (refs. 1-3). However, intense ultraviolet excitation into Ce^{3+} absorption bands is known to produce both transient and stable color centers in some of these crystals (refs. 4-6). The broadband absorption spectra of these color centers often overlap with the Ce^{3+} fluorescence spectra, and have deleterious effects on the gain and lasing characteristics of the crystal. Absorption by these color centers is known to limit the performance of Ce^{3+}:$YLiF_4$ laser (ref. 6) and quench the gain in Ce^{3+}:CaF_2 (ref. 5). We have observed strong induced absorption and brown coloration of the Ce-doped lanthanum beryllate (BEL) crystal under 355-nm excitation. The coloration is due to the formation of stable photochromic centers. The centers are produced following a two-step photoionization of the Ce^{3+} ion. In the first step, absorption of a 355-nm photon raises the single optically-active electron of Ce^{3+} from the *4f*-ground state to the lowest-*5d* excited state. An excited-state absorption (ESA) of a second photon from this populated lowest-*5d* state then promotes the electron to the host conduction band. This mobile electron may get trapped at a positively-

charged site and give rise to a stable color center. This article presents a study of the spectroscopic characteristics and growth kinetics of these centers.

A number of characteristics of Ce^{3+}:$La_2Be_2O_5$ (Ce^{3+}:BEL) seemed favorable for its use as a tunable laser crystal in the blue-green spectral region. First, the intense, electric-dipole-allowed *4f-->5d* absorption in Ce^{3+} in this crystal spans the 220-400 nm spectral range with peaks at 275, 312 and 345 nm. The peak absorption cross section at 345 nm is $5.75X10^{-18}$ cm^2. This broadband absorption is suitable for optical excitation of the crystal with conventional light sources. Second, the crystal fluoresces with near-unity quantum efficiency over the 400-650 nm range with a peak emission cross section of $6.0X10^{-18}$ cm^2 at 500 nm. Third, the fluorescence lifetimes of 36 ns at 300 K and 40 ns at 80 K are indicative of small nonradiative losses in the crystal. Fourth, BEL is a good host for rare-earth ions, and large crystals can be grown by the Czochralski technique. In spite of all these promising characteristics, the crystal exhibits net loss instead of gain under optical excitation. Strong ESA transitions and subsequent photochromic center formation completely inhibit laser action in this crystal.

In the subsequent sections we first present a brief description of the experimental arrangement used for studying the characteristics of the photochromic centers. The absorption spectrum of these centers, and the dependence of the number of centers that are formed on the excitation intensity and duration of excitation are then presented. A rate-equation model that assumes a two-photon formation and a single-photon photobleaching of these centers is then used to model their observed growth kinetics.

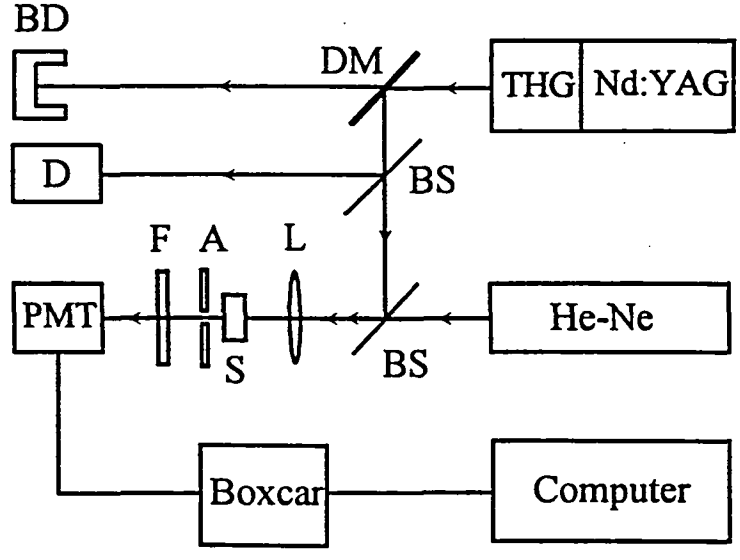

Figure 1. A schematic diagram of the experimental arrangement for studying the growth kinetics of photochromic centers. (Key: A = aperture, BD = beam dump, BS = beam splitter, D = detector, DM = dielectric mirror, F = filter, L = lens, PMT = photomultiplier tube, S = sample, THG = third-harmonic generator.)

EXPERIMENTAL ARRANGEMENT

The Ce^{3+}:BEL crystal used in this study was grown at Allied Signal by the Czochralski technique from a heated mixture of 49.75% La_2O_3, 50% BeO and 0.25% Ce_2O_3 in the melt (ref. 7). The resulting Ce^{3+} doping is 0.5% in the melt and corresponds to an ion concentration of $4X10^{-18}$ cm^{-3}. Cylindrical wafers 19 mm in diameter and 3 mm thick were cut and annealed in an atmosphere of 10% by volume of hydrogen in argon at 1150 °C. The sample used in the experiments reported here had a thickness of 2.5 mm with the *b*-crystallographic axis oriented along the cylinder axis. A similar but undoped BEL sample was used for comparison purpose.

The photochromic centers were grown by irradiating the crystal with 355-nm third harmonic radiation from a Q-switched Nd-doped yttrium aluminum garnet (YAG) laser (Quanta-Ray DCR-3G). The laser operated at a 10-Hz repetition rate with a pulsewidth of ~5 ns. An excite-and-probe absorption measurement technique was used to monitor the temporal evolution of the photochromic color centers. The third harmonic radiation of the Nd:YAG laser was used for exciting the crystal, and the induced absorption was probed by a continuous wave He-Ne laser. A schematic diagram of the experimental arrangement is shown in figure 1.

RESULTS

A. General features and the absorption spectrum

The Ce^{3+}:BEL crystal absorbs strongly at 355 nm with an absorption cross section of ~ $5X10^{-18}$ cm^2. Laser excitation at this wavelength gives rise to photochromic color centers. The presence of these centers is visually observable as the pumped volume of the transparent crystal turns brown in color. No coloration is observed for nonresonant excitation of the Ce^{3+} states, or for 355-nm excitation of the undoped BEL sample. These indicate that Ce^{3+} is directly involved in the formation of the photochromic centers. The coloration is photoreversible. The sample can be bleached back to its original transparent state by illuminating it at wavelengths that are absorbed by the centers, hence, the name photochromic centers. The centers are also bleached by prolonged exposure to room light, but lasts for weeks if the sample is kept in the dark.

The room-temperature absorption spectrum of these stable photochromic centers is displayed in figure 2. The spectrum spans the 220-840 nm range and is characterized by three broadbands with peaks at 640, 380 and 290 nm. Such a wide and broadband absorption is typical of absorption by color centers. Photochromic centers generated both by additive coloration (ref. 8) and by ultraviolet pumping (ref. 5) of Ce^{3+}:CaF_2 crystal also have similar absorption spectra.

B. Growth Kinetics

In order to measure the growth kinetics of stable photochromic centers, we have used the experimental arrangement of figure 1 to monitor the induced absorption of a 632.8-nm He-Ne laser beam as a function of the number of pulses for different intensities of the 355-nm pump beam. Ce^{3+} ions do not absorb at this wavelength, but the photochromic centers have a local absorption peak nearby. The induced absorption of the He-Ne probe beam is thus a direct measure of the photochromic-center concentration. For this measurement, the laser repetition rate was set at 1 Hz. The 355-nm pump beam was focused to a 2-mm diameter spot onto the sample. The He-Ne laser-beam was focused to a 1-mm diameter spot and traversed the sample collinearly with the pump beam. Its intensity was attenuated such that bleaching of the photochromic centers by the probe beam could be neglected. The transmitted intensity of the probe beam was measured 5 ms after each laser shot. This time delay was used to eliminate contributions to induced absorption from excited-state absorption by Ce^{3+} ions, as well as by transient color centers that are also formed. Results of this measurement are presented in figure 3 for several pump-beam intensities.

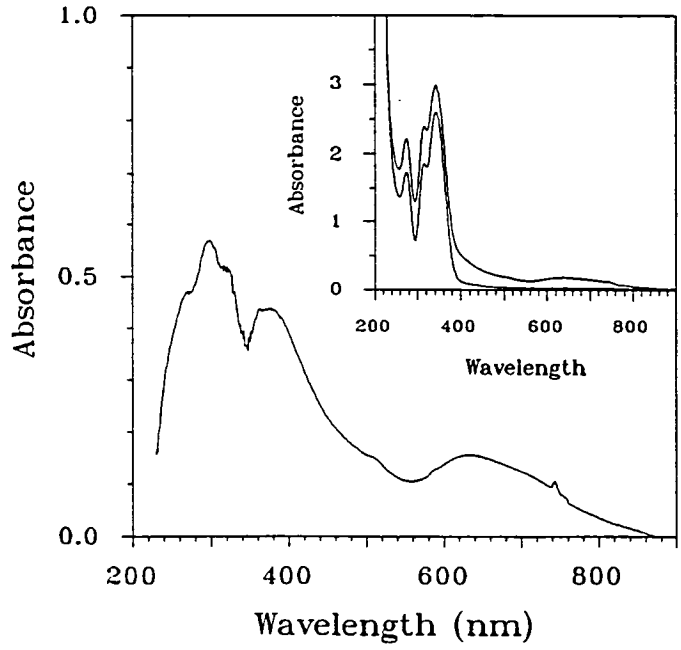

Figure 2. Room-temperature absorption spectrum of stable photochromic centers. Inset shows the absorption spectrum of the sample after (solid line) and before (dashed line) ultraviolet-induced coloration. The absorption spectrum of the photochromic centers is obtained from the difference of these two spectra.

A detailed study of these growth curves reveals two salient features. First, for a given excitation intensity, the induced absorption increases rapidly for the first few laser shots and eventually reaches a steady-state value. The magnitude of this steady-state absorption depends on the intensity of the laser beam. Second, the initial slope of the growth curve that represents the change in induced absorption per laser pulse varies quadratically with the laser intensity for low-intensity levels. This indicates that a nonlinear, two-photon process is involved in the formation mechanism of these centers.

The photochromic centers may be bleached by excitation in its absorption bands which include the 355-nm pump wavelength that is used for their creation, as well as the cerium fluorescence. Further investigation of the photobleaching indicates that it is a single-photon process, and that the bleaching rate is proportional to the number density of the centers.

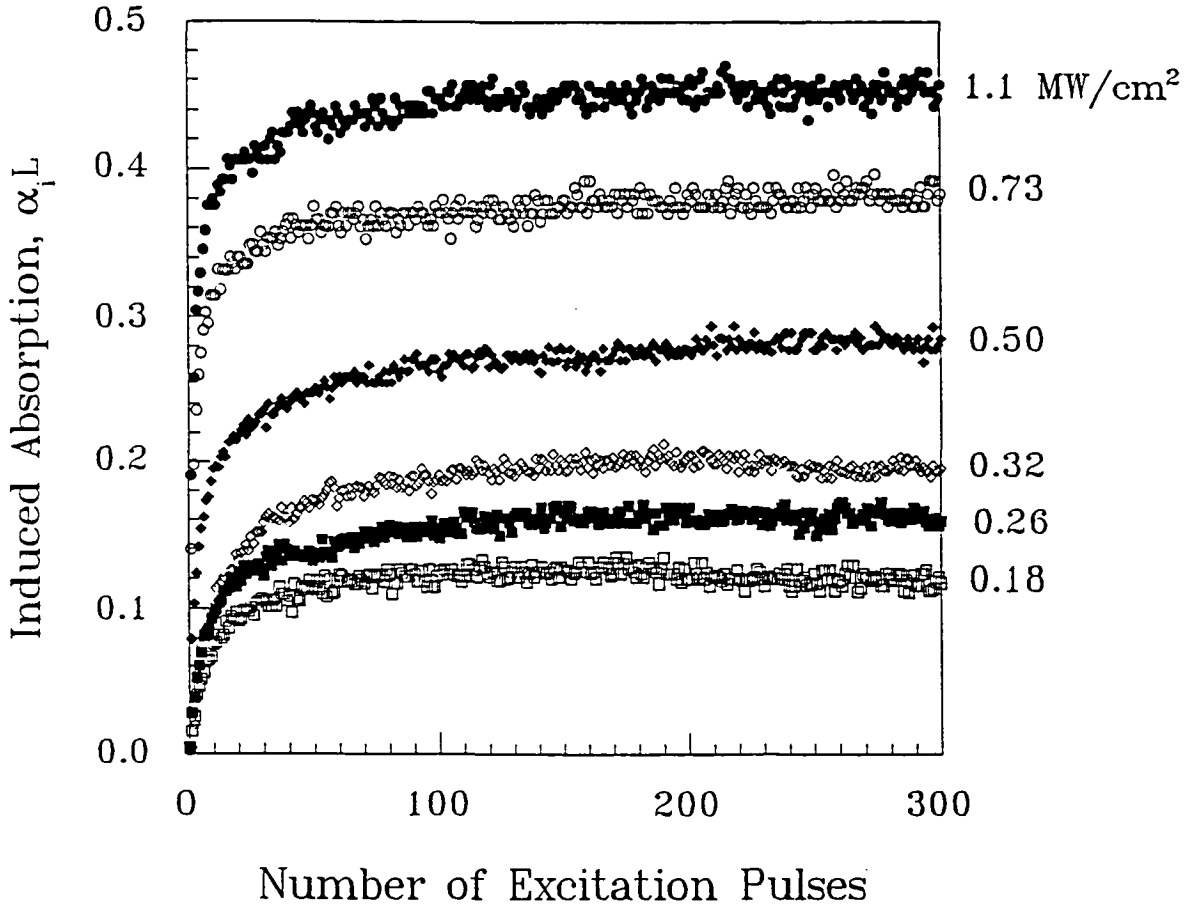

Figure 3. The absorption of a 632.8-nm probe beam due to the growth of photochromic centers as a function of the accumulated number of 355-nm pulses that create the centers.

DISCUSSION

A realistic model of the photochromic centers should incorporate the observed growth kinetics, saturation of induced absorption, intensity dependence, and photobleaching. The absorption spectrum of undoped BEL indicates the onset of valence-->conduction band absorption to be at ~ 40 000 cm^{-1} (250 nm). The lowest absorption band of Ce^{3+} peaks at 345 nm, well below the conduction-band edge. However, a two-photon process can readily raise the single, optically-active electron of the ion to the conduction band. The photoionized electron in the conduction band has sufficient mobility to wander and get attached to a nearby charge-trapping site forming a color center. Similar mechanism has been invoked to model the creation of photochromic centers in Ce-doped CaF_2 (ref. 5) and $YLiF_4$ (ref. 6). Along the line of those works, we use a rate equation to describe the formation kinetics of photochromic centers in Ce:BEL

$$dn/dt = (n_0 - n)NAI^2 - nBI, \qquad (1)$$

where n is the number density of photochromic centers, n_0 is the initial density of trap sites, N is the

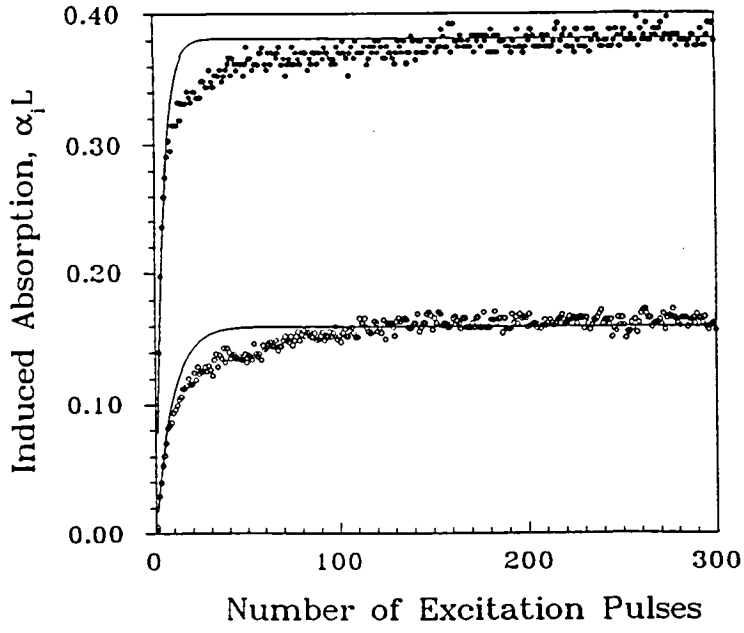

Figure 4. Theoretical fit (solid line) of the measured growth kinetics of photochromic centers to an analytic solution of the rate equation assuming a square pump pulse. The upper curve is for a pump intensity of 0.73 MW/cm^2 and the lower for 0.26 MW/cm^2.

concentration of Ce ions, I is the pump intensity, and A and B are creation and photobleaching coefficients, respectively. A fit of the experimental growth curve to this rate equation for two different pump intensities is shown in figure 4. It is evident that the rate-equation model explains the initial rise and the saturation behavior nicely. However, the fit is not satisfactory around the turning point. This implies that the formation kinetics of photochromic centers are more involved than that provided by the simple model.

The exact nature of the charge-trapping sites in this crystal is not known. More work is necessary for their characterization. It should be pointed out that absorption by this stable photochromic center is not the only loss mechanism in this crystal. Absorption by transient color centers and excited-state absorption contribute strongly to the optical loss at shorter time scales. A detailed discussion of these loss mechanisms is beyond the scope of this contribution, and will be presented in a forthcoming publication.

REFERENCES

1. Ehrlich, D. J.; Moulton, P. F.; and Osgood, R. M., Jr.: Ultraviolet Solid-State Ce:YLF Laser at 325 nm. *Opt. Lett.*, vol. 4, 1979, pp. 184-186.
2. Ehrlich, D. J.; Moulton, P. F.; and Osgood, R. M., Jr.: Optically Pumped Ce:LaF_3 Laser at 286 nm. *Opt. Lett.*, vol. 5, 1980, pp. 339-341.
3. Dubinskii, M. A.; Shemashko, V. V.; Naumov, A. K. ; Abdulsabirov, R. Yu.; and Korableva, S. L.: Ce^{3+}-doped Colquirite: A New Concept of All Solid-State Tunable Ultraviolet Laser. *J. Mod. Opt.*, vol. 40, 1993, pp. 1-5, and relevant references therein.
4. Pogatshnik, G. J.; Gayen, S. K.; and Hamilton, D. S.: Laser Induced Defect Centers in Ce^{3+}:CaF_2. *J. Lumin.*, vol. 31/32, 1984, pp. 251-253.
5. Pogatshnik, G. J.; and Hamilton, D. S.: Excited-State Photoionization of Ce^{3+} ions in Ce^{3+}:CaF_2. *Phys. Rev. B.*, vol. 36, 1987, pp. 8251-8257.
6. Lim, K. S.; and Hamilton, D. S.: Optical gain and loss studies in Ce^{3+}:$YLiF_4$. *J. Opt. Soc. Am. B*, vol. 6, 1989, pp. 1401-1406.
7. Gualtieri, D. M.: Cathodoluminescence of Ce:$La_2Be_2O_5$ Single Crystals, *J. Lumin.*, vol. 60/61, 1994, pp. 127-130.
8. Staebler, D. L.; and Schnatterly, S. E.: Optical Studies of Photochromic Color Centers in Rare-Earth-Doped CaF_2. *Phys. Rev. B.*, vol. 3, 1971, pp. 516-526.

AGGREGATION-ENHANCED RAMAN SCATTERING BY A WATER-SOLUBLE PORPHYRIN

Daniel L. Akins

The Center for Analysis of Structures and Interfaces

Department of Chemistry

The City College of The City University of New York

—ABSTRACT—

Much interest in our laboratory has focused on aggregation of organic compounds, particularly cyanine dyes and porphyrins. For this discussion we have applied absorption and Raman scattering spectroscopies to characterize aggregated TSPP (tetrakis-(p-sulfonatophenyl)porphyrin) in homogeneous aqueous solution. Based on concentration, pH and ionic strength dependence of TSPP absorption, we deduce that aggregation evolves through the formation of TSPP diacid and that the diacid is the repeating unit in the aggregate. The Raman bands of TSPP in strongly acidic solution lead us further to conclude that vibrations of adjacent molecules are perturbed in a fashion that is consistent with the pyrrolic ring in the porphinato macrocycle being ruffled, and that two aggregate arrangements occur: specifically J- and H-type aggregates. Furthermore, aggregation enhancement is advanced as a viable mechanism to explain enhanced Raman scattering for homogeneous aqueous phase TSPP, where the surface-enhancement mechanism is not applicable.

I. Introduction

Aggregated molecules play crucial roles in nature and have important technological applications. In particular, aggregates involving porphyrins and their derivatives are found in biological systems where they function to convert optical radiation into chemical energy and promote charge transfer reactions [1]. Also, dye aggregates (spec., the cyanines) have been used as spectral sensitizers, principally, for silver halide semiconductor materials [2], as organic photoconductors [3], and, recently, much interest has centered on their nonlinear optical susceptibilities [4,5]—since aggregated molecules may have enhanced nonlinear responses and would find utility in nonlinear optical devices [6-8].

Research from this laboratory has focused on molecular excitons associated with aggregate structures, and electron-transfer dynamical processes involving aggregated species as one of the reactants. It has proved necessary to put forth a quantum theory derived analytical intensity expression to explain the occurrence of various vibrational Raman bands as well as an enhancement of intensities for aggregated molecules (viz., "aggregation-enhancement") [9,10].

In the present paper, we provide a brief discussion of some of the deductions that emanate from aggregation-enhanced Raman scattering theory. We then detail some spectroscopic investigations for a water-soluble porphyrin, spec., sulfonated tetraphenylporphine (TSPP), see Fig. 1, which we construe to form two types of aggregates, the so-called J- and H-aggregates [11], in acidic solution. It is of particular note that aggregates of TSPP formed in homogeneous, aqueous solution insure the absence of surface plasmon resonances. Such resonances are a fundamental aspect of the enhancement mechanism attributable to protuberances on substrates (i.e., surface-enhanced Raman scattering, SERS), and the TSPP system is nearly an ideal one to test the aggregation-enhancement model.

Our major conclusions for the aggregates of TSPP are (a) protonation-induced change in the alignment of phenyl group attached to the porphyrin macrocycle (from an almost perpendicular to a nearly coplanar orientation, see Fig. 1) promotes aggregation, (b) "ruffling" of the porphyrin macrocycle is advanced to explain the existence and spectral shifts of certain Raman lines, and (c) aggregation-enhancement explains Raman band intensities and their dependencies on excitation frequency.

In the following section, we discuss "aggregation-enhancement," as developed by the author over the past several years [9]. This discussion begins with the elaboration of various concepts of molecular vibro-exciton theory for linear aggregates, including the determination of an analytical expression for the vibro-excitonic energies and wave functions. These analytical expressions are then utilized in the Raman scattering problem, and can be used to determine, among other things, band selection rules and Raman enhancement factors relative to intensities of monomer bands. In section III we provide details of our experimental apparatus and procedures. In section IV we discuss absorption and Raman evidence that points to the nature of the TSPP aggregates that are formed, and under what conditions. Finally, in section V we summarize our findings.

II. Raman Scattering by Aggregated Molecules

Molecular Vibro-Exciton Theory: The theory as developed here applies to a finite, linear aggregate structure consisting of N molecules. The quantum mechanical Hamiltonian which describes the internal system of N molecules which can mutually interact through a potential term V is given by eq 1,

$$\mathrm{H} = \sum_{n=1}^{N}\left(H_n + \sum_{m>n} V_{mn} \right) \tag{1}$$

where H_n represents the kinetic energy operator for molecule n, and V_{mn} is the interaction potential between molecules m and n, where m is any of the other molecules in the aggregate besides molecule n.

The vibronic wave function for an individual molecule n is taken to be

$$\psi_{ni}(\mathrm{q},\mathrm{Q}) = \psi_n(\mathrm{q},\mathrm{Q}_0)\chi_{ni}(\mathrm{Q}) \tag{2}$$

where i is a composite quantum number which specifies the number of vibrational quanta of excitation with known distribution among the vibrational modes. Equation 2 is the crude adiabatic Born-Oppenheimer approximation [9], where q is a composite spatial coordinate of the electrons, Q represents the normal coordinates, and Q_0 is the normal coordinate for the ground-state equilibrium configuration. Also, ψ is here a many electron wave function which depends on the coordinates and spins of the π-electrons,

while χ is the vibrational wave function, which, more explicitly, in the zeroth approximation is defined as

$$\chi_{ni}(Q) = \prod_{\kappa} \chi_{ni_\kappa}(Q_\kappa) \quad , \tag{3}$$

where i_κ specifies the number of vibrational quanta i in mode κ, and Q_κ is the normal-coordinate variable.

The solutions for the energies and wave functions, when only the next nearest neighbor interaction is considered, are the following:

$$\varepsilon_k = 2M \cos\frac{\pi k}{N+1}, \quad k = 1, 2, \ldots, N \quad , \tag{4}$$

$$\Psi_{ki} = \left[\frac{2}{(N+1)}\right]^{1/2} \sum_n \Theta_{ni} \sin\frac{\pi nk}{N+1} \quad , \text{where} \tag{5}$$

$$\Theta_{ni} = \left((SN)!\right)^{-1/2} \sum_{\nu} (-1)^{\nu} P_{\nu} \Phi_{ni} \tag{6}$$

In the above expressions, k is the electronic quantum label which can have integer values 1 to N, the sum over n (the molecule label) also goes from 1 to N, S is the number of π-electrons, $\mathbf{P}_\nu$ is the antisymmetrization operator, and ν is the number of pair permutations required to recover an arbitrary fiducial arrangement of electrons among the molecules in the aggregate. Also, Φ represents a particular arrangement in which a quantum of energy exists among the available vibronic states of the N aggregated molecules.

Raman Scattering Theory: From Craig and Thirunamachandran [12], the Raman scattering intensity in a particular direction, as defined by the scattered radiation's wave vector κ', is given by

$$I(\kappa') = \frac{\tilde{N} I \kappa'^4}{16\pi^2 \varepsilon_0{}^2} \left| \sum_r \left\{ \frac{\left(\frac{r_{mr}}{\mu} \cdot \bar{e}'\right)\left(\frac{r_{r0}}{\mu} \cdot \bar{e}\right)}{E_{r0} - hc\kappa} + \frac{\left(\frac{r_{mr}}{\mu} \cdot \bar{e}\right)\left(\frac{r_{r0}}{\mu} \cdot \bar{e}'\right)}{E_{r0} + hc\kappa'} \right\} \right|^2 \tag{7}$$

where $\tilde{N}$ is the number of scattering centers (i.e., aggregates for this problem); the sum is over excited electronic states r; the μ's are transition dipole moment vectors; the e's are microscopic electric field strength vectors; and E_{r0} is the energy difference between the upper state r and the ground state 0.

Expressed in terms of the polarizability, the Raman intensity becomes

$$I(\kappa') = \frac{\tilde{N} I \kappa'^4}{16\pi^2 \varepsilon_0{}^2} e'_i e_j e'_k e_l \, \alpha_{ij}{}^{m0}(\omega, \omega') \overline{\alpha}_{kl}{}^{m0}(\omega, -\omega') \tag{8}$$

where i, j, k, and l are laboratory coordinates.

Upon applying the Born-Oppenheimer approximation to describe the states of the molecular system, and concerning ourselves with vibrational Raman scattering where the molecule after scattering radiation remains in its ground electronic state while the vibrational state changes from initial value v" to final value v', the polarizability assumes the form

$$\alpha_{ij}{}^{0v',0v''} = \sum_{r,v} \left\{ \frac{\langle \chi_{0v'} | \langle \varphi_0 | \mu_i | \varphi_r \rangle | \chi_{rv} \rangle \langle \chi_{rv} | \langle \varphi_r | \mu_j | \varphi_0 \rangle | \chi_{0v''} \rangle}{E_{r0} + \varepsilon_{rv,0v''} - hc\kappa} + \frac{\langle \chi_{0v'} | \langle \varphi_0 | \mu_i | \varphi_r \rangle | \chi_{rv} \rangle \langle \chi_{rv} | \langle \varphi_r | \mu_j | \varphi_0 \rangle | \chi_{0v''} \rangle}{E_{r0} + \varepsilon_{rv,0v''} + hc\kappa'} \right\} \tag{9}$$

where E_{r0}, now, is the electronic energy difference; $\varepsilon_{rv,0v''}$ is the vibrational energy difference; the χ's are vibrational wave functions; the φ's are electronic wave functions; and rv labels the intermediate vibronic state.

Albrecht's [13] development of the Herzberg-Teller correction to the excited electronic states is now applied. The electronic transition moment at a given nuclear configuration, for a typical transition-moment matrix element, becomes

$$\langle \varphi_r | \mu_j | \varphi_0 \rangle = M^0_{0,r} + \sum_s{}' \lambda_{rs}(\mathrm{Q}) \, M^0_{0,s} \tag{10}$$

where the M's are electric dipole moments integrated over electronic coordinates for the ground-state configuration; λ_{rs}, from first-order perturbation theory, is

$$\lambda_{rs}(\mathrm{Q}) = \left(\sum_\alpha h^\alpha_{rs} \mathrm{Q}_\alpha \right) \left(\Delta E^0_{rs} \right)^{-1} \tag{11}$$

in which h_{rs}^{a} is a coupling term between electronic states r and s for the molecule with equilibrium ground-state configuration; Q_α is the displacement of mode α; $\Delta E_{rs}^0 = E_r^0 - E_s^0$ is the electronic energy difference, again, for the molecule with equilibrium ground-state configuration; and the prime on the summation over s excludes state r from the sum.

Upon substituting the molecular vibro-excitonic wave functions, as expressed by eq 5, into eq 9, and utilizing Albrecht's notation, we find that the polarizability can be expressed as follows:

$$\alpha_{ij}^{0v',0v''} = A + B + C \quad , \tag{12}$$

where A, B, and C are analytical terms, referred to as Albrecht A-, B-, and C-terms, respectively.

Some deductions based on the form of the Albrecht terms are (i) enhanced Raman scattering, vis-à-vis the monomer's scattering intensity, is due to the effective number of molecules forming the aggregate; (ii) B-term bands can be used to normalize A-term bands to surface concentration as well as excitation frequency when a substrate is used [14]; (iii) when off-resonance excitation is used, all Raman bands are fundamentals; (iv) resonance in band intensities associated with tuning through an aggregate absorption band may allow determination of dipole-dipole interaction energy for molecules in the aggregate [15]; and (v) again when a substrate is used, surface potential dependence of band intensities may enable determination of excited-state transition dipole moments (when B-term bands are used to normalize A-term bands) [10].

In addition, analysis of widths of Raman bands that exhibit resonance enhancement (A-term bands) when the excitation frequency is tuned into coincidence with the absorption band(s) leads to a dephasing argument (i.e., transitions between excitonic state sublevels) to explain relative widths [16] as well as relative lifetimes of the pertinent states [17].

III. Experimental Section

The water soluble porphyrin studied in this work is free base meso-tetrakis(p-sulfonatophenyl)porphine (TSPP), which was purchased from Porphyrin Products, Inc., Utah, and used without further purification. All measurements were conducted at room temperature, ca. 22 C. The molecular structure of TSPP is provided in Fig. 1.

Solutions were prepared using distilled and deionized water; pH values were adjusted by addition of 0.1 N NaOH or 0.1 N HCl; and ionic strengths were varied through addition of KCl. Solutions were kept in the dark for 6-18 hours prior to spectral measurements to allow species equilibration.

All absorption spectra were recorded using a Perkin-Elmer, Lambda 19, UV-vis-NIR spectrometer. Raman scattering of samples contained in quartz cells was excited at 488 and 514.5 nm with laser radiation provided by a Coherent, Innova 200, argon-ion laser. Raman spectra were recorded using a Spex 1877, 0.6 m triple-spectrometer, coupled to a charge-coupled-device (CCD) detector (Spectrum-1) cooled to 140 K with liquid nitrogen. Reported Raman spectra, in general, correspond to 64 scans with a 0.5-s integration period per scan, and have been refined by background subtraction—by exporting files to analysis software (Igor) from Wavematrics (Lake Oswego, Oregon). Additionally, all reported Raman spectra have a resolution of ca. ± 2 cm^{-1}.

IV. Results for TSPP

The absorption spectrum of TSPP in water is sensitive to a number of solution properties. As displayed in Fig. 2, the absorption spectrum of TSPP is dramatically different for solution pH values above or below a "threshold" value of about 5. For a solution of pH above this threshold, the absorption spectrum of TSPP is that typical for most porphyrin free bases, i.e., it consists of an intense Soret band (B band) at 413 nm and four very weak Q bands at 648, 580, 552 and 515 nm (Q_1, Q_2, Q_3 and Q_4, respectively).

The absorption spectrum of TSPP as a function of ionic strength is shown in Fig. 3.

As indicated by the growth of the sharp absorption band at 490 nm at the expense of the absorption bands characteristic for protonated porphyrin free base, water-soluble TSPP has been shown to undergo aggregation in low-pH solution via formation of the diacid [18].

Raman measurements for low pH systems have provided information on structural details for aggregated TSPP, especially through assignments of low-frequency bands—far beyond that possible from absorption studies, but not sufficient to accurately define aggregate structure. However, through studies of other porphyrins, especially tetraphenylporphine, TPP (the simplest meso-substituted phenylporphyrin), one might infer structural characteristics of aggregated TSPP. In particular, for TPP diacid, X-ray

crystallographic data [19] convincingly indicates that protonation at the inner pyrrolic N-atom has little effect on the inherent geometry of the pyrrole ring or on the phenyl substituent, but does lead, as mentioned earlier, to twisting of the meso-substituted phenyl group toward a near coplanar orientation (as opposed to its original near perpendicular orientation) with respect to the porphinato macrocycle; it also destroys the planarity of the porphinato macrocycle by tilting the pyrrole rings alternately up and down (i.e., "ruffles" the surface). This ruffling is probably caused by steric hindrance of the four hydrogen atoms as well as electrostatic repulsion of the inner, positively charged N atoms.

By transferring the conclusion for the TPP Raman spectrum to that for TSPP, we conclude that the low frequency band at 242 cm^{-1} is generated by N···N stretching, and is down-shifted from 310 cm^{-1} attributed to the monomeric TSPP free base [18].

Given the above assignment for the 242-cm^{-1} band, it is reasonable to assign the 316-cm^{-1} band to the same radial N···N stretching mode, but upshifted from the parent TSPP diacid band as a result of the diacid being in a different aggregate environment. Since the lower energy aggregate (i.e., the J-aggregate) is expected to give rise to a lower energy phonon mode [16], we associate the 242 cm^{-1} band with the J-aggregate. The higher energy band at 316 cm^{-1} is attributed to N···N stretching of the diacid in the higher energy environment of the H-aggregate. The picture that emerges is that the protonated macrocycle in the J-aggregate can ruffle and thus have a bathochromic shift in its (nearly) out-of-plane N···N stretching, while the same motion is constricted in the H-aggregate, giving rise to a hypsochromic shift.

As a result of the above assignments of the low-frequency bands, it is possible to guess at structures for both the J- and H-aggregates. A low energy interaction for a linear aggregate would have adjacent molecules offset in a spread card-deck arrangement with the sulfonato group positioned over the macrocycle (see Fig. 4). Such an arrangement would lead to increased N···N separation, with a resultant red-shift. A second linear arrangement in which the molecules are nearly stacked one-above-the-other would result in repulsion between adjacent N···N groups because of the decreased interaction distance, leading to a blue-shift. We further note that the C_m-Φ out-of-plane vibrations would be subject, in the picture presented, to the same interactions, and would experience blue and red shifts.

V. Conclusion

The aggregation of meso-tetrakis(p-sulfonatophenyl)porphine in aqueous solution has been demonstrated by the appearance of a sharp absorption band at 490 nm accompanied by a broader absorption band at 422 nm. The absorption measurements further reveal that aggregation takes place only in solution of pH<5, and is promoted by increasing the ionic strength.

The Raman spectral data of TSPP in acidic aqueous solution (pH between 4 and 5) is interpreted as indicating that TSPP diacid in the aggregate can be viewed as forming two quasi-planar, linear aggregates. Both aggregates have the pyrrolic rings in the porphinato macrocycle that are alternately ruffled up and down; however, one can be viewed as forming a linear, staggered card-deck structure, with the opposite peripheral phenyl groups (in the aggregate formation direction) overlapping adjacent porphinato macrocycles, while the other can be viewed as a stacked card-deck arrangement with phenyl and macrocycle groups (in the linear aggregate formation direction) nearly directly above and below one another. These two aggregate structures are interpreted as giving rise, respectively, to linear J- and H-aggregates [11], with absorptions occurring at 490 and 422 nm, respectively.

A very important determination is that the Raman spectrum of aggregated, homogeneous aqueous phase TSPP meets the expectations defined by aggregation enhancement theory [9]. The intensity of Raman bands of the porphinato macrocycle is essentially the same whether or not excitation that is near resonant with the visible absorption bands of the aggregate is used (off-resonant spectra have not been shown here); these bands, as a result, meet the conditions that define them as emanating from the Albrecht *B*-term contribution to the polarizability. Two Raman bands (at 242 and 316 cm^{-1}), which are resonance Raman active for excitation close to those due to the aggregates (422 and 490 nm), are attributable to the Albrecht *A*-term of the polarizability. Hence, we conclude that aggregation enhancement is a viable mechanism to explain enhanced Raman scattering, especially in systems where the SERS mechanism is not applicable.

Acknowledgment

Support for this research by the National Science Foundation (NSF) under Grant RII-8802964 is gratefully acknowledged.

REFERENCES

1. Feher, G.; Okumura, M. Y.: In "The Photosynthetic Bacteria"; Clayton, K.; Sistrom, W.F., eds.; Plenum, New York, 1978.

2. Gilman, P. B.: Use of Spectral Sensitizing Dyes to Estimate Effective Energy Levels of Silver Halide Substrates. *Photo. Sci. Eng.*, vol. 18, 1974, p. 418.

3. Borsenberger, P. M.; Chowdry, A.; Hoesterey, D. C.; W. Mey: An Aggregate Organic Photoconductor. Part 2. Photoconduction Properties. *J. Appl. Phys.*, vol. 44, 1978, p. 5555.

4. Hanamura, E.: Very Large Optical Nonlinearity of Semiconductor Microcrystallytes. *Phys. Rev. B.*, vol. 37, 1988, p. 1273.

5. Sasaki, F.; Kobayashi, S.: Anomalous Excitation Density Dependence of Nonlinear Optical Responses in Pseudoisocyanine J-Aggregates. *Appl. Phys. Lett.*, vol. 63, 1993, p. 2887.

6. Wang, Y.: Efficient Second Harmonic Generation from Low Dimensional Dye Aggregates in Thin Polymer Films. *Chem. Phys. Lett.*, vol. 126, 1986, p. 209.

7. Wang, Y.: Resonant Third-Order Optical Nonlinearity of Molecular Aggregates with Low Dimensional Excitons. *J. Opt. Soc. Am. B.*, vol. 8, 1991, p. 981.

8. Kobayashi, S.: Large Optical Nonlinearity in Pseudoisocyanine J-Aggregates. *Mol. Crys. Liq. Crys.*, vol. 217, 1992, p. 77.

9. Akins, D. L.: Theory of Raman Scattering by Aggregated Molecules. *J. Phys. Chem.*, vol. 90, 1986, p. 1530.

10. Akins, D. L.; Akpabli, C. K; Li, X.: Surface Potential Dependence of Enhanced Raman Bands of Aggregated Cyanine Dyes. *J. Phys. Chem.*, vol. 93, 1989, p. 1977.

11. Herz, A. H.: Aggregation of Sensitizing Dyes in Solution and Their Adsorption onto Silver Halides. *Colloid. Interfacial Sci.*, vol. 8, 1977, p. 237.

12. Craig, D. P.; Thirunamachandran, R.: "Molecular Quantum Electrodynamics"; Academic: New York, 1984.

13. Albrecht, A. C.: On the Theory of Raman Intensities. *J. Chem. Phys.*, vol. 34, 1961, p. 1476.

14. Akins, D. L.; Zhu, H. -R.: Raman Excitation Spectra of Coupled Intramolecular-Intermolecular Vibronic Modes of Aggregated 4,4'-Cyanine. *Langmuir*, vol. 8, 1992, p. 546.

15. Akins, D. L.; Lombardi, J. R.: Excitation Wavelength Dependence of Raman Bands of Aggregated Molecules. *Chem. Phys. Lett.*, vol. 135, 1987, p. 495.

16. Akins, D. L.; Zhuang, Y. H.; Zhu, H. -R.; Liu, J. Q.: Raman Excitation Spectra and the Structure of Adsorbed 2,2'-Cyanine. *J. Phys. Chem.*, vol. 98, 1993, p. 1068.

17. Akins, D. L.; Özçelik, S.: "Structure and Superradiance of J-Aggregated 2,2'-Cyanine Adsorbed onto a Vesicle Surface," to be submitted to J. Phys. Chem., 1994.

18. Akins, D. L.; Zhu, H. -R.; Guo, C.: Absorption and Raman Scattering by Aggregated *meso*-Tetrakis(*p*-sulfonatophenyl)porphine. *J. Phys. Chem.*, vol. 98, 1994, p. 3612.

19. Stone, A.; Fleischer, E. B.: The Molecular and Crystal Structure of Porphyrin Diacids. *J. Am. Chem. Soc.*, vol. 90, 1968, p. 2735.

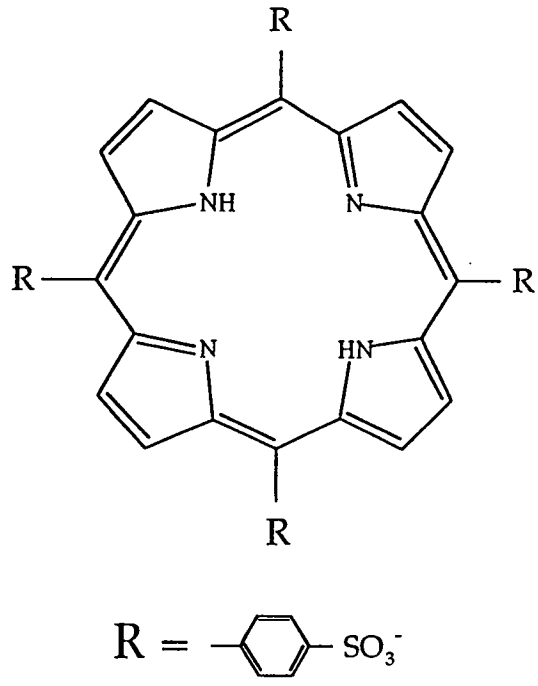

Fig. 1: Structure of meso-tetrakis(p-sulfonatophenyl)porphine (TSPP).

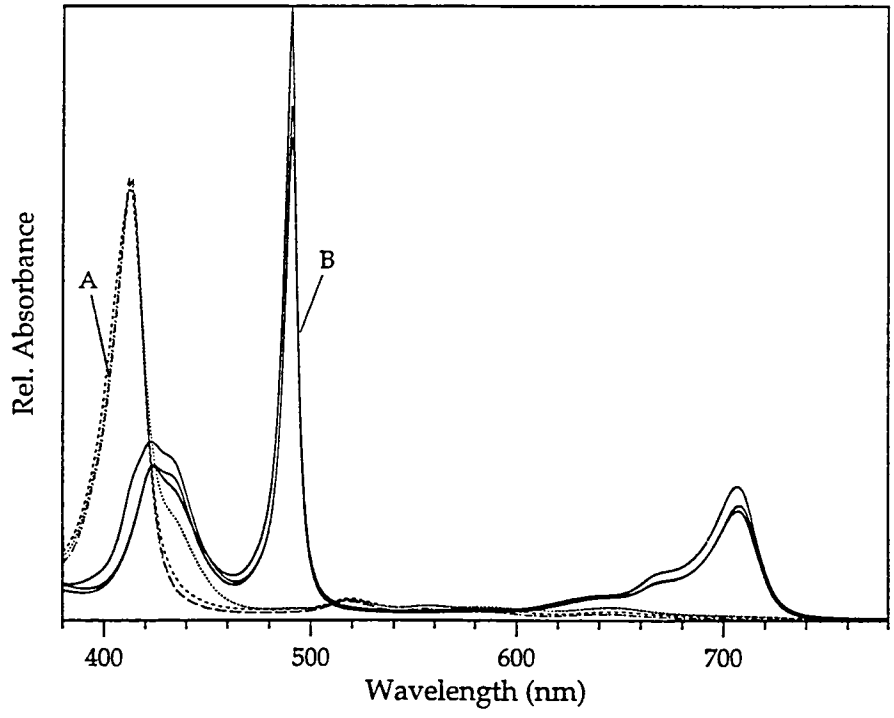

Fig. 2: Absorption spectra of 5×10^{-5} M TSPP in aqueous solutions of ionic strength 0.1 (by addition of KCl) and different pHs. (A) Broken-line spectra labeled for three (representative) spectra with pHs lying between 12.5 and 5.2. (B) Three solid-line (representative) spectra labeled are for pHs between 4.2 and 1.6. Absorption path length was 1 mm in all cases.

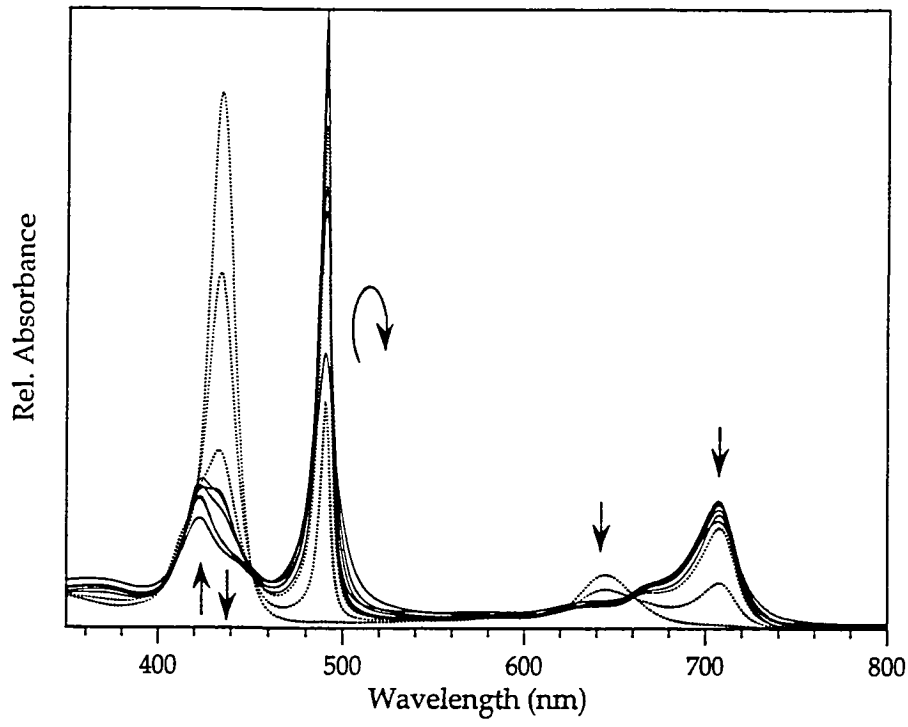

Fig. 3: Ionic strength dependence of absorption of TSPP in aqueous solution. TSPP concentration of 5.0×10^{-5} M, pH=4.3, absorption path length of 1 mm. The arrows show the trends of the various absorbances with increasing ionic strength. The curved arrow indicates that the absorbance at 490 nm is found to reach a maximum value then to decrease for higher ionic strengths. For reference purposes, it is noted that the top three Soret band absorbances, corresponding to dotted line spectra, occur for KCl concentrations of 0, 25 mM, and 50 mM.

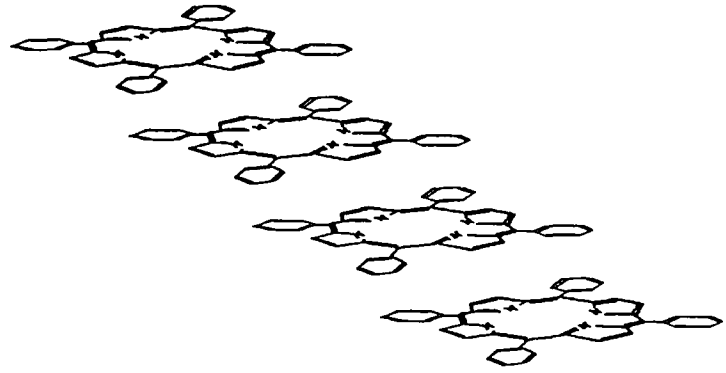

J - Aggregate

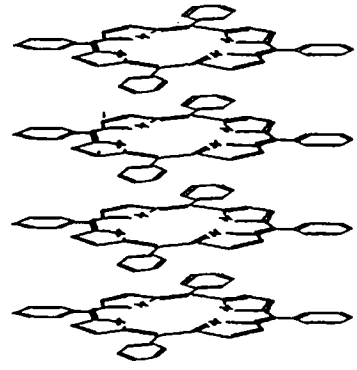

H - Aggregate

Fig. 4: Suggested structural alignment of TSPP forming the J- and H-aggregates.

SUPERRADIANCE OF J-AGGREGATED 2,2'-CYANINE ADSORBED ONTO A VESICLE SURFACE

Daniel L. Akins and Serdar Özçelik†

Center for Analysis of Structures and Interfaces (CASI)

Department of Chemistry

The City College of The City University of New York

New York, NY 10031

ABSTRACT

Phospholipid vesicles are used as substrates to form adsorbed aggregates of 2,2'-cyanine, also referred to as pseudoisocyanine (PIC). In this paper, we report photophysical parameters of two putative adsorbed aggregates species (cis- and trans-aggregates, relating to their makeup from mono-cis and all-trans stereoisomers, respectively). Phase modulation picosecond fluorescence decay measurements reveal that superradiance and energy transfer are dominant features controlling photophysical processes. Superradiance, coherence size, energy transfer and exciton-phonon coupling are discussed for the two types of aggregates; as regards photophysical parameters, the fluorescence lifetimes, fluorescence quantum yields, and nonradiative rate constants are determined. It is suggested that structure plays the crucial role in excited state dynamics.

† Tübitak NATO Science Predoctoral Fellow.

I. Introduction

Aggregated molecules play crucial roles in nature and have important technological applications. Aggregates are found in biological systems where they function to convert optical radiation into chemical energy and promote charge transfer reactions [1]. Dye aggregates have been used as spectral sensitizers (principally for silver halide semiconductor materials) [2], as organic photoconductors [3], and, recently, much interest has centered on their nonlinear optical susceptibilities [4,5], since aggregated molecules with enhanced nonlinear responses find utility as materials for use in nonlinear optical devices [6-8].

Aggregation of cyanine dyes was first reported by Jelley [9] and Scheibe [10], in 1936, who found that concentrated aqueous solutions of 1,1'-diethyl-2,2'-cyanine exhibit an absorption which is not present in dilute solution and is red-shifted and narrowed relative to monomer absorption bands, the so-called J-band attributed to aggregated molecules. Many other cyanine dyes exhibit similar spectral properties.

In terms of photodynamics, recently, superradiance was observed for 1,1'-diethyl-2,2'-cyanine (also referred to as pseudoisocyanine, PIC) in ethylene glycol/water glass at low temperature [11,12], and adsorbed onto an AgBr surface at room temperature [13]. The occurrence of superradiance for the dye aggregates suggests the concept of an effective coherence size for the emitting species [14-16]: molecules which define the coherence size are considered to be strongly coupled and respond in phase to optical radiation. As a result, the radiative decay rate is increased by a factor dependent on the effective coherence size, and, often, enhanced nonlinear optical response is found.

In this laboratory, Raman scattering studies of aggregated 1,1'-diethyl-2,2'-cyanine iodide (hereinafter referred to as 2,2'-cyanine) on silver electrodes [17-24] have been utilized to gain insight into the structures of aggregates on metallic surfaces. More recently, cyanines have also been shown to aggregate on phospholipid vesicle surfaces [25]. The structure, alignment, and photodynamics of cyanine dyes on such surfaces can provide reference type information for cyanines adsorbed onto metallic and semiconductor surfaces, and, also, might represent model systems for investigating electron transfer structures for chromophores intercalated into lipids [26].

In this paper, we study the aggregation behavior of 2,2'-cyanine adsorbed onto phospholipid vesicle surfaces formed in aqueous solutions containing L-α-dimyristoylphosphatidylcholine (DMPC) and dicetyl phosphate (DCP) (see Figure 1 for structures). The results of fluorescence lifetime and quantum yield measurements are discussed.

We report measurements of photophysical parameters of J-aggregated 2,2'-cyanine adsorbed onto the vesicle surface. Steady-state and phase-modulation, fluorescence spectroscopies are used for this study, and support the presence of two aggregate conformers, heretofore referred to by us as cis- and trans-aggregates [26], for which the relative orientations of ethyl groups attached to the nitrogen heteronuclei of the monomer, either on the same or opposite side of the molecular plane, defined cis- and trans-, respectively. More recently [27], however, we understand the cis/trans makeup of aggregates in terms of a somewhat different picture. Our new understanding derives from current photophysical studies in our laboratory for cyanine dyes at "low" concentrations, where dimers and other H-type aggregates are found to occur. We have, in agreement with others, ascertained that, in general, stereoisomers of the monomeric species exist, with the dominant stereoisomer being the so-called all-trans species and the stereoisomer of lower concentration being referred to as the mono-cis isomer [28-36]. Henceforth in this manuscript, the designations trans- and cis-aggregate will refer to aggregates composed of the trans- and mono-cis-configurational stereoisomers, respectively.

We conclude from the accumulated information that superradiance and energy transfer are the principal determinants of excited-state dynamics.

II. Experimental

Two dimensional molecular structures of the phospholipids and of 2,2'-cyanine are shown in Figure 1. 2,2'-cyanine was purchased from Aldrich Chemical Company and the phospholipids from Sigma Chemical Company. In the studies reported here, all compounds were used without further purification and all experiments were conducted at room temperature.

Dye solutions were prepared using distilled and deionized water. pH values were adjusted by addition of 0.1 N NaOH. Vesicle solutions were made following a recipe given in Ref. 25, briefly: the chloroform solutions of DMPC and DCP were slowly evaporated at 50-70° C to remove solvent; thin films were

hydrated with distilled and deionized water at 70° C and sonicated in a bath type sonicator for 1-2 minutes to obtain homogeneous solutions. The pH of the vesicle solutions prepared by this method was ca. 3.0, and not further adjusted. The vesicle size was measured using a photon correlation spectrometer, and the average diameter was found to be ca. 400 nm [37].

Absorption spectra were recorded using a Perkin-Elmer Lambda 19, UV-vis/NIR spectrometer. Steady-state fluorescence, fluorescence excitation and synchronously scanned luminescence spectra were acquired using a SPEX Fluorolog-τ2 spectrofluorometer.

Principal components of the Fluorolog are the following: a 450 W xenon incandescent lamp coupled to both a single grating excitation and an emission spectrometer; a Pockels cell which modulates the excitation light from 0.5 MHz to 300 MHz for lifetime studies (see below); a T-box sampling module, including an automated, four-position sample changer; and two Hamamatsu model R928-P photomultiplier tubes, one used as a reference detector, and operated in the direct-current acquisition mode, and the other operated in the photon-counting acquisition mode. Scanning of excitation, emission, or both simultaneously are under computer control (SPEX DM3000F software run on a SPEX-486 PC). All data are stored and analyzed using vendor software.

The fluorescence quantum yields were determined relative to rhodamine 6G in ethanol ($\Phi = 0.90$) as the reference [38]. The reference and sample were prepared optically dense (optical density near 2) at the excitation wavelength 525 nm, and greater than 2 at 582 nm for the J-aggregate solution. Front-face illumination (with an incident angle of ca. 22.5° relative to the normal) was used. In our measurements we used a 1 cm cell, with "complete" absorption occurring within 1 or 2 mm near the front surface of the cell. The contributions to the total absorption due to the cis- and trans-aggregates were determined by decomposing the absorption spectrum (such as that shown in Part B of Figure 2) when both species are present. For quantum yield as well as fluorescence lifetime measurements, solution conditions which gave rise to two aggregate bands were chosen. The corrections required for wavelength response of the emission monochromator-photomultiplier combination were made with correction factors supplied by the vendor. The slit widths for the excitation and emission monochromators were set to 0.5 mm ($\approx$ 2 nm).

The SPEX Fluorolog-τ2 spectrofluorometer, which uses the phase-modulation technique, was used for the determination of fluorescence lifetimes. When configured for lifetime measurements, radiation from a cw xenon incandescent light source (or laser) is directed to a Pockels cell; in our experiments we used front-face illumination and radiation at 550 nm, with a bandpass of ca. 4 nm (resulting from a 1 mm entrance slit width of the excitation spectrometer). Approximately 8% of modulated excitation light from the Pockels cell is directed to the reference detector and the remainder to the sample. To measure the fluorescence lifetime of 2,2'-cyanine aggregates, a reference standard, glycogen, as well as the sample are required. The fluorescence lifetime determination is made through an analysis which utilizes the relative phase shift and relative demodulation of the sample compared to that of the reference.

III. Results and Discussion

A. Steady-State Spectroscopic Studies

Figure 2 shows absorption spectra of 2,2'-cyanine in the absence (Part A) and presence (Parts B and C) of vesicle solution, as well as the "quasi-resonance" fluorescence spectrum (Part D, also in the presence of vesicle solution), in which the fluorescence band nearly overlaps the absorption band. The absorption spectrum of 2,2'-cyanine in the absence of vesicle solution (Part A) consists of a vibronic progression with the band at ca. 524 nm corresponding to the 0←0 band (bandwidth 1100 cm^{-1}), the band at ca. 490 nm corresponding to the 1←0 band (bandwidth 1550 cm^{-1}), and the shoulder at ca. 454 nm corresponding to the 2←0 band (estimated bandwidth of 1800 cm^{-1}).

Addition of vesicle solution to the dye solution promotes aggregation of the dye, as indicated by a color change from orange to pink. Based upon experimental conditions, such as the concentrations of the dye and vesicle solutions, the solution pH, viscosity and temperature, and the surface potential of the vesicle, we obtain, in general, two different absorption spectra: one has two red-shifted bands (see Part B) located at ca. 572 and 582 nm and the other has only one red-shifted band (see Part C) located at ca. 582 nm. The experimental solution composition conditions which typically led to the occurrence of spectra containing one red-shifted band spectrum were dye concentration, 5×10^{-5} M ; vesicle concentration, 1.6×10^{-3} M; and a volume ratio of dye to vesicle of 2:1. Typical experimental conditions which led to the existence of two red-shifted

bands were dye concentration, 1×10^{-4} M; vesicle concentration, 2×10^{-5} M; and a volume ratio of dye to vesicle of 1:1. When the volume ratio of the latter dye/vesicle solution was varied the relative absorbances of the two red-shifted bands were changed, as well as that of the monomer (data not shown here). The two red-shifted bands, termed the J-bands, are attributed to adsorption by aggregated molecules consisting of mono-cis monomers (at 572 nm) and all-trans monomer (at 582 nm). This assignment is also supported by Raman spectra from this laboratory of J-aggregates adsorbed onto a vesicle surface [26].

It might be noted that the optical absorption spectrum of the J-aggregate of 2,2'-cyanine has been theoretically calculated using excitonic transitions, and the narrow bandwidth of the J-band was shown to result from motional narrowing [39]. Furthermore, two vibronic bands of the aggregate, for low temperature systems, have been found at 495 and 535 nm [40,41]. For the present study, we assume that the aggregate vibronic bands are of much lower intensity than those absorption bands due to the monomer, and, as a result, do not measurably alter relative absorbance determinations for aggregate and monomer.

Part D of Figure 2 shows the quasi-resonance fluorescence spectrum of the J-aggregate, with a band centered at 585 nm, when excited at 550 nm. The fluorescence maximum is shifted to the red by ca. 3 nm when compared to the absorption due to the J-band (see Parts C and D of Fig. 2). We have also studied the dependence of the position of the fluorescence intensity maximum on excitation wavelength (not shown), and found it invariant, leading to the conclusion that the fluorescence originates from the lower levels of the LUMO excited state—the lower band edge levels are presumably populated by nonradiative relaxations. It is to be noted that monomer dye molecules in water alone (concentration of ca. 10^{-5}, pH = 11) do not fluoresce [42].

Parts A and B, respectively, of Figure 3 show fluorescence excitation and synchronized emission spectra of the aggregate. For the fluorescence excitation spectrum the excitation range is from 400 to 600 nm with detection on the shoulder of the low energy side of the J-band at 605 nm (with a bandpass of 0.4 nm throughout the range). The excitation spectrum reveals bands at 572 and 585 nm, which are attributed to structurally different aggregates, namely, the cis- and trans-aggregates, respectively. In addition, weaker bands at ca. 450, 480, 520, and 540 nm are present, and presumably are due to vibronic transitions of the aggregates. The synchronized emission spectrum of the aggregate, with 3 nm

offset between the excitation and emission spectrometers (of the SPEX Fluorolog) throughout the range from 400 to 650 nm, reveals bands at ca. 575 and 585 nm. Again, these two bands are assigned to the putative cis- and trans-aggregates, respectively. We find that the relative intensity of these latter bands differs from that found in the fluorescence excitation spectrum. In the fluorescence excitation spectrum the 572-nm band is more intense than the 585-nm band, while in the synchronized emission spectrum the 575-nm band is less intense than the 585-nm band. We presume that this variation in relative intensities for the two J-bands signals energy transfer from the higher energy cis-aggregate to the lower energy trans-aggregate. The higher ratio of the 572-nm band to the 585-nm band in the fluorescence excitation spectrum occurs because during the lifetime of the emission energy moves from the cis- to the trans-aggregate and contributes to intensity at the detection wavelength of 605 nm. The cis-aggregate, thus, is deduced to have a greater relative concentration in the ground state than does the trans-aggregate. The fact that the synchronized emission spectrum reveals an inverse relationship between the relative intensity of the bands is interpreted as indicating a greater relative concentration of the trans- to the cis-aggregate in the excited state: a determination arrived at since an offset of 3 nm means that the intensity will track the concentration of the particular aggregate, and possibly will have only a minimal contribution from the wing or shoulder of a nearby emission band. The deduction concerning relative populations of the two ground and excited states of the aggregate is the same reached by De Boer et al. [41] from a contrasting of fluorescence excitation and extinction measurements.

B. Fluorescence Dynamics

Early measurements of the fluorescence lifetime of J-aggregates formed in solution or on glass gave very short lifetimes [43-47], on the order of picoseconds, since the high excitation intensities used resulted in exciton annihilation.

Sundström et al. [48] performed experiments on J-aggregates of 2,2'-cyanine in homogeneous aqueous solution at room temperature and determined that both the lifetime and the fluorescence yield were strongly dependent on excitation pulse intensity; a single exponential lifetime of about 400 ps was measured at low excitation intensity. Other time-dependent studies that avoided the excitation pulse intensity problem were conducted by Wiersma et al. [11,12,41,49,50] who utilized J-aggregates of 2,2'-cyanine formed in an ethylene

glycol/water glass at low temperature, and ascertained that the low-temperature fluorescence lifetime was 70 psec. In these latter studies, the measured lifetime was found to be independent of temperature up to 50 K, and temperature dependent (increasing with temperature) above 50 K; they further concluded that molecular superradiance (due to disordered molecular aggregates) is the dominant deactivation process.

Other recent investigations provide information on fluorescence dynamics for 2,2'-cyanine. For example, Muenter et al. [13] reported the dependence of fluorescence lifetime and relative quantum yield on temperature and aggregate size for the J-aggregates of 2,2'-cyanine on AgBr surface, and showed that the dominant process controlling the dynamics was energy transfer to a defect state—a dimer structure was suggested. This nonradiative process was postulated to lead at room temperature to a strong diminution in fluorescence yield with increasing concentration.

Dorn and Müller [51] measured a lifetime of 8.2 ps for a Langmuir-Blodgett monolayer of 2,2'-cyanine J-aggregate at room temperature, and a value of 5.5 ps at 143 K; they interpreted the decrease in lifetime as evidence for superradiance enhancement.

Additionally, Fidder et al. [12] have shown for a Langmuir-Blodgett monolayer of 2,2'-cyanine J-aggregate at 1.5 K that the fluorescence lifetime of the initial decay process was 10 ps— a slower, secondary decay was not evaluated. These latter authors attributed the nonexponentiality of the decay to a combination of exciton transport and radiative decay. The structure of J-aggregates in a Langmuir-Blodgett monolayer was deduced to be quasi two-dimensional and more delocalized than one dimensional aggregates formed in frozen glass.

In this laboratory we used the phase-modulation method to determine fluorescence lifetimes. In this method [52], the sample is excited with light whose intensity is sinusoidally modulated. Since there is a time lag between absorption and emission, emission is delayed in phase and demodulated relative to the incident light. The phase delay (ϕ) and demodulation factor (m) can be experimentally measured and used to determine the fluorescence lifetime of the aggregate. The phase and modulation apparent lifetimes, τ_p and τ_m, respectively, are defined as

$$\tau_p = \omega^{-1} \tan \phi \quad (1)$$

$$\tau_m = \omega^{-1} \left(\frac{1}{m^2 - 1} \right)^{1/2} \quad (2)$$

where ω is the modulation frequency.

Analysis and nonlinear least-squares fitting (Marquardt-Levenson minimization algorithm) were performed with software provided by Globals Unlimited (Urbana, IL). Phase-shift and demodulation measurements were obtained for modulation frequency ranging from 20 to 250 MHz.

Frequency domain fluorescence intensity decay of the putative trans- and cis-aggregates of 2,2'-cyanine adsorbed onto a vesicle surface at room temperature is shown in Figure 4. The excitation wavelength was 550 nm and the phase shifts for the fluorescence intensities for the cis- and trans-aggregates were measured separately by setting the emission monochromator at appropriate detection wavelengths, 575 and 585 nm, respectively. Both measurements fit single exponential decay models with low χ^2 values: the fluorescence lifetime of the cis-aggregate was found to be 110 ± 20 ps, with a $\chi^2 = 1.06$; the trans-aggregate's fluorescence lifetime was found to be 340 ± 20 ps, with $\chi^2 = 0.87$.

The fluorescence quantum yield measurements were carried out under the conditions mentioned in the experimental section. Fluorescence quantum yields were determined by using the relationship [54],

$$Q_J = Q_S \frac{A_J}{A_S} \frac{(1 - 10^{-OD_S})}{(1 - 10^{-OD_J})} \frac{n_J^2}{n_S^2} \quad (3)$$

where, for our system, J and s specify the J-aggregate and the standard, respectively; A is the integrated area under the corrected fluorescence spectrum; n is the refractive index of the solution; and OD is the optical density at excitation wavelengths used: 525, 560, and 570 nm.

Fluorescence quantum yields were found to be 0.28 ± 0.03 for the trans-, and 0.04 ± 0.01 for the cis-aggregate, respectively—with the possible error in the determination reflecting the range in the respective measurement when several different excitation wavelengths, between 560 and 570 nm, were used. (Note that for the cis-isomer, the synchronized emission spectrum was used.)

Fluorescence lifetime and quantum yield are related to the radiative rate constant k_r and nonradiative rate constant k_{nr} by the photophysical equations:

$$k_r = \frac{\phi_f}{\tau_f} \tag{4}$$

$$k_{nr} = \frac{1-\phi_f}{\tau_f} \tag{5}$$

Upon substituting the measured values of fluorescence lifetimes and quantum yields, one finds that for the trans-aggregate $k_r = (8.3 \pm 0.2) \times 10^8\ s^{-1}$ and $k_{nr} = (2.1 \pm 0.2) \times 10^9\ s^{-1}$. We deduce, in this case, that the nonradiative process is exciton transport (electronic energy transfer): each exciton created travels within the aggregate before being captured by a local potential minimum (luminescent center), suggesting the concept of coherence size, i.e., the length (or area) of the molecules strongly coupled to each other and responding in phase to the external optical field. The radiative rate suggests some alignment of molecules in a single aggregate, thus supporting the concept of a coherence dimension. The implicit disorder might be attributed to variations in orientation of the remaining molecules in an aggregate. A consequence of this assumption, as suggested by others [15,16], is that the physical size of a single aggregate would differ from the coherent size. The coherence size, in fact, has been deduced to be equal to the ratio of the J-aggregate's and monomer's radiative rate constants. This ratio is found to be 3 for the trans-aggregate, with the monomer radiative rate constant calculated by the data taken from Ref. 42. We interpret our results as indicating superradiant emission of the trans-aggregate adsorbed onto a vesicle surface at room temperature.

The radiative and nonradiative decay rates for the cis-aggregate are calculated to be $(3.6 \pm 0.9) \times 10^8\ s^{-1}$ and $(2.4 \pm 0.9) \times 10^9\ s^{-1}$, respectively. In this case, the nonradiative processes would be exciton transport: energy transfer, for example, to the trans-aggregate or a defect state. The strong overlap of the absorption spectrum of the cis-aggregate and the emission spectrum of the trans-aggregate, about 40% of the normalized spectra (not shown here), suggests a large cross-section for energy transfer. Energy transfer, indeed, is likely to emanate from an electromagnetic coupling between the cis-aggregate (energy donor) and the trans-aggregate (energy acceptor) [53, 54], both aggregates being coupled to the lattice, and weakly coupled to each other. We estimate that the

energy transfer rate is of the same order of magnitude as the fluorescence lifetime, that is ≈ 100 ps. Thus, the ratio of the nonradiative to radiative decay rate for the cis-aggregate (about 24) indicates that nonradiative processes are of principal importance in determining excited-state dynamics. It is also to be noted that the ratio of the radiative rate constants for the cis-aggregate to that of the monomer is calculated to be 1, indicating weaker or no superradiance. Hence, upon comparison of this result with that of the trans-aggregate, we observe that superradiance is greater for the lower energy aggregate configuration.

A schematic representation of energy levels and related photophysical processes is shown in Figure 5. The photophysical properties of the J-aggregates adsorbed on a vesicle surface and those for the monomer are tabulated in Table I.

It is to be noted that Mukamel et al. [14-16] have provided a theoretical relationship connecting superradiance, exciton-phonon coupling, coherence size, etc. The coherence size is found to depend on the coupling strength, the phonon bandwidth, the aggregate temperature, and the aggregate's physical size, for small aggregates whose size is much smaller than the optical wavelength. Our results indicate that the exciton-phonon coupling strength for the cis-aggregate (compared to that of the trans-aggregate) should be larger due to its smaller coherence size. This latter finding has been theoretically suggested by Spano et al. [16], and confirms the suggestion by Muenter et al. [13] that microscopic structure is related to superradiance.

In the case of J-aggregates formed in solution at low temperature [11,12], more intense superradiance is observed, with ca. 100 molecules apparently coupled, while J-aggregates on a AgBr surface at room temperature [13] shows weaker superradiance with ca. 2 molecules responding in phase to the external optical field. For our system, though two structurally different J-aggregates are formed on the vesicle surface, the trans-aggregate exhibits greater superradiance and more coupled molecules than reported for the AgBr system, but less superradiance than found for the frozen glass system.

It might be noted that the dynamics parameters which we have measured correlate with other studies reported from this laboratory in which a silver electrode was used as the substrate. We have suggested that the measured widths of the Raman excitation profiles of the two low frequency Raman exciton-

phonon modes located at 232 and 278 cm^{-1} (with room temperature peak intensities occurring at 575.5 and 577.5 nm, respectively) can be rationalized in terms of the relative energies of two aggregates [24]: the halfwidths of the excitation profiles of the trans- and cis-aggregate were found to be 434 ± 25 and 321 ± 20 cm^{-1} for the 232- and 278-cm^{-1} bands, respectively, with the widths reflecting the strengths of the dipole-dipole coupling in the excitonic state (i.e., the trans-aggregate has a larger dipole-dipole interaction energy, hence a larger spacing between sublevels, resulting in a wider excitation profile). In addition, the relative widths of the 232- and 278-cm^{-1} exciton-phonon Raman bands were rationalized using dephasing rate arguments: the dephasing of the higher energy 278-cm^{-1} band (assigned to the cis-aggregate) is faster since the spacing between sublevels is less, and dephasing depopulates the k=1 state from which transitions are allowed, leading to a narrower profile for the cis-aggregate. These earlier findings, indeed, are consistent with the cis-aggregate having a smaller coherence size, lower superradiance, and a shorter fluorescence lifetime than the trans-aggregate.

IV. Conclusions

Cyanine dye molecules have been shown to aggregate when adsorbed onto a phospholipid vesicle surface. Absorption, fluorescence and dynamics measurements for such a system are potentially useful as reference information for cyanines adsorbed onto metallic and semiconductor surfaces. Moreover, the phospholipid system might be a model system for investigating electron transfer dynamics and structure for chromophores intercalated into lipids.

Fluorescence excitation and synchronized emission and absorption spectra reveal the presence of two J-bands, which we attribute to a cis- and trans-aggregate species, relating to their being composed of mono-cis and all-trans stereoisomers, respectively. Energy transfer from the cis- to the trans-aggregate is used to rationalize the relative intensity difference found in the two types of emission studies.

Phase modulation picosecond fluorescence decay measurements reveal that superradiance and energy transfer between two aggregate structures are dominant features controlling photophysical processes. Superradiance is stronger for the trans-aggregate, corresponding to the lower energy configuration.

Acknowledgments

Support for this research by the National Science Foundation (NSF) under grant HRD-9353488 is gratefully acknowledged. One of us (SO) thanks the Scientific and Technical Research Council of Turkey (TUBITAK) for the award of a graduate scholarship.

REFERENCES

1. Feher, G.; Okumura, M. Y. In "The Photosynthetic Bacteria"; Clayton, K.; Sistrom, W.F., Ed.; Plenum: New York, **1978**.

2. Gilman, P. B. Photo. Sci. Eng. **1974**, 18, 418.

3. Borsenberger, P. M.; Chowdry, A.; Hoesterey, D. C.; W. Mey J. Appl. Phys. **1978**, 44, 5555.

4. Hanamura, E. Phys. Rev. B. **1988**, 37, 1273.

5. Sasaki, F.; Kobayashi, S. Appl. Phys. Lett. 1993, 63, 2887.

6. Wang, Y. Chem. Phys. Lett. **1986**, 126, 209.

7. Wang, Y. J. Opt. Soc. Am. B. **1991**, 8, 981.

8. Kobayashi, S. Mol. Crys. Liq. Crys. **1992**, 217, 77.

9. Jelley, E. Nature, **1936**, 138, 1009.

10. Scheibe, G. Angew. Chem. **1936**, 49, 563.

11. Fidder, H.; Knoster, J.; Wiersma, D. A. Chem. Phys. Lett. **1990**, 171, 529.

12. Fidder, H.; Terpstra, J.; Wiersma, D. A. J. Chem. Phys. **1991**, 94, 6895.

13. Muenter, A. A.; Brumbaugh, D. V.; Apolito, J.; Horn, L. A.; Spano, F. C.; Mukamel, S. J. Phys. Chem. **1992**, 96, 2783.

14. Grad, J.; Hernandez, G; Mukamel, S. Phys. Rev. A. **1988**, 37, 3835.

15. Spano, F. C.; Mukamel, S. J. Phys. Chem. **1989**, 91, 683.

16. Spano, F. C.; Kuklinski, J. R.; Mukamel, S. J. Phys. Chem. **1991**, 94, 7534.

17. Akins, D. L. J. Phys. Chem. **1986**, 90, 1530.

18. Akins, D. L.; Lombardi, J. R. Chem. Phys. Lett. **1987**, 136, 495.

19. Akins, D. L.; Akpabli, C. K.; Li, X. J. Phys. Chem. **1989**, 93, 1977.

20. Akins, D. L.; Macklin, J. W. J. Phys. Chem. **1989**, 93, 5999.

21. Akins, D. L.; Macklin, J. W.; Parker, L. A.; Zhu, H. -R. Chem. Phys. Lett. **1990**, 169, 564.

22. Akins, D. L.; Macklin, J. W.; Zhu, H. -R. J. Phys. Chem. **1991**, 95, 793.

23. Akins, D. L.; Zhu, H. -R. Langmuir **1992**, 8, 546.

24. Akins, D. L.; Zhuang, Y. H.; Zhu, H. -R.; Liu, J. Q. J. Phys. Chem. **1994**, 98, 1068.

25. Sato, T.; Yonezewa, Y., Hada, H. J. Phys. Chem. **1989**, 93, 14.

26. Akins, D. L., Ozcelik, S.; Liu, J. Q. Pittsburgh Conference, **1994**, Abstract # 936.

27. Ozcelik, S.; Akins, D. L. "Photophysics of Cyanine Dyes: I. Steady-State Spectroscopy and Fluorescence Lifetime of Monomeric Benzimidazolocarbocyanine," submitted to J. Phys. Chem., **1995**.

28. West, W.; Pearch, S. J. Phys. Chem. **1965**, 69, 1894.

29. O'Brien, D. F.; Kelly, T. M.; Costa, L. F. Photo. Sci. Eng. **1974**, 18, 76.

30. Knudtson, J. T.; Eyring, E. M. J. Phys. Chem. **1974**, 78, 2355.

31. Tredwell, C. J.; Keary, C. M. Chem. Phys. **1979**, 43, 307.

32. Sundström, V.; Gillbro, T. J. Chem. Phys. **1985**, 83, 2733.

33. Murphy, S.; Sauerwein, B.; Drickamer, H. G.; Schuster, G. B. J. Phys. Chem. **1994**, 98, 13476.

34. Aramendia, P. F.; Negri, R. M.; San Romàn, E. J. Phys. Chem. **1994**, 98, 3165.

35. Awad, M. M.; McCarthy, P. K.; Blanchard, G. J. J. Phys. Chem. **1994**, 98, 1454.

36. Åkesson, E.; Sundström, V.; Gillbro, T. Chem. Phys. **1986**, 106, 269.

37. Measurement made at General Food of Fort Lee, NJ by Dr. Stephen Habif.

38. Schafer, F. P. In "Dye Lasers." Springer-Verlag: New York, **1989**.

39. Knapp, E. W. Chem. Phys. **1984**, 85, 73.

40. Misawa, K.; Ono, H.; Minoshima, K.; Kobayashi, T. J. Lumin. **1994**, 60&61, 812.

41. De Boer, S.; Vink, K. J., Wiersma, D. A. Chem. Phys. Lett. **1987**, 137, 99.

42. Dorn, H-. P.; Muller, A. Chem. Phys. Lett. **1986**, 130, 426..

43. Yu, Z. X.; Lu, P. Y.; Alfano, R. R. Chem. Phys. Lett. **1983**, 79, 289.

44. Kopainsky, B.; Kaiser, W. Chem. Phys. Lett. **1982**, 88, 357.

45. Rentsch, S. K.; Danielius, R. V.; Gadonas, R. A.; Piskarkas, A. Chem. Phys. Lett. **1981**, 84, 446.

46. Brumbaugh, D. V.; Muenter, A. A.; Knox, W.; Mourau, G.; Wittmershaus, B.; J. Lumin. **1984**, 31&32, 783.

47. Fink, F.; Klose, E.; Teuchner, K.; Dahne, S. Chem. Phys. Lett. **1977**, 45, 548.

48. Sundström, V.; Gillbro, T.; Gadonas, R. A.; Piskarkas, A. J. Chem. Phys. **1988**, 89, 2754.

49. De Boer, S.; Wiersma, D. A. Chem. Phys. **1989**, 131, 135.

50. De Boer, S.; Wiersma, D. A. Chem. Phys. Lett. **1990**, 165, 45.

51. Dorn, H-. P.; Muller, A. Appl. Phys. B. **1987**, 43, 167.

52. Lakowicz, J. R. In "Principles of Fluorescence Spectroscopy." Plenum Press: New York, **1983**.

53. Di Bartolo, B.; In "Energy Transfer Processes in Condensed Matter", NATO-ASI Series B: Physcis, Vol. 114, Plenum Press, **1983**.

54. Agranovich, V. M.; Galanin, M. D. In "Electronic Excitation Energy Transfer in Condensed Matter." North-Holland Pub. Co., Amsterdam, **1982**.

Table I. Room temperature photophysical properties of 2,2'-cyanine J-aggregates (adsorbed onto a vesicle surface) as well as monomer in glycerol.

	Monomer	Cis-aggregate	Trans-aggregate
λ_{abs} (nm)	524[d]	572[b]	582[d]
λ_{em} (nm)	570[a]	575[c]	585[e]
$\Delta\nu_{abs}$ (cm^{-1})	1100[d]	1000[b]	300[b,d]
$\Delta\nu_{em}$ (cm^{-1})	2400[a]	325[c]	250[c] (400[e])
ϕ_f	0.03[a]	0.04 ± 0.01[c]	0.28 ± 0.03[e]
τ_f (ps)	94 ± 5[a]	110 ± 20	340 ± 20
τ_o (ps)	3700 ± 100[a]	2750 ± 700	1200 ± 200
k_r (s^{-1})	3×10^8	$(3.6 \pm 0.9) \times 10^8$	$(8.3 \pm 0.2) \times 10^8$
k_{nr} (s^{-1})	1×10^{10}	$(8.7 \pm 0.9) \times 10^9$	$(2.1 \pm 0.2) \times 10^9$
Coherence size (N_{eff})	—	—	3 ± 1

[a] Taken from Ref. 42; [b] Fluorescence excitation; [c] Synchronized luminescence; [d] Absorption; [e] Fluorescence.

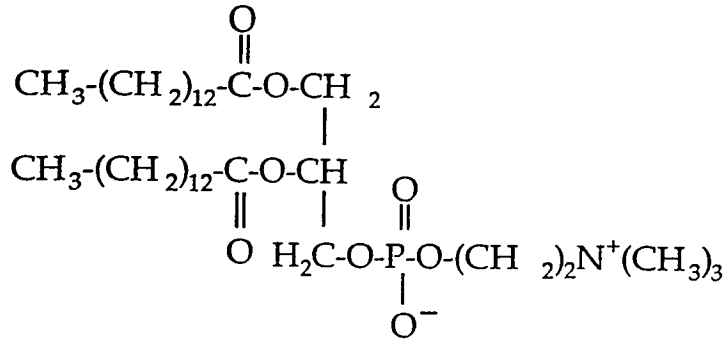

L-α-Dimyrisatoylphosphatidycholine (DMPC)

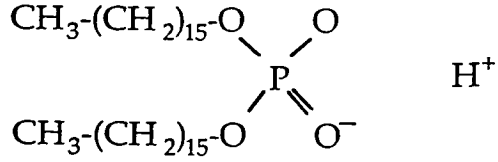

Diacetyl Phosphate (DCP)

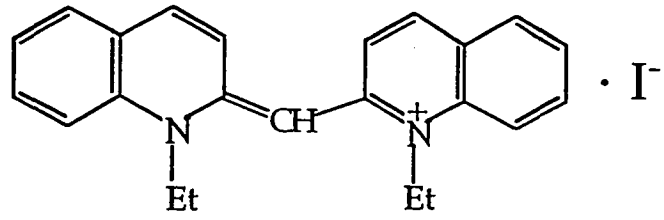

1,1'-Diethyl-2,2'-cyanine Iodide

Fig. 1: Chemical structures of 1,1'-diethyl-2,2'-cyanine and phospholipid surfactants.

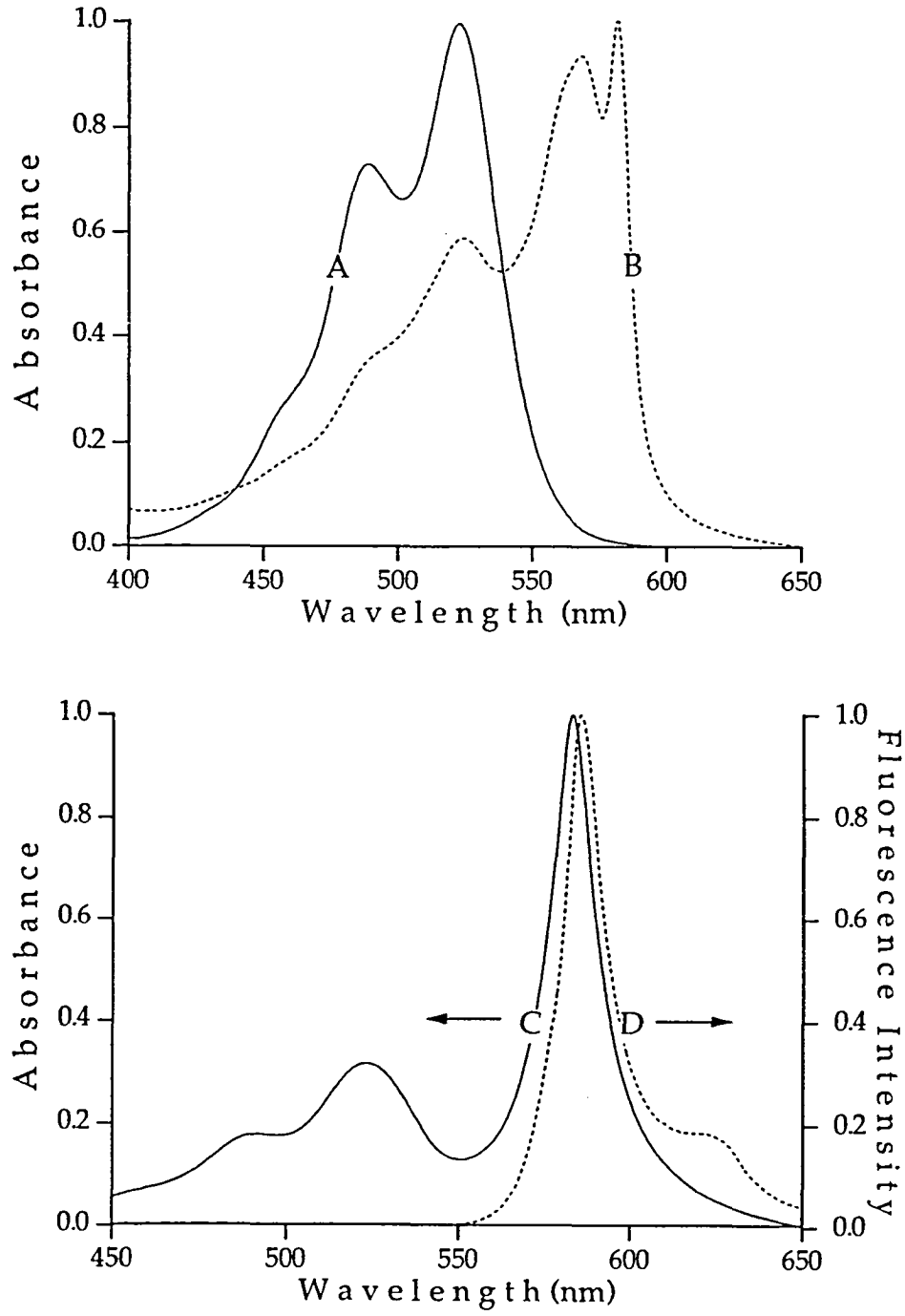

Fig. 2: (A) Absorption spectrum of 5×10^{-5} M 2,2'-cyanine in water alone (pH=10); (B) in the presence of vesicle solution (2×10^{-5} M, 1:1 molar mixture of DMPC and DCP, pH=3) showing two J-bands; (C) in the presence of vesicle solution (1.6×10^{-3} M, 1:1 molar mixture of DMPC and DCP, pH=3) showing one J-band; and (D) quasi-resonance fluorescence spectrum of the J-aggregates of 2,2'-cyanine in the presence of vesicle solution (dashed line). All spectra acquired are at room temperature and are normalized to their maximum intensity.

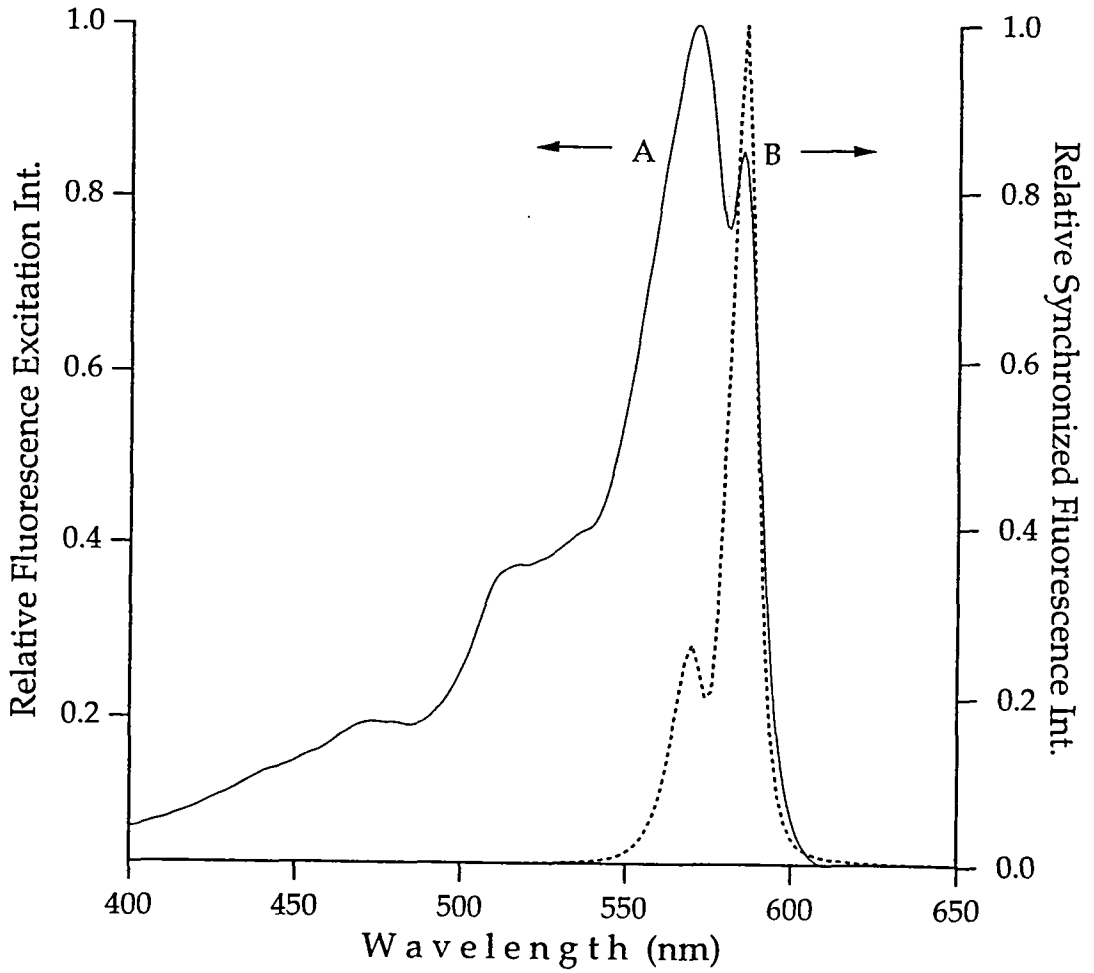

Fig. 3: Fluorescence excitation detected at 605 nm (A) and synchronized emission (B) spectra of the J-aggregates with a 3 nm offset between excitation and emission monochromators. Solution conditions same as in Part B of Fig. 2. Spectra are normalized to their maximum intensity.

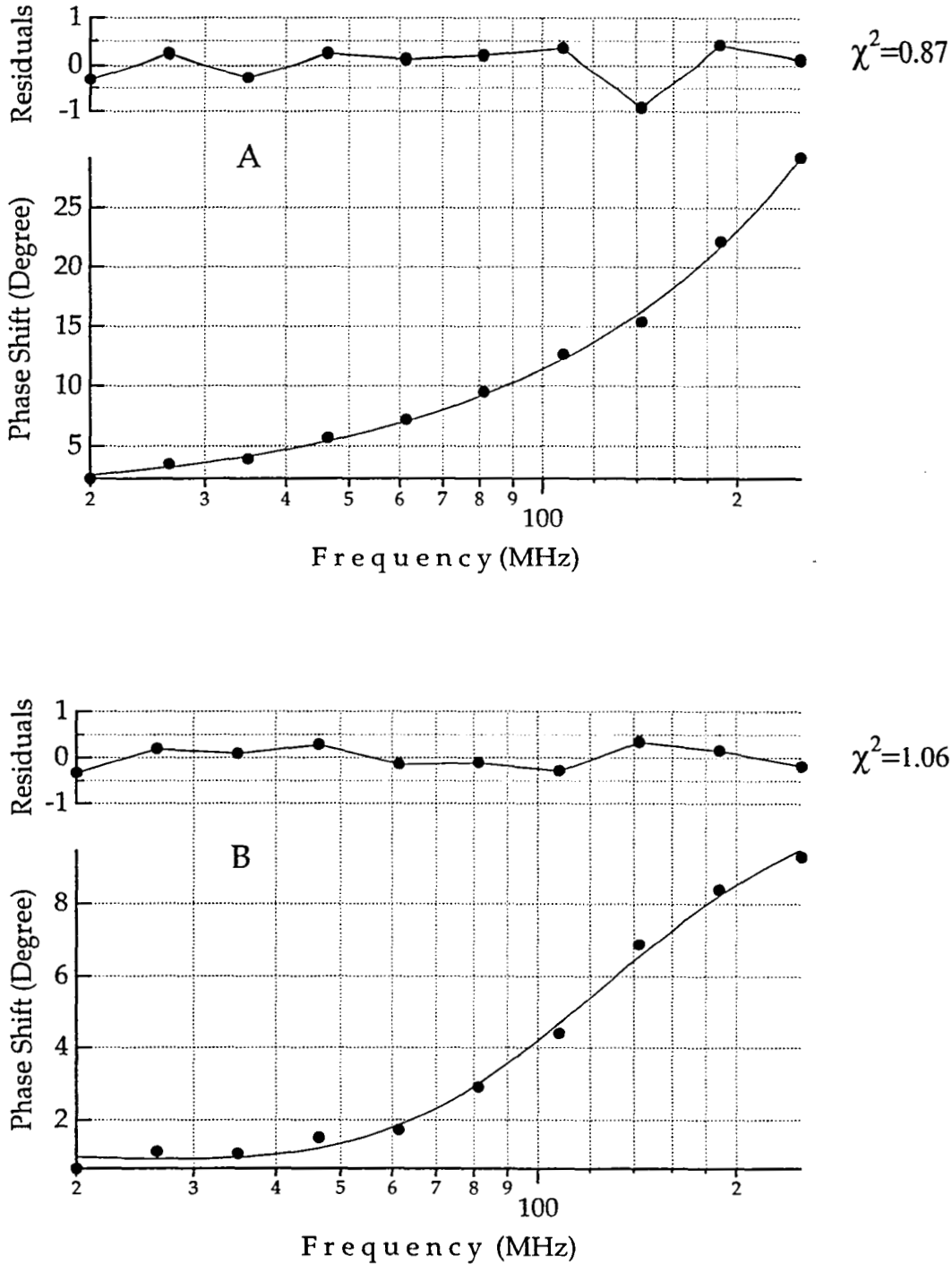

Fig. 4: Frequency domain fluorescence phase shift for (A) the trans-aggregate and (B) the cis-aggregates of 2,2'-cyanine adsorbed onto a vesicle surface at room temperature. Excitation wavelength was 550 nm, and the detection wavelengths were 575 and 585 nm for the cis- and trans-aggregates, respectively.

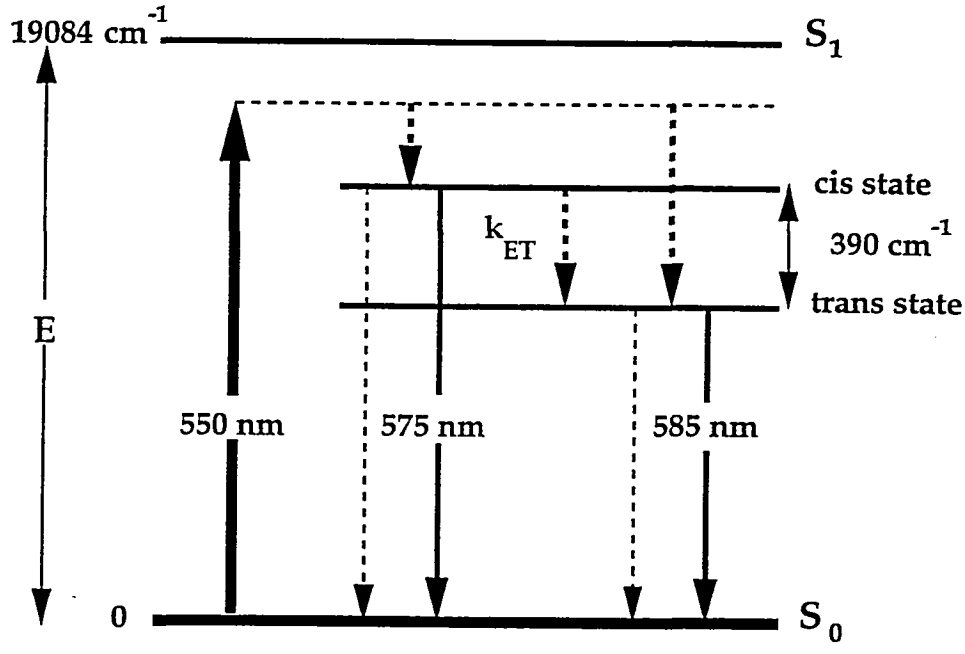

Fig. 5: Energy level diagram of photophysical processes for the J-aggregate. ET stands for an energy transfer from cis-aggregate to trans-aggregate.

SPECTROSCOPIC INVESTIGATION OF Ce^{3+} DOPED FLUORIDE CRYSTALS

Donald H. Reinhart, Jr.† and Guzin Armagan
Department of Physics, The College of William and Mary, Williamsburg, VA 23187

Waverly Marsh
Science Applications International Corporation
1 Enterprise Pkwy, Suite 250, Hampton, VA 23666

James Barnes
NASA Langley Research Center, MS 474, Hampton VA 23681

B. H. T. Chai
Center for Research and Education in Optics and Lasers,
University of Central Florida, Orlando, FL 32826

I. INTRODUCTION

Doping of the trivalent rare-earth cerium ion into fluoride crystals is of interest in producing tunable ultra-violet solid state lasers. These lasers are desirable for many applications in medicine, industry, and scientific research, including remote sensing. High absorption and stimulated emission cross sections of the dipole allowed 4f - 5d transitions show promise in cerium as a laser ion in crystals. Several research groups have already reported the observation of stimulated emission of cerium in $LiYF_4$ [1], $LiSrAlF_6$ [2], and $LiCaAlF_6$ [3,4]. However, the color center formation in the crystals due to the excited state absorption of ultra-violet pump light adds difficulty to achieving laser action [5,6]. We have investigated the spectroscopic properties of cerium such as absorption and emission spectra, and lifetimes in four different fluoride crystals, including $LiCaAlF_6$, $LiSrAlF_6$, KYF_4 and $LiYF_4$. We have derived the polarized absorption and stimulated emission cross sections from transmission and fluorescence emission measurements for each of the host crystals. We have measured the lifetime of the lowest 5d level; moreover, investigated the temperature dependence of this lifetime and the color center formation. Our results on absorption and stimulated emission cross sections for $LiCaAlF_6$ and $LiSrAlF_6$ are similar to the results already published [7].

---

†Bucknell University, Department of Physics, Lewisburg, PA 17837.

II. SAMPLES AND EXPERIMENTAL SETUP

The Center for Research and Education in Optics and Lasers, University of Central Florida, and the Lighting Optical Corporation provided the samples studied in this investigation. Table 1 reports several properties of these crystals. The transmission spectra were measured with a Cary 5 Spectrophotometer in the wavelength region from 250 to 400 nm. A pair of calcite polarizers was used to determine the σ- and π-polarized spectra. Fluorescence spectra were measured using a deuterium lamp as an excitation source. Cerium fluorescence was focused through a calcite polarizer to a monochromator that scanned a wavelength region of 250 to 400 nm. The fluorescence signal was detected using a GaAs photomultiplier tube. The measured spectrum for each sample was calibrated for the photomultiplier and grading sensitivities using a black body source.

Lifetime measurements were performed using a pulsed (pulse duration ~ 20 nsec) quadrupled Nd:YAG laser (wavelength = 266 nm) at a fluency of 7 mJ/cm^2 as the excitation source. Fluorescence decay curves were detected with a EMI-9817 photomultiplier tube. The fluorescence signal from the photomultiplier tube was recorded by a DSA 602 Tektronics digital oscilloscope. All measurements except lifetimes were conducted at room temperature. The changes in lifetimes with temperature were also investigated above room temperature.

III. ABSORPTION AND STIMULATED EMISSION CROSS SECTIONS

The measured polarized transmission spectrum allows us to determine the polarized absorption cross section as follows:

$$\sigma_{A\,p} = -\,(1/NL)\,\ln(I/I_0)_p \qquad (1)$$

where N is the concentration of cerium ions, L is the thickness of the material and (I/I_0) is the ratio of transmitted beam to reference beam intensity, and the index p denotes the σ or π polarizations. The Einstein relation [7,8]:

$$\sigma_{E\,p} = (\lambda^2 / 8\pi c n^2)\,(1/\tau_{rad})\,[\,I_p(\lambda) / \int [\,2I_\sigma(\lambda) + I_\pi(\lambda)\,]\,d\lambda/\lambda^2\,] \qquad (2)$$

leads us to derive the polarized stimulated emission cross section from the polarized emission spectrum. Here, τ_{rad} is the radiative lifetime and $I_p(\lambda)$ is the measured polarized emission spectrum.

The polarized absorption and emission cross section spectra of cerium derived using eqs. (1) and (2) for $LiCaAlF_6$, $LiSrAlF_6$, KYF_4 and $LiYF_4$ crystals appear in Fig.1. Table 2 summarizes the wavelength range of absorption and emission bands and Table 3 summarizes the peak values of the polarized stimulated emission cross sections.

Table 4 reports the lifetimes of the lowest 5d state of cerium in the fluoride host crystals. These lifetimes remained constant in the temperature range from 295 to 500 K. The quadrupled Nd:YAG laser at low fluency (~ 7mJ/cm^2) did not produce any visible color centers in the crystal. The color centers appeared and their density grew with increased laser fluency. However, the color center density considerably decreased with increasing temperature. An incident laser fluency of 0.6 J/cm^2 did not produce any visible color centers at temperature of ~500 K.

V. DISCUSSIONS

Several characteristics of the cerium doped crystals studied provide potential for their use as tunable solid state ultra-violet laser media. Each of the crystals has high absorption and stimulated emission cross section values with a significant difference between the two polarizations. The observation of σ-polarization to absorb more strongly than the π-polarization and π-polarization to emit more strongly than the σ-polarization evaluates the choice of pumping and lasing axis for a laser crystal. The "double-peak" appearance in the stimulated emission spectra for $LiCaAlF_6$, $LiSrAlF_6$, and $LiYF_4$ is due to the spin-orbit interaction splitting of the 4f level. However, KYF_4 is the only crystal that represents single peak.

$LiCaAlF_6$ and $LiSrAlF_6$ are exceptionally high, about $7x10^{-22}$ m^2 for absorption cross section and $1x10^{-21}$ m^2 for stimulated emission cross section. The absorption band for $LiCaAlF_6$ and $LiSrAlF_6$ also peaks near 266 nm, the quadrupled Nd:YAG laser wavelength commonly used as a pumping source. The disadvantages of these crystals lie in their short excited state lifetimes, 26–28 nsec, and in their doping process. Since the Ce^{3+} ion in $LiCaAlF_6$ and $LiSrAlF_6$ replaces the Ca and Sr atoms that are 2+, much of the attempted doping of Ce^{3+} does not remain in the crystal structure. Hence, doping concentrations for $LiCaAlF_6$ and $LiSrAlF_6$ are low.

KYF_4 shows promise in tuning abilities with a stimulated emission bandwidth of 105 nm, from 295 to 400 nm. A large stimulated emission bandwidth compromises its relatively low stimulated emission cross section. The KYF_4 and $LiYF_4$ absorption bands lie in the wavelength region suitable for flash lamp pumping. Their excited state lifetimes exceed that of both $LiCaAlF_6$ and $LiSrAlF_6$ with 38-40 nsec. Since the Ce^{3+} ion in KYF_4 and $LiYF_4$ replaces the Y^{3+}, the heavy doping concentration of these two crystals is easier to achieve.

Our observation on the temperature dependence of both color center density and lifetime offers a feasible solution in eliminating degradation in laser performance. Maintaining the fluoride crystal at a high temperature while lasing could quite possibly relieve the effect of this transient color center formation. Better understanding of these properties requires more investigation into the excited state absorption of cerium.

We wish to acknowledge the National Science Foundation for its REU Grant PHY-9300205 and the NASA Langley Research Center for its Grant NAS-19656 which supported the funding for this research.

REFERENCES

1. Ehrlich, D. J.; Moulton, P. F.; and Osgood, Jr., R. M.: Ultraviolet solid-state Ce:YLF laser at 325 nm. Opt. Lett., vol. 4, no. 6, 1979, pp. 184-186.

2. Pinto, J. F.; Rosenblatt, G. H.; Esterowitz, L.; and Quarles, G. J., "Continuously tunable UV Ce^{3+}:$LiSrAlF_6$ Laser", presented at IEEE Laser and Electro-Optics Society Annual Meeting, San Jose, California (Nov. 15-18, 1993).

3. M. A. Dubinskii, V. V. Semashko, A. K. Naumov, R. Y. Abdulsabirov, and S. L. Korableva: J. Mod. Opt. 40, 1 (1993).

4. M. A. Dubinskii, V. V. Semashko, A. K. Naumov, R. Y. Abdulsabirov, and S. L. Korableva, "Spectroscopy of New Active Medium of a Solid-State UV Laser with Broad band Single-Pass Gain", Laser Phys., Vol. 3, 216 (1993).

5. Ki-Soo Lim, and D. S. Hamilton, "Uv-induced loss mechanisms in a Ce^{3+}:$LiYF_4$ laser", J. of Lum. 40&41 (1988), 319-320.

6. Lim, Ki-Soo; and Hamilton, D. S.: Optical gain and loss studies in Ce^{3+}: $YLiF_4$. Opt. Soc. Am. B, vol. 6, no. 7, 1989, pp. 1401-1406.

7. C. D. Marshall, J. A. Speth, S. A. Payne, W. F. Krupke, G. J. Quarles, V. Castillo, and B. H. Chai, "Ultraviolet laser emission properties of Ce^{3+}-doped $LiSrAlF_6$ and $LiCaAlF_6$", J. Opt. Soc. Am. B, Vol. 11, No. 10, October 1994.

8. W. Koechner, "Solid State Laser Engineering", Springer-Verlag Berlin Heidelberg, 1988, p.15.

Table 1. Sample properties of cerium doped fluoride crystals used in this research.

Crystal	Doping (at %)	Site	Density (gr/cm^3)	Index of Ref. (n_o/n_e)	Length (mm)
$LiCaAlF_6$	0.005	Ca	2.983	1.3882/1.3852	8.28
$LiSrAlF_6$	0.01	Sr	3.45	1.3800/1.3840	8.01
KYF_4	0.1	Y	3.49	* / *	0.82
$LiYF_4$	0.2	Y	3.99	1.4535/1.4762	0.28

Table 2. Absorption and fluorescence emission bands of cerium in fluoride crystals.

Crystal	Absorption Range (nm)	Emission Range (nm)
$LiCaAlF_6$	240-290	270-350
$LiSrAlF_6$	240-300	270-350
KYF_4	240-310	295-400
$LiYF_4$	270-310	300-350

Table 3. Peak values of stimulated emission cross section of cerium in fluoride crystals.

Crystal	Polarization	Wavelength (nm)	Cross Section(m^2)
$LiCaAlF_6$	π-pol	290	10.3×10^{-22}
	σ-pol	286	8.0×10^{-22}
$LiSrAlF_6$	π-pol	292	10.0×10^{-22}
	σ-pol	287	6.8×10^{-22}
KYF_4	π-pol	310	6.0×10^{-22}
	σ-pol	310	4.1×10^{-22}
$LiYF_4$	π-pol	310	8.4×10^{-22}
	σ-pol	325	6.8×10^{-22}

Table 4. Lifetime of the lowest 5d state of cerium in fluoride crystals.

Crystal	Lifetime (nsec)
$LiCaAlF_6$ [7]	26
$LiSrAlF_6$ [7]	28
KYF_4	38
$LiYF_4$ [1]	40

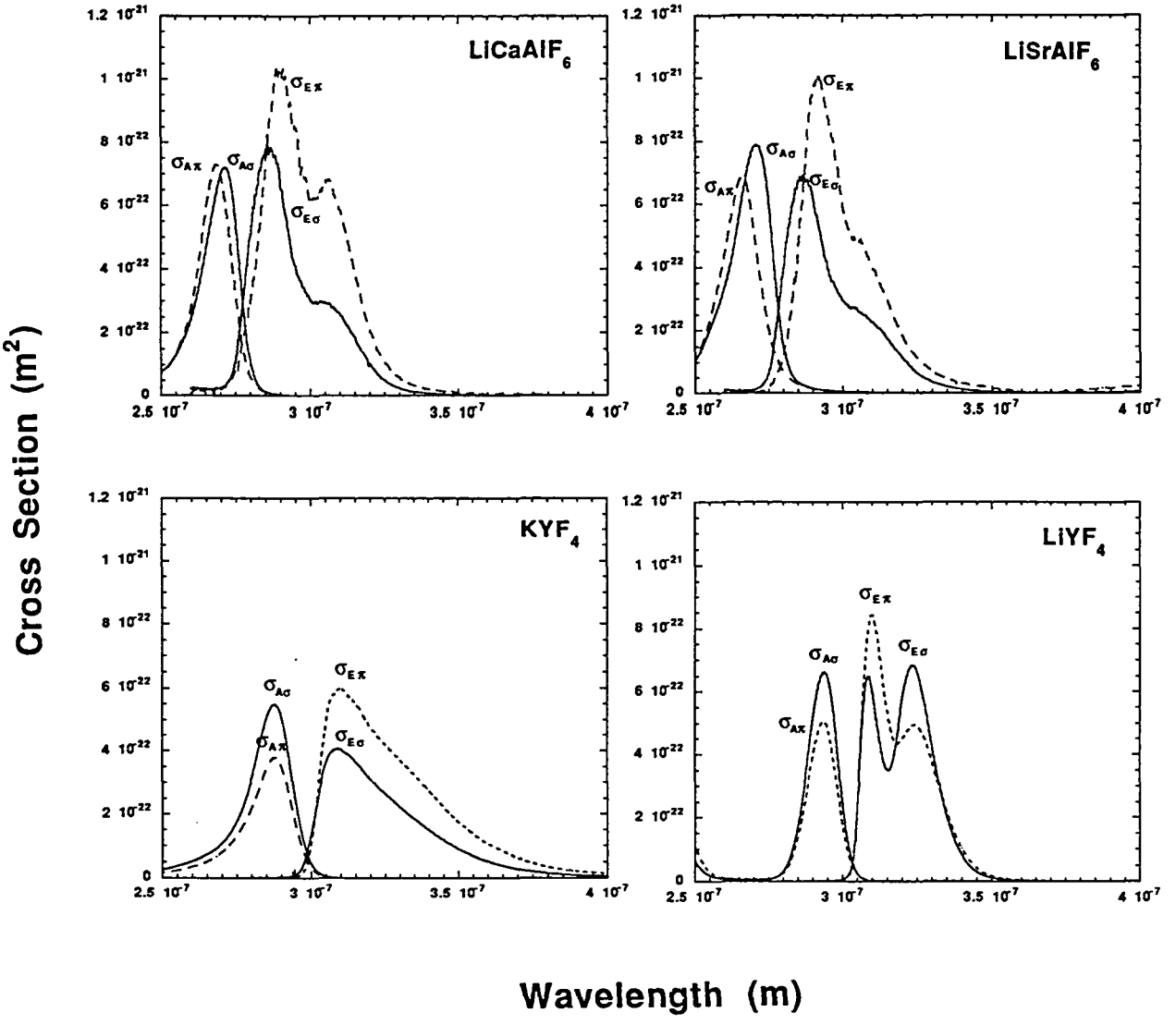

Fig.1. The polarized absorption and emission cross section spectra of cerium derived using eqs. (1) and (2) for $LiCaAlF_6$, $LiSrAlF_6$, KYF_4 and $LiYF_4$ crystals.

STUDY OF LUMINESCENCE CHARACTERISTICS OF TRIVALENT TERBIUM IN SILICATE GLASS

Mike S. West and Guzin Armagan
Department of Physics, The College of William and Mary
Williamsburg, VA 23187

William P. Winfree
NASA Langley Research Center, MS 231
Hampton, VA 23681

INTRODUCTION

An important use of silicate glasses doped with terbium oxide (Tb_2O_3) is their use as fiber optic sensors for high-resolution imaging applications requiring the detection of x-rays (e.g. tomography and radiography). The x-ray radiation is absorbed by the glass, producing electron-hole pairs (excitons). The excitons migrate through the glass matrix and then recombine, emitting characteristic Tb^{3+} luminescence in the optical wavelength region. This emission is due to forbidden transitions of 4f electrons and therefore has a long decay time. Long decay time is undesirable when imaging transient events since it results in blurring in time of the images.

It has been reported elsewhere [1,2] that in crystals Tb^{3+} ions can both act as luminescence centers and as fluorescence traps. These traps can capture excitons and delay their recombination. This delayed fluorescence is seen as a long lived, secondary component to the luminescence decay curve, or afterglow. Such a secondary decay component to the luminescence decay of Tb^{3+} has been observed before in soda glass following pulsed optical excitation[3]. In order to determine the conditions under which afterglow occurs, an understanding of the material's luminescent properties is required.

EXPERIMENT

Absorption, emission, and lifetime measurements were made on a terbium-doped fiber-optic array which is manufactured by Collimated Holes, Incorporated. The array is a silicate based glass which has a 5% doping of Tb_2O_3 by weight. The other major constituents of the glass (by weight percent) are oxides of silicon (56%), strontium(21%), and cesium(12%). The fiber-optic array originally had dimensions of 5.0 cm x 1.8 cm x 0.3 cm. From this, a sample was cut with dimensions (0.81 cm x 0.90 cm) more suitable for spectroscopic measurements. All surfaces of the sample were polished to reduce light scatter.

Absorption Spectra

The absorption spectrum of the glass was measured using a Perkin-Elmer Lamda-9 spectrophotometer. The spectrophotometer operates by splitting light from a source into two beams: one which acts as a reference beam and one which passes through the material. The intensities of the two beams are measured and compared to determine the absorbance of the glass:

$$A = -ln(\frac{I}{I_0})$$

where I is the intensity of light after leaving the sample, I_0 is the reference intensity, and A is the absorbance.

Emission Spectra

A diagram of the emission spectra setup is shown in Figure 1. A laser or lamp is used to pump the sample in the visible and UV wavelength regions. Radiation from the laser/lamp is absorbed and then re-emitted as light characteristic to the active ions in the sample. Emitted light is reflected into a collecting lens, through a beam chopper and into a monochromator. The light leaving the monochromator is picked up by a detector. The signal from the detector goes to a lock-in amplifier and then onto a computer where the signal is stored.

Lifetime

Figure 2 shows the experimental setup for the UV-excitation lifetime measurements. Laser light is focused down to a point onto the sample by two lenses. The beam is reflected 90 degrees to the sample in order to avoid having laser light entering the detector. Light emitted by the sample is collected by a third lens, directed to the detector. Two filters, a cut-off filter and an interference filter, are placed in front of the detector in order to isolate the characteristic emission from the sample. The signal from the detector goes through a pre-amp and into a digital oscilloscope. The data from the oscilloscope can then be downloaded to a computer.

The setup for the x-ray excitation lifetime measurements is diagramed in Figure 3. The sample is coupled to a photomultiplier tube and base. A cover is placed over the end of the tube in order to prevent light leaks. X-rays from a bremsstrahlung device are modulated by a tungsten shutter before striking the sample. The shutter modulation frequency is controlled by a function generator, which also triggers a digital oscilloscope. After averaging, the data is downloaded to a computer.

RESULTS AND DISCUSSION

Absorption and emission spectra

The visible and UV absorption spectrum of the glass sample is illustrated in Figure 4. The transitions from the ground state, $^7F_6$, to the excited states of Tb^{3+} are clearly discernible in the visible realm. Towards the ultraviolet end of the spectrum, however, the states of Tb^{3+} become mixed with band states of the glass. Deep UV absorption sets in the glass just above 300 nm, where it appears to be virtually opaque. Because of this, the transition from the 4f to the 5d shell (225 nm), which is allowed under Laporte selection rules, was not resolvable.

Figure 5 shows the emission spectra of the glass in the visible region. An argon-ion laser emitting at 477 nm was used to probe the strong visible transitions of Tb^{3+} from the $^5D_4$ state to the ^7F_J manifolds. As can be seen in Figure 4, the strongest emission is due to the $^5D_4$ - $^7F_5$ transition (550 nm). To probe transitions from the higher $^5D_3$ level to the ^7F_J levels, a broad spectrum deuterium lamp (200-700 nm) with emission lines in the ultraviolet was used. Comparing the spectrum of the $^5D_3$ transitions (Figure 6) to the $^5D_4$ transitions (Figure 5), it can be seen that emission due to transitions from the $^5D_3$ level is weaker by two orders of magnitude. Possible reasons for the quenching of the $^5D_3$ - ^7F_J transitions are non-radiative transitions from $^5D_3$ to $^5D_4$ [4] and cross-relaxation between neighboring Tb^{3+} ions (Figure 7).

Lifetime

A 10 nanosecond pulsed nitrogen laser emitting at 337 nm was used to excite the glass in the UV region. The primary component of the luminescence decay of the green emission line had a lifetime of approximately 3.5 milliseconds. The measured lifetime is in good agreement with lifetimes measured on other terbium doped glasses [5,6]. The green line of the $^5D_4$ - ^7F_J transition was isolated using a 512 nm cut-off and a 540 nm interference (band-pass) filter in order to cut down on background noise. Figure 8 shows evidence for a second, slower component to the decay which has a lifetime of approximately 1.0 second. This second component, however, is extremely weak, accounting for less than 1 percent of the overall output.

The x-ray excitation setup was designed to measure afterglow by exposing the glass to x-rays and then cutting off the source for a period of time much longer than the expected characteristic lifetime of Tb^{3+}. The duration of the exposure was purposely made long (2.5 seconds) in order to promote energy migration by creating excitons in the glass. The data from this measurement showed a single component with a lifetime of 2.85 milliseconds (Figure 9). Note that the non-linear portion of the plot is due to the closing of the shutter. This value is fairly consistent with the before mentioned measurement using the nitrogen laser. No long lifetime components were observed, however. This may be due to the fact that these long lifetime components are very weak and fell below the noise level of the detector.

CONCLUSIONS

Luminescence decay measurements under UV and x-ray excitation conditions demonstrate essentially the same characteristics in that the primary mode of decay has a lifetime of approximately 3 milliseconds. The longer decay component, which was evident only in the near-UV excitation lifetime measurement, appears to be too weak to be noticeable in x-ray detector applications. The relatively slow response of the glass is tolerable in such applications provided the scan period does not approach that of the luminescence lifetime.

ACKNOWLEDGEMENTS

This research was supported by NASA grant NAG-1-1597.

The authors would like to thank Ray Parker*, John Grainger*, and Randy Worjec** for all the assistance and advice they provided on this project.

REFERENCES

[1] M.F. Joubert, B. Jacquier, R. Mongorgé, and G. Boulon, J. Physique 43 (1982) 893.
[2] F. Kellendonk and G. Blasse, J. Phys. Chem. Solids, Vol. 43, No. 5 (1982) 481.
[3] B.V. Shulgin, K.N.R. Taylor, A. Hoaksey, and R.P. Hunt, J. Phys. C. 5 (1972) 1716.
[4] A. Hoaksey, J. Woods and K.N.R. Taylor, Journal of Luminescence 17 (1978) 385.
[5] R. Ruchti et al, IEEE Transactions on Nuclear Science, Vol. NS-31, No. 1 (1984) 69.
[6] Hua Shao, Don W. Miller, and Robert Pearsall, IEEE Transactions on Nuclear Science, Vol. 38, No. 2 (1991) 845.

* NASA Langley Research Center
** CEBAF

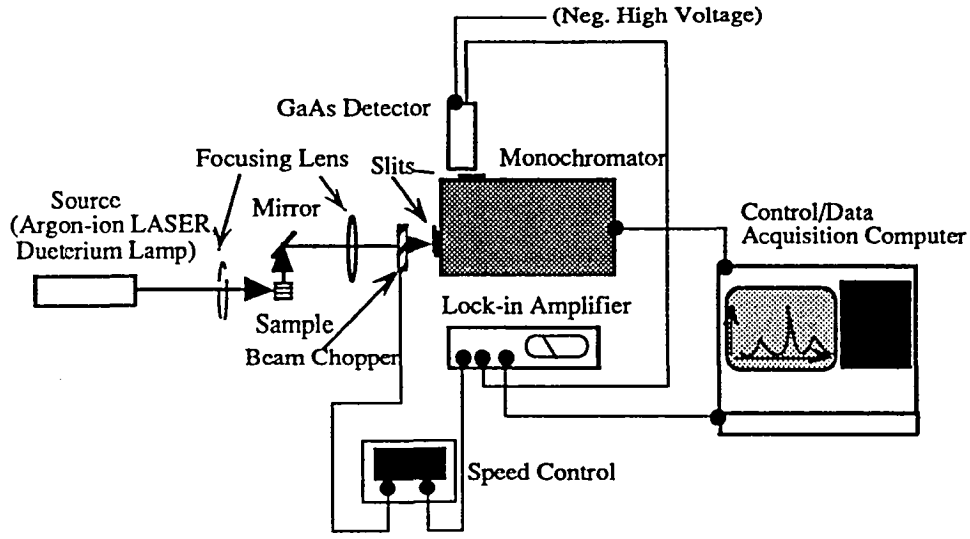

Figure 1. Emission Spectra Setup

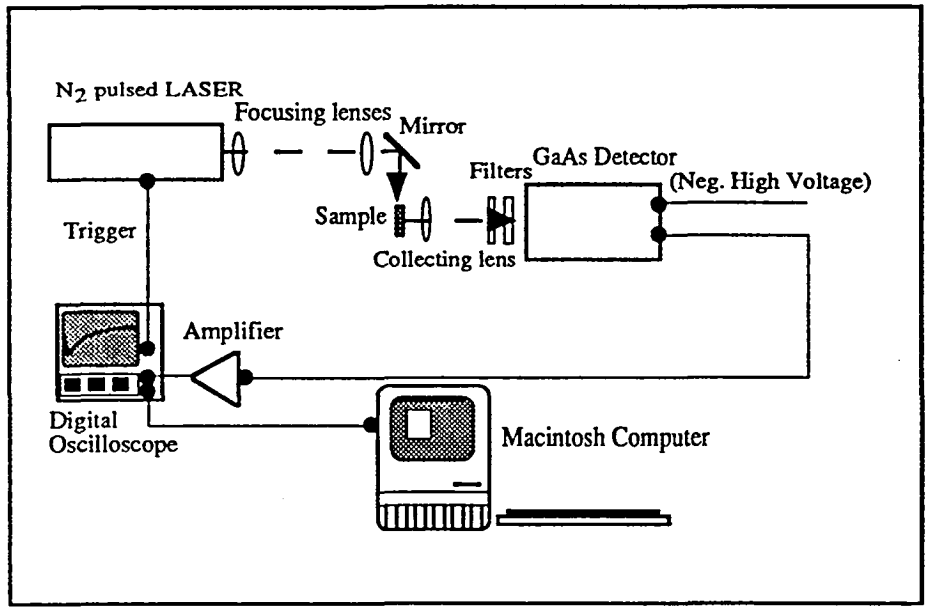

Figure 2. Nitrogen Laser Excitation Lifetime Setup

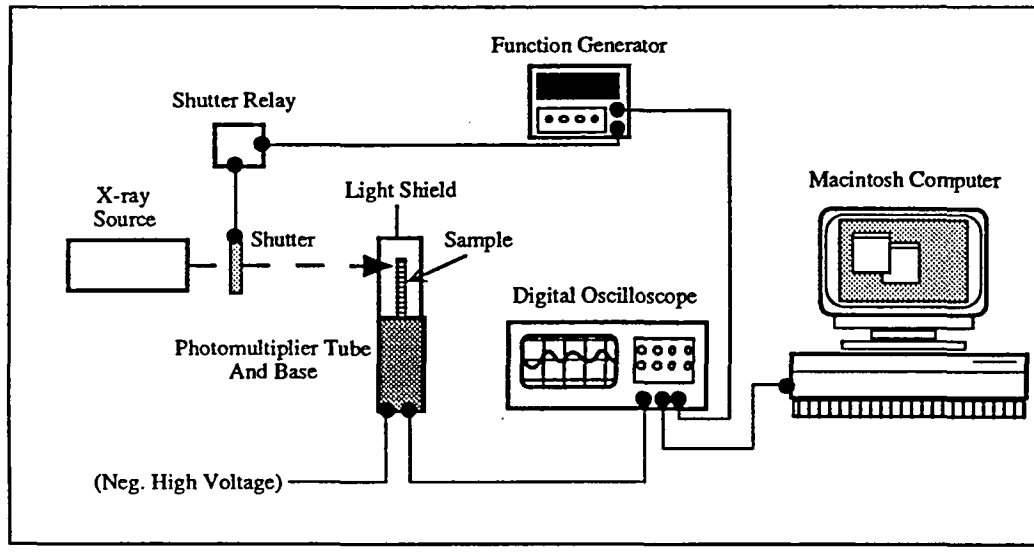

Figure 3. X-ray Excitation Lifetime Setup

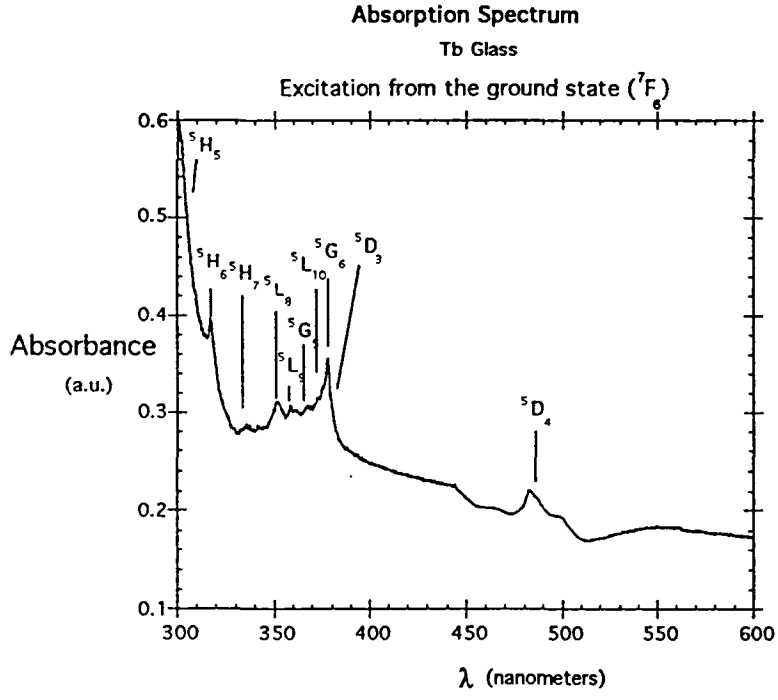

Figure 4. Excitation From The $^7F_6$ Level

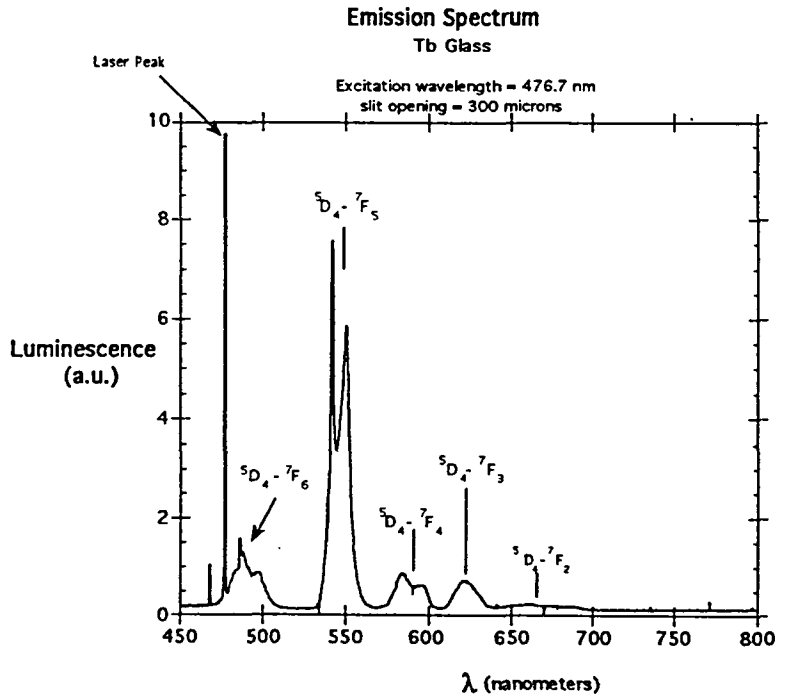

Figure 5. $^5D_4$ Transitions

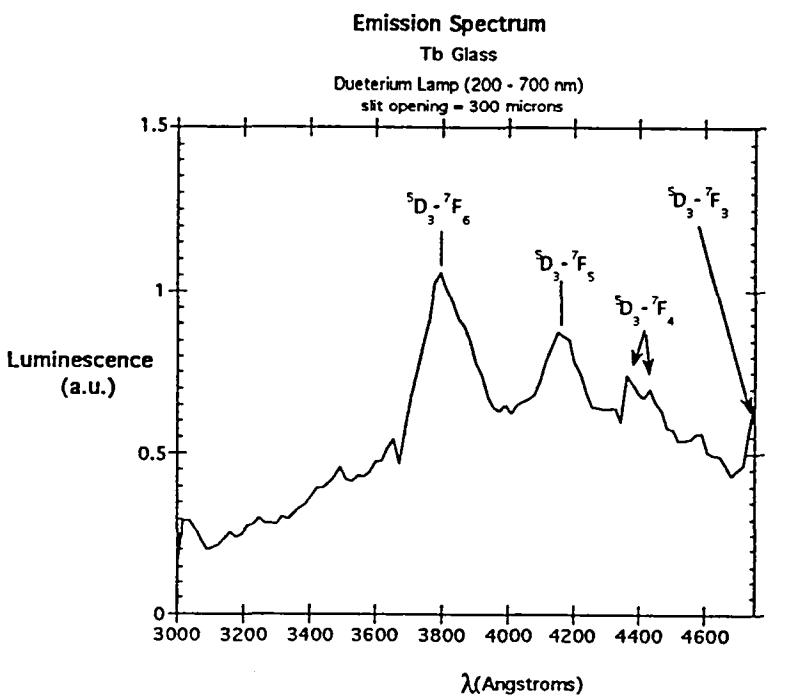

Figure 6. $^5D_3$ Transitions

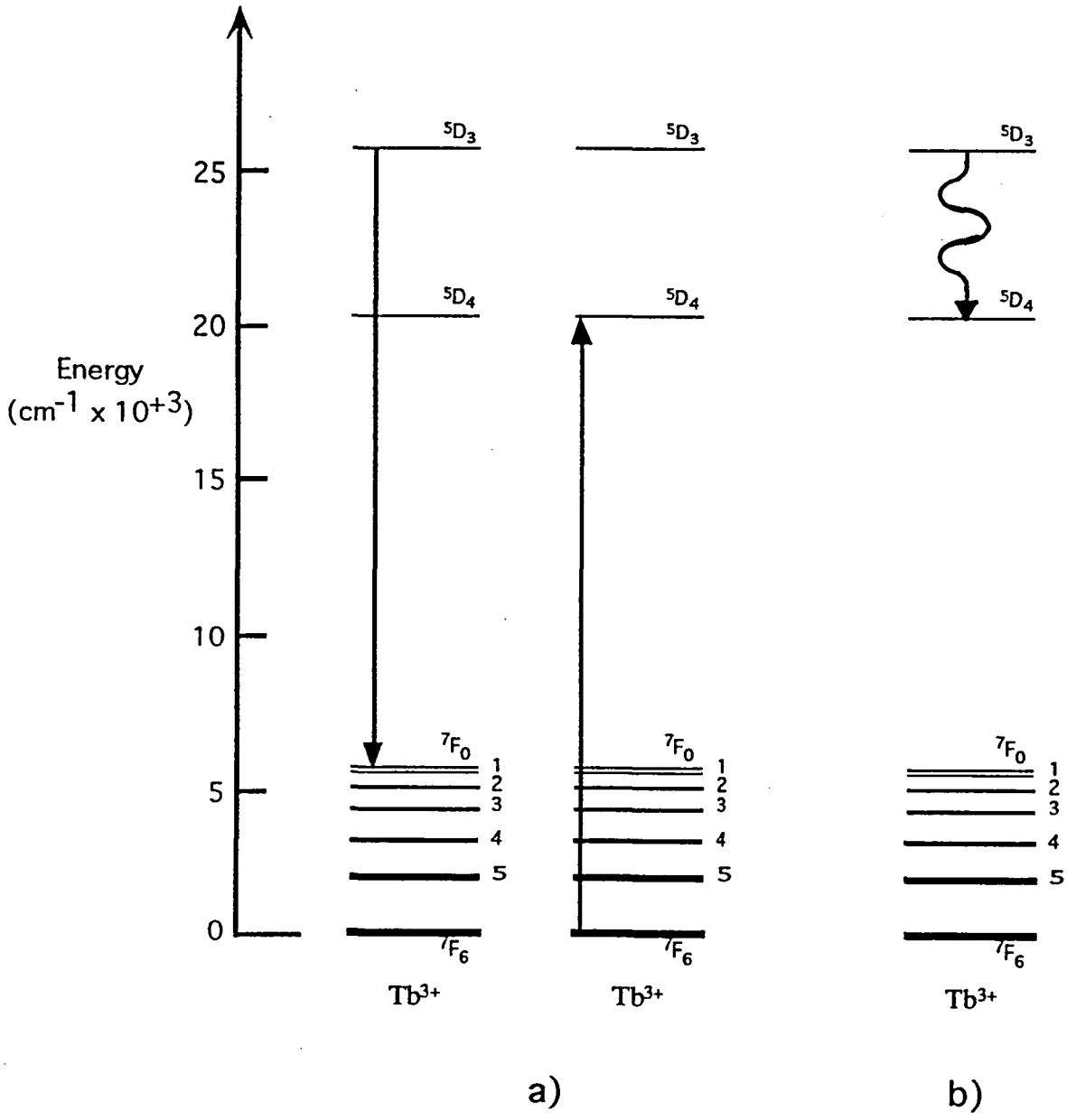

Figure 7. Quenching of $^5D_3$ Luminescence a) Cross-relaxation b) Non-radiative Transition

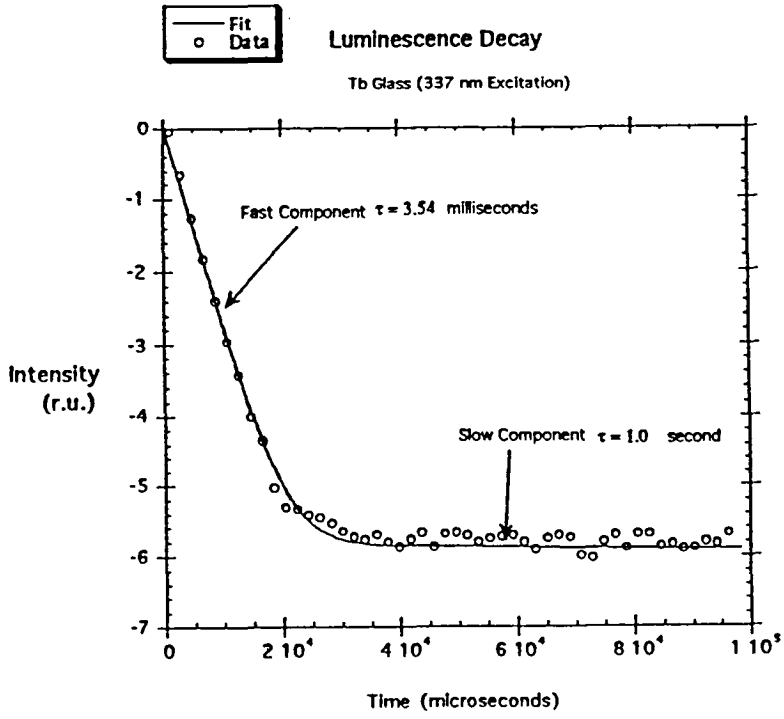

Figure 8. Temporal Response Following UV Excitation

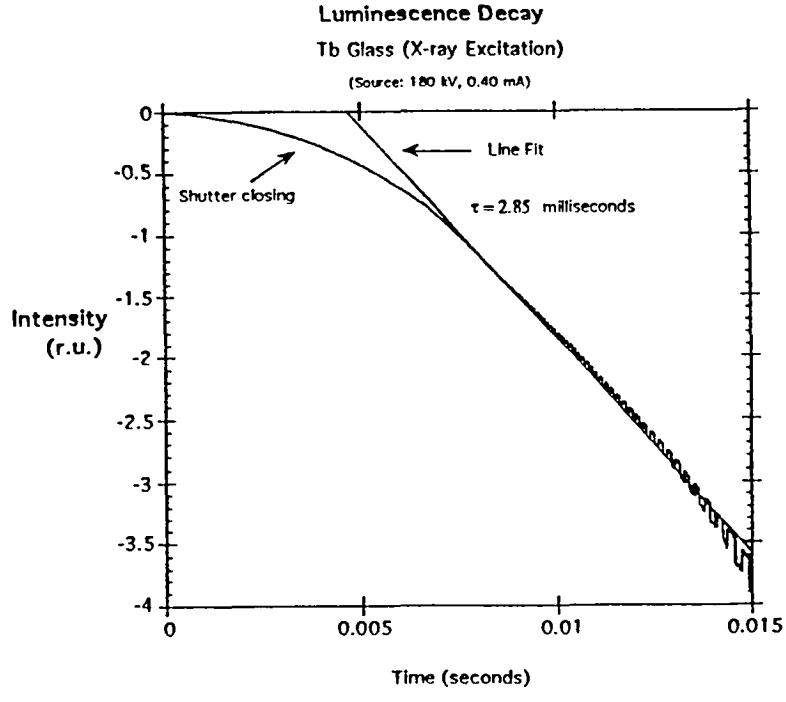

Figure 9. Temporal Response Following X-ray Excitation

RADIATIVE AND NONRADIATIVE TRANSITIONS OF THE RARE-EARTH IONS Tm^{3+} AND Ho^{3+} IN Y3Al5O12 AND LiYF4 †

Brian M. Walsh
Boston College, Dept. of Physics
Chestnut Hill, MA 12167

Guzin Armagan
The College of William and Mary, Dept. of Physics
Williamsburg, VA 23187

Baldassare Di Bartolo
Boston College, Dept. of Physics
Chestnut Hill, MA 02167

Edward A. Modlin
NASA Langley Research Center
Hampton, VA 23681

1. INTRODUCTION

The optical spectra of rare earth ions in solids arise primarily from electric and magnetic dipole transitions between stark split multiplets of the $4f^N$ electronic configuration. Electric dipole transitions are parity forbidden between levels of the $4f^N$ configuration, while those of magnetic dipole origin are allowed. It is known from experiment, however, that the significant contributions to the intensities of most transitions are electric dipole in nature. This is due to the mixing of higher level energy configurations of opposite parity into the $4f^N$ configuration, resulting in a configuration such as $4f^{N-1}5d$. This admixing of configurations is brought about primarily by the odd-order terms in the crystalline stark field. It should be noted, however, that even though magnetic dipole radiation is about six orders of magnitude smaller than electric dipole radiation in free ions, the electric dipole radiation only enters as a perturbation for ions in a crystal. As such, some transitions show a significant magnetic dipole contribution.

Judd [1] and Ofelt [2] developed the theory of forced electric dipole transitions of rare-earth ions. This study is devoted to determining electric dipole transition probabilities and branching ratios for Tm^{3+} and Ho^{3+} ions in Yttrium Aluminum Garnet (YAG) and Yttrium Lithium Fluoride (YLF) using the theory of Judd and Ofelt. The radiative rates determined from the Judd-Ofelt analysis are used with measured lifetimes to find nonradiative rates of relaxation.

† This research was supported by NASA grants NAG-1-955 and NAS1-19656

2. THEORETICAL BACKGROUND

Judd [1] and Ofelt [2] have shown that the line strength from initial J manifold $\langle \psi J|$ and the terminal J´ manifold $|\psi' J'\rangle$ can be expressed as a simple sum of the matrix elements of tensor operators and phenomenological Judd-Ofelt parameters, which is given in Eq. (1).

$$S_{ED} = \sum_{\lambda=2,4,6} \Omega_\lambda \left| \langle \psi J \| U^{(\lambda)} \| \psi' J' \rangle \right|^2 \tag{1}$$

where $\langle \psi J || U^{(\lambda)} || \psi' J' \rangle$ are the doubly reduced matrix elements. These matrix elements vanish for λ odd or $\lambda \geq 6$.The values for the matrix elements can be found in various sources. The most complete set is given by Carnall, Fields and Rajnak [3]. Experience has shown that the matrix elements vary only by small amounts from host to host, so they can be used regardless of the host materials studied. It should be noted that the expression for one-phonon vibronic transitions has an identical form as that of (1) and is incorporated into the Judd-Ofelt parameters. An equation similar to (1) can also be written for the magnetic dipole contribution to the linestrength.

$$S_{MD} = \left(\frac{h}{4\pi mc}\right)^2 \left| \langle \psi J \| L + 2S \| \psi' J' \rangle \right|^2 \tag{2}$$

Equations (1) and (2) are related to the spontaneous emission probability by:

$$A(\psi J; \psi' J') = \frac{64\pi^4 e^2}{3h(2J+1)\bar{\lambda}^3} \left[n \left(\frac{n^2+2}{3n} \right)^2 S_{ED} + n^3 S_{MD} \right] \tag{3}$$

The connection between the theoretical expressions given above and experiment is provided by calculating the linestrengths from absorption measurements. The linestrength is related to measured integrated absorption profiles by the following relation:

$$S_{ED} = \frac{3hc(2J'+1)}{8\pi^3 e^2 \bar{\lambda}} \cdot \frac{1}{n} \left(\frac{3n}{n^2+2} \right)^2 \int_{\text{manifold}} \sigma(\lambda) d\lambda \tag{4}$$

The magnetic dipole contribution is given by the equation:

$$S_{MD} = \frac{3h(2J'+1)\bar{\lambda}}{8\pi^2 mc} \cdot n f_{MD} \tag{5}$$

where f_{MD} is the magnetic dipole oscillator strength. The oscillator strengths have been calculated for many different transitions in rare-earth ions [4]. In cases where the magnetic dipole contributes significantly to the linestrength it must be subtracted from the electric dipole part.

3. EXPERIMENTAL PROCEDURE

Absorption measurements were made on samples of singly doped Tm YAG, Ho YAG, Tm YLF, and Ho YLF. The YLF samples were obtained from Oklahoma State University and were grown by the Bridgman method. The YAG samples were obtained from M.I.T. and were grown by the Czocralski method. The measurements were performed at room temperature on a Perkin-Elmer Lambda9 spectrophotometer across all absorption bands in the wavelength range 300-2300 nm. Spectra for the YLF samples were taken over both polarizations, σ-pol. (E-field perpendicular to c-axis) and π-pol. (E-field parallel to c-axis). YAG is an isotropic crystal, so only one set of absorption measurements were neccesary. The samples were checked for accuracy of manufacturers concentrations by comparison with other available samples. Only one of the samples used showed a discrepancy in concentration. The concentrations of the samples used were 0.75% Tm YAG, 0.5% Ho YAG, 0.5% Tm YLF and 0.44% Ho YLF, the latter being a corrected value. The spectra were also corrected for Fresnel losses at the crystal faces. Mean wavelength values for the manifolds in YAG and YLF were found from energy levels reported in references [5] - [8]. The indices of refraction were calculated from the Sellmeier equation:

$$n^2 = A + \frac{B\lambda^2}{(\lambda^2 - C)} + \frac{D\lambda^2}{(\lambda^2 - E)} \tag{6}$$

with Sellmeier coefficients:

A=1.00000, B= 2.27790, C= 0.01141, D= 0.00000, E= 0.00000 for YAG
A=1.32021, B= 0.84903, C= 0.00876, D=0.53607, E= 134.957 for YLF (P-pol)
A=1.38757, B=0.70757, C= 0.00931, D=0.18849, E=50.9970 for YLF (S-pol)

4. INTEGRATED ABSORPTION PROFILES

YAG is an isotropic crystal, so the evaluation of the bandstrength is simply a matter of summing the absorption cross-section values over wavelength. On the other hand, YLF is an anisotropic crystal which exhibits differing absorption intensities for different polarizations. To take this into account, a modified Beer-Lambert Law for absorption attenuation can be written as:

$$I_t(\lambda) = I_o\left[\frac{2}{3}e^{-\sigma_\perp N\ell} + \frac{1}{3}e^{-\sigma_\parallel N\ell}\right] \tag{7}$$

A spatially averaged Beer-Lambert Law can then be written as:

$$I_t(\lambda) = I_o e^{-\bar{\sigma}(\lambda)N\ell} \tag{8}$$

where,

$$\bar{\sigma}(\lambda) = -\frac{1}{N\ell}\ln\left[\frac{2}{3}e^{-\sigma_\perp N\ell} + \frac{1}{3}e^{-\sigma_\parallel N\ell}\right] \tag{9}$$

Integrating (9) over the entire band gives:

$$\bar{\Gamma} = -\frac{1}{N\ell} \int_{manifold} \ln\left[\frac{2}{3}e^{-\sigma_\perp N\ell} + \frac{1}{3}e^{-\sigma_\parallel N\ell}\right] d\lambda \qquad (10)$$

The above equation was used for the calculation of integrated absorption profiles in YLF.

5. THE FITTING PROCEDURE

A computer program was written to perform a least squares fit between the experimental linestrengths found from (4) and the theoretical values from (1). The procedure is the same as outlined by Krupke [9]. If the three Judd-Ofelt parameters are made to form a column vector Ω, and the doubly reduced matrix elements form an n x m matrix **M**, where n is the number of transitions to fit, and m is the number of parameters to vary in the fit (in this case m=3 corresponding to the 3 Judd-Ofelt parameters), then the theoretical linestrength can then be written as a 1 x n column vector. This can be expressed as:

$$\mathbf{S}_t = \mathbf{M}\Omega \qquad (11)$$

The set of J-O parameters that minimizes the sum of the squares of the differences between the theoretical and experimental linestrengths is found from matrix algebra to be:

$$\Omega^o = (\mathbf{M}^\dagger\mathbf{M})^{-1}\mathbf{M}^\dagger\mathbf{S}_m \qquad (12)$$

where $\mathbf{M}^\dagger$ is the adjoint of matrix **M**. The measure of the quality of the fit is given by the root mean deviation, expressed as:

$$\text{RMS } \Delta S = [\ \Sigma(\Delta S)^2/(\#\text{ Transitions to fit} - \#\text{ of parameters to fit})]^{1/2}$$

The results of this fitting procedure are presented in Tables 1 - 4.

6. MULTIPHONON RATES

The total lifetime τ of excited states in YAG and YLF were measured, and the radiative decay times from the Judd-Ofelt theory were used to find the nonradiative decay times according to:

$$\frac{1}{\tau_{nr}} = \frac{1}{\tau} - \frac{1}{\tau_r} \qquad (13)$$

The measured lifetimes in Holmium YAG and YLF were measured at low temperature (20K) and are given in Table 5.

Table 5. Measured lifetimes in YAG and YLF

Ion	manifold	τ_{YAG} (ms)	τ_{YLF} (ms)
Ho	5F5	0.4	50
Ho	5S2,5F4	3.7	265
Ho	5I6	45	2500
Ho	5I7	7000	14500

The multiphonon rates are seen to follow an exponential function which depends on the energy gap between the lowest level of an excited manifold and the highest lying level of the next lower manifold. The multiphonon rates are graphed with energy gap in Figure 1. The multiphonon rates can be modeled as:

$$k_{nr} = (1+m)^p \cdot \beta e^{-\alpha \Delta E} \tag{14}$$

where,

$$m = [\exp(\hbar\omega_{max} / kT) - 1]^{-1} \quad \text{and} \quad p = \Delta E / \hbar\omega_{max}$$

The value of m accounts for thermally stimulated emission of phonons at higher temperatures, p is the number of phonons participating in the transition, ΔE is the energy gap from the lowest crystal field level of the excited manifold and the upper crystal field level of the next lower lying manifold, and $\hbar\omega_{max}$ is the maximum energy of the phonons.

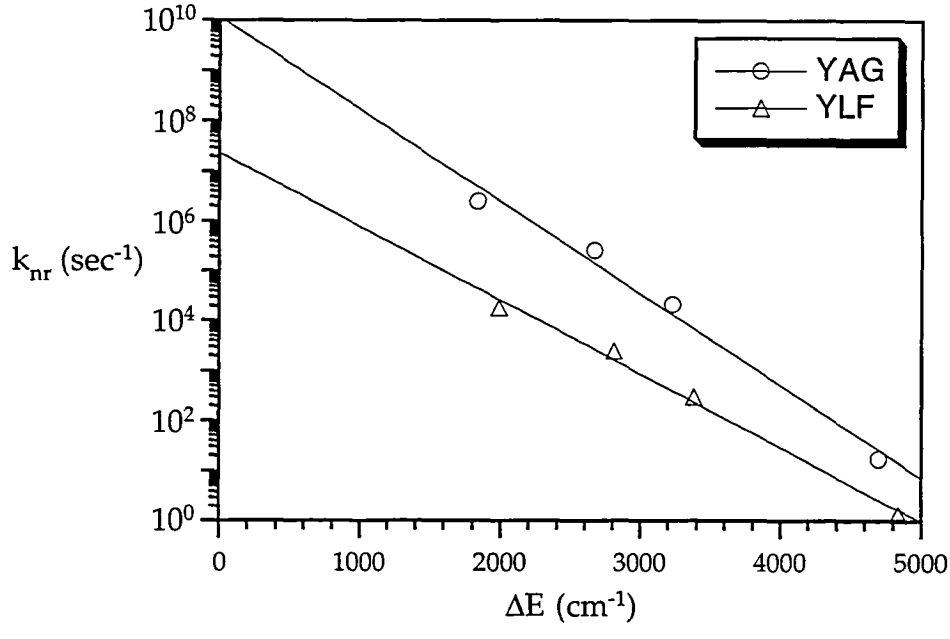

Figure 1. Multiphonon rate vs. energy gap

An exponential fit to the data allowed a determination of the constants α and β to be made. α and β are assumed to be characteristic of the crystal lattice only. It is also assumed that the rate of multiphonon nonradiative transitions is dominated by processes of lowest order in p. As a result, $\omega_{max.}$ is taken as the maximum phonon frequency or a frequency of some effective phonon mode with a value smaller than the maximum value which dominates the transitions. A comparison of the experimental and modeled multiphonon rates in YLF and YAG is given in Tables 6 and 7.

Table 6 Multiphonon Rates in YLF

ion	band	ΔE	$k_{nr}^{meas}(sec^{-1})$	$k_{nr}^{model}(sec^{-1})$
Ho	5F5	1985	$1.87x10^4$	$2.76x10^4$
Ho	5I5	2445	—	$5.78x10^3$
Ho	5S2	2812	$2.44x10^3$	$1.66x10^3$
Ho	5I6	3377	304	243
Ho	5I7	4833	1.37	1.72

Table 7 Multiphonon Rates in YAG

ion	band	ΔE	$k_{nr}^{meas}(sec^{-1})$	$k_{nr}^{model}(sec^{-1})$
Ho	5F5	1837	$2.49x10^6$	$5.27x10^6$
Ho	5I5	2349	—	$6.14x10^5$
Ho	5S2	2665	$2.66x10^5$	$1.62x10^5$
Ho	5I6	3228	$2.19x10^4$	$1.53x10^4$
Ho	5I7	4692	18	32

7. RESULTS AND CONCLUSIONS

Based on the multiphonon rates presented in Tables 5 and 6 we were able to determine the host dependent constants appearing in equation (14). For YAG, using a phonon energy of 700 cm^{-1}, it was found that α=.00428 and $\beta=8.7887x10^9$. For YLF, using a phonon energy of 560 cm^{-1}, it was found that α=.00315 and $\beta=1.1137x10^7$. The critical energy gap below which nonradiative rates dominate the transition is estimated to be 3500 cm^{-1} in YAG and 2800 cm^{-1} in YLF. This corresponds to the emission of 5 or less phonons in both crystals.

As expected, the logarithm of the multiphonon rate shows an approximately linear dependence with energy gap. This is in agreement with the general criterion that the relative contributions of radiative and nonradiative processes to the decay of an excited state depends on the size of the energy gap and the number of phonons necessary to bridge it. This indicates that the model for nonradiative decay rates can be used for order of magnitude estimates of multiphonon rates.

8. REFERENCES

[1] B.R. Judd, Phys. Rev. **127**, 750 (1962)
[2] G.S. Ofelt, J. Chem. Phys. **37**, 511 (1962)
[3] W.T. Carnall, P.R. Fields, K. Rajnak, J. Chem. Phys. **49**, 4424 (1968)
[4] W.T. Carnall, P.R. Fields, K. Rajnak, J. Chem. Phys. **49**, 4412 (1968)
[5] H.P. Jenssen, A Linz, R.P. Leavitt, C.A. Morrison, Phys. Rev. **B11**, 92 (1975)
[6] N. Karayanis, D.E. Wortman and H.P. Jenssen, J. Phys. Chem. Solids 37, 675 (1976)
[7] J. Gruber, et. al., Phys. Rev. **B11**, 9464 (1989)
[8] J. Gruber, et. al., J. Appl. Phys. **69**, 8183 (1991)
[9] W. F. Krupke, IEEE J. Quantum Elec. **QE-7**, 153 (1971)

Table 1 Judd-Ofelt Fit for YAG: Tm

Transition from 5I8	$[U^{(2)}]^2$	$[U^{(4)}]^2$	$[U^{(6)}]^2$	λ(nm)	S meas. $x10^{-20}$ cm^2	S theor. $x10^{-20}$ cm^2
1D2	0	0.3156	0.0928	357	0.5718	0.6035
1G4	0.0483	0.0748	0.0125	469	0.2617	0.1902
3F2+3F3	0	0.3164	1.0992	677	1.6377	1.6239
3H4	0.2373	0.1090	0.5947	784	1.0334	1.0570
3F4	0.5375	0.7261	0.2382	1725	2.0331	2.0291

Judd-Ofelt Parameters: $\Omega_2 = 1.1752$ $\Omega_4 = 1.6146$ $\Omega_6 = 1.0126$
Root Mean Square deviation: $\delta = 5.8612E-02$

Transition	λ(nm)	S theor. $x10^{-20}$ cm^2	A_{ED} (sec^{-1})	A_{MD} (sec^{-1})	β	τ (μs)
1D2 - 1G4	1535.6	0.512	115.43		0.005	
1D2 - 3F2	787.3	0.569	967.78		0.042	
1D2 - 3F3	750.2	0.301	593.47		0.026	
1D2 - 3H4	656.2	0.392	1163.63		0.051	43
1D2 - 3H5	516.4	0.021	129.55		0.006	
1D2 - 3F4	449.4	0.839	8053.31		0.350	
1D2 - 3H6	357.2	0.600	11981.52		0.521	
1G4 - 3F2	1615.5	0.180	19.34		0.007	
1G4 - 3F3	1466.7	0.473	67.95		0.024	
1G4 - 3H4	1145.7	0.101	30.66		0.011	
1G4 - 3H5	778.1	0.672	657.95		0.235	358
1G4 - 3F4	635.4	0.617	1122.16		0.401	
1G4 - 3H6	465.5	0.188	897.68		0.321	
3F2 - 3F3	15929.2	0.126	0.03		0.000	
3F2 - 3H4	3940.1	0.675	8.96		0.006	
3F2 - 3H5	1501.1	1.059	255.40		0.182	712
3F2 - 3F4	1047.3	0.500	357.79		0.255	
3F2 - 3H6	653.9	0.261	783.21		0.557	
3F3 - 3H4	5235.6	0.918	3.71		0.001	
3F3 - 3H5	1657.3	1.299	166.12		0.059	
3F3 - 3F4	1121.1	0.171	71.28		0.025	356
3F3 - 3H6	681.9	1.362	2564.50		0.914	
3H4 - 3H5	2424.8	0.792	25.09		0.021	
3H4 - 3F4	1426.5	0.582	90.95		0.078	857
3H4 - 3H6	784.0	1.099	1051.01		0.901	
3H5 - 3F4	3465.0	1.223	10.85		0.038	
3H5 - 3H6	1158.6	1.145	274.15	32.7	0.962	3147
3F4 - 3H6	1740.6	2.044	175.44		1.000	5700

Table 2 Judd-Ofelt Fit for YLF: Tm

Transition from 5I8	$[U^{(2)}]^2$	$[U^{(4)}]^2$	$[U^{(6)}]^2$	λ(nm)	S meas. $x10^{-20}$ cm^2	S theor. $x10^{-20}$ cm^2
1D2	0	0.3156	0.0928	357	0.7209	0.7065
1G4	0.0483	0.0748	0.0125	469	0.2693	0.2371
3F2+3F3	0	0.3164	1.0992	672	1.7981	1.8047
3H4	0.2373	0.1090	0.5947	784	1.2633	1.2504
3F4	0.5375	0.7261	0.2382	1725	2.5347	2.5433

Judd-Ofelt Parameters: Ω_2 = 1.6673 Ω_4 = 1.9184 Ω_6 = 1.0897
Root Mean Square deviation: δ = 2.6938E-02

Transition	λ(nm)	S theor. $x10^{-20}$ cm^2	A_{ED} (sec^{-1})	A_{MD} (sec^{-1})	β	τ (μs)
1D2 - 1G4	1486.3	0.675	79.18		0.006	
1D2 - 3F2	788.3	0.693	587.65		0.044	
1D2 - 3F3	745.2	0.401	387.33		0.029	
1D2 - 3H4	657.0	0.473	669.11		0.050	75
1D2 - 3H5	504.1	0.023	71.49		0.005	
1D2 - 3F4	450.4	1.143	5092.22		0.384	
1D2 - 3H6	357.1	0.702	6373.78		0.481	
1G4 - 3F2	1633.7	0.211	10.63		0.007	
1G4 - 3F3	1494.3	0.528	34.75		0.022	
1G4 - 3H4	1177.4	0.113	15.27		0.010	
1G4 - 3H5	762.8	0.755	377.59		0.244	645
1G4 - 3F4	646.2	0.729	602.71		0.389	
1G4 - 3H6	470.1	0.235	509.51		0.329	
3F2 - 3F3	17513.1	0.151	0.02		0.000	
3F2 - 3H4	4215.9	0.869	4.30		0.006	
3F2 - 3H5	1431.0	1.192	160.91		0.207	1289
3F2 - 3F4	1069.1	0.671	218.25		0.281	
3F2 - 3H6	660.0	0.281	392.29		0.506	
3F3 - 3H4	5552.5	1.082	1.49		0.001	
3F3 - 3H5	1558.4	1.708	127.39		0.084	
3F3 - 3F4	1138.6	0.185	35.61		0.023	660
3F3 - 3H6	685.9	1.532	1351.08		0.891	
3H4 - 3H5	2166.4	0.943	20.21		0.030	
3H4 - 3F4	1432.3	0.701	52.46		0.078	1480
3H4 - 3H6	882.5	1.302	603.06		0.892	
3H5 - 3F4	4226.5	1.373	3.06		0.023	
3H5 - 3H6	1225.0	1.316	129.05	46.0	0.977	5614
3F4 - 3H6	1725.0	2.499	106.66		1.000	9375

Table 3 Judd-Ofelt Fit for YAG: Ho

Transition from 5I8	$[U^{(2)}]^2$	$[U^{(4)}]^2$	$[U^{(6)}]^2$	λ(nm)	S meas. $x10^{-20}$ cm^2	S theor. $x10^{-20}$ cm^2
3K6+3F4	0.0026	0.1262	0.0073	333	0.2644	0.2864
3L9+5G3	0.0185	0.0052	0.1669	345	0.2485	0.2671
3D2+3H6+G5	0.2155	0.1969	0.1679	361	0.8635	0.7171
3K7+5G4	0.0058	0.0361	0.0697	386	0.1441	0.1851
3G5	0	0.5338	0.0002	420	1.0358	1.1634
5F1+5G6	1.5201	0.8410	0.1411	448	2.2649	2.2843
3K8	0.0208	0.0334	0.1535	466	0.3498	0.3086
3F2	0	0	0.2041	475	0.3213	0.3092
3F3	0	0	0.3464	487	0.5124	0.5248
5F4+5S2	0	0.2392	0.9339	543	2.0695	1.9363
5F5	0	0.4250	0.5687	650	1.8771	1.7878
5I5	0	0.0100	0.0936	886	0.0903	0.1636
5I6	0.0084	0.0386	0.6921	1162	0.8616	1.1341

Judd-Ofelt Parameters: $\Omega_2 = 0.1565$ $\Omega_4 = 2.1790$ $\Omega_6 = 1.5152$
Root Mean Square deviation: $\delta = 8.5854E-02$

Transition	λ(nm)	S theor. $x10^{-20}$ cm^2	A_{ED} (sec^{-1})	A_{MD} (sec^{-1})	β	τ (μs)
5F4 - 5S2	87719.3	0.040	0.00		0.000	
5F4 - 5F5	3045.1	0.244	3.89		0.001	
5F4 - 5I4	1920.9	0.443	28.27		0.005	
5F4 - 5I5	1361.8	0.992	178.28		0.029	
5F4 - 5I6	993.7	0.820	381.59		0.063	165
5F4 - 5I7	735.0	0.482	561.59		0.093	
5F4 - 5I8	535.7	1.596	4916.25		0.810	
5S2 - 5F5	3145.6	0.029	0.76		0.000	
5S2 - 5I4	1963.9	0.485	52.05		0.015	
5S2 - 5I5	1383.3	0.170	52.55		0.015	
5S2 - 5I6	1005.1	0.278	225.41		0.065	
5S2 - 5I7	741.2	0.621	1267.87		0.365	288
5S2 - 5I8	535.7	0.344	1871.19		0.539	
5F5 - 5I4	5202.9	0.019	0.05		0.000	
5F5 - 5I5	2463.7	0.310	7.66		0.002	
5F5 - 5I6	1475.1	1.023	118.20		0.037	
5F5 - 5I7	968.9	1.379	567.25		0.178	314
5F5 - 5I8	650.0	1.794	2488.87		0.539	
5I4 - 5I5	4679.5	1.653	7.27		0.051	
5I4 - 5I6	2058.9	1.068	55.30		0.390	
5I4 - 5I7	1190.6	0.245	65.99		0.466	7075
5I4 - 5I8	742.8	0.012	13.15		0.093	
5I5 - 5I6	3676.5	1.246	9.26		0.041	
5I5 - 5I7	1596.9	1.396	127.07		0.564	4437
5I5 - 5I8	883.0	0.163	89.07		0.395	
5I6 - 5I7	2823.3	1.707	23.69		0.094	
5I6 - 5I8	1162.1	1.133	227.50		0.906	3981
5I7 - 5I8	1975.1	2.603	91.63	34.0	1.000	7977

Table 4 Judd-Ofelt Fit for YLF: Ho

Transition from 5I8	$[U^{(2)}]^2$	$[U^{(4)}]^2$	$[U^{(6)}]^2$	λ(nm)	S meas. $x10^{-20}$ cm^2	S theor. $x10^{-20}$ cm^2
3K6+3F4	0.0026	0.1262	0.0073	334	0.1421	0.2146
3L9+5G3	0.0185	0.0052	0.1669	345	0.2118	0.2275
3D2+3H6+5G5	0.2155	0.1969	0.1679	360	0.9189	0.6858
3K7+5G4	0.0058	0.0361	0.0697	385	0.1796	0.1483
3G5	0	0.5338	0.0002	418	0.9251	0.8620
5F1+5G6	1.5201	0.8410	0.1411	448	2.6378	2.6704
3K8	0.0208	0.0334	0.1535	467	0.2814	0.2583
3F2	0	0	0.2041	473	0.2789	0.2510
3F3	0	0	0.3464	486	0.4729	0.4260
5F4+5S2	0	0.2392	0.9339	540	1.6620	1.5348
5F5	0	0.4250	0.5687	645	1.2203	1.3856
5I5	0	0.0100	0.0936	886	0.0550	0.1312
5I6	0.0084	0.0386	0.6921	1175	0.8090	0.9198

Judd-Ofelt Parameters: $\Omega_2 = 0.7483$ $\Omega_4 = 1.6168$ $\Omega_6 = 1.2269$
Root Mean Square deviation: $\delta = 1.0909E-01$

Transition	λ(nm)	S theor. $x10^{-20}$ cm^2	A_{ED} (sec^{-1})	A_{MD} (sec^{-1})	β	τ (μs)
5F4 - 5S2	67567.7	0.030	0.00		0.000	
5F4 - 5F5	3173.6	0.305	2.03		0.001	
5F4 - 5I4	1887.5	0.356	11.58		0.005	
5F4 - 5I5	1386.8	0.786	73.99		0.033	442
5F4 - 5I6	985.8	0.626	144.52		0.064	
5F4 - 5I7	737.9	0.361	199.62		0.088	
5F4 - 5I8	536.1	1.258	1832.72		0.809	
5S2 - 5F5	3330.0	0.022	0.23		0.000	
5S2 - 5I4	1941.7	0.390	20.94		0.016	
5S2 - 5I5	1353.9	0.138	21.95		0.016	
5S2 - 5I6	1000.4	0.223	88.55		0.067	751
5S2 - 5I7	746.0	0.504	485.35		0.365	
5S2 - 5I8	540.4	0.279	714.38		0.537	
5F5 - 5I4	4657.7	0.015	0.02		0.000	
5F5 - 5I5	2281.5	0.252	3.77		0.003	
5F5 - 5I6	1430.0	0.818	50.31		0.041	
5F5 - 5I7	961.4	1.080	219.84		0.180	820
5F5 - 5I8	645.0	1.390	944.96		0.775	
5I4 - 5I5	4472.3	1.342	3.05		0.056	
5I4 - 5I6	2063.6	0.864	21.44		0.396	
5I4 - 5I7	1211.5	0.198	24.57		0.454	18496
5I4 - 5I8	748.7	0.009	5.01		0.093	
5I5 - 5I6	3831.4	1.013	3.08		0.039	
5I5 - 5I7	1661.7	1.132	44.24		0.553	12502
5I5 - 5I8	899.3	0.131	32.66		0.408	
5I6 - 5I7	2934.3	1.384	8.15		0.086	
5I6 - 5I8	1175.1	0.919	86.46		0.914	10570
5I7 - 5I8	1960.0	2.107	36.67	21.4	1.000	17500

THERMAL LINE SHIFT AND BROADENING OF Ho^{3+} IN $Y_3Al_5O_{12}$ AND $Lu_3Al_5O_{12}$

Elizabeth R. Snoke† and Guzin Armagan
The College of William and Mary, Dept. of Physics, Williamsburg, VA 23185

Gary W. Grew and Norman P. Barnes
NASA Langley Research Center, MS 474, Hampton, VA 23681

Brian M. Walsh
Department of Physics, Boston College, Chestnut Hill, MA 02167

I. INTRODUCTION

The interaction between the active ion and the host lattice manifests itself in two distinct ways : the static interaction with the crystal field that causes the splitting of the free ion energy levels and the active interaction through the surrounding phonon system that produces temperature dependent characteristics in the optical spectrum of the ion (e.g., line broadening and line shift). The strength of the splitting depends heavily on the electronic configuration of the atom.

The model given by McCumber and Sturge [1] describes the thermal effects on line width and position above 77 K with Raman scattering of Debye model phonons. These processes predict a Lorentzian line shape. However below 77 K the principal contributions are from crystal inhomogeneities that result in a Gaussian line shape.

We have investigated the experimental Stark levels as well as the thermal effects on the line width and the position of trivalent holmium ions in both yttrium aluminum garnet, $Y_3Al_5O_{12}$ (YAG) and lutetium aluminum garnet, $Lu_3Al_5O_{12}$ (LuAG) crystals. We have compared the Stark levels of the $^5I_6$ state, and the thermal line shift and broadening of an isolated transition (Z2 -> X13) between the $^5I_8$ and $^5I_6$ Stark levels in these crystals. This transition occurs in the near infrared region at approximately 1117 nm.

†University of North Carolina at Chapel Hill, Department of Physics, Chapel Hill, NC 27514.

II. SAMPLES AND EXPERIMENTAL SETUP

The samples used in this study were single crystals of LuAG and YAG with low doping percentages (0.5 or 2 %) of holmium. The Cary 5E spectrophotometer recorded the transmission spectra for both Ho:YAG and Ho:LuAG in the wavelength region of 1110 -1150 nm, corresponding to the $^5I_8$ -> $^5I_6$ transition. The sample was placed in a cold finger and cooled to 8 K with a RMC Cryosystems cryogenic compressor system. The temperature of the sample was varied with Lake Shore 320 autotuning temperature controller from 8 K to 300 K.

III. EXPERIMENTAL RESULTS AND OBSERVATIONS

We have determined the Stark levels of the $^5I_6$ transition by measuring the transmission spectra at 8 K and 30 K. The transitions take place mainly from the two lowest Stark levels (Z1 and Z2) of the $^5I_8$ manifold to the 13 Stark levels (X1-X13) of the $^5I_6$ manifold at these temperatures. The change in the line intensity of transitions from the Z1 and Z2 levels with increasing temperature follows the Boltzmann statistics. Table 1 lists the Stark levels of the $^5I_6$ manifold of Ho^{3+} in YAG and LuAG. Figures 1 and 2 show the transmission spectra of Ho(0.5%) at 8 K for YAG and LuAG, respectively.

We can make the following observations on these experimental results :

1) The band width of the $^5I_6$ manifold is wider in YAG than in LuAG.
2) The width of each individual $^5I_6$ Stark level is narrower in YAG than in LuAG.
3) Comparison of the positions of the $^5I_6$ Stark level for YAG and LuAG indicates differences of up to 10.5 cm^{-1}.

We have also examined the thermal effects on the line width and line shift of the Z2 -> X13 transition. This transition was chosen because it is well separated from the other transitions in both crystals. Figures 3 and 4 show the comparison of thermal broadening and line shift between the YAG and LuAG crystals, respectively.

When examining the thermal dependence of the Z2 -> X13 transition, we can make the following observations:

1) The wavelength of the transition shifts towards longer wavelengths as temperature increases.
2) The width of the line broadens as temperature increases.
3) The line position and the line width are independent of temperature below ~70 K for LuAG and ~100 K for YAG.

4) The line shape fits well with the Lorentzian function due to the homogeneous broadening at high temperatures.

5) The Gaussian contribution to the line shape is more evident at low temperatures.

6) Thermal broadening is greater on the lower wavelength side of the line, giving an asymmetric line shape.

7) Thermal shift and broadening of the LuAG line start at lower temperatures than for the YAG line.

8) The rate at which the line width changes with temperature is twice as fast for LuAG as for YAG.

9) The rate at which the line position shifts with temperature is 3.7 times faster for LuAG than for YAG.

Since it is the interaction between the ion and the surrounding phonon system which produces the temperature dependent characteristics in the optical spectrum of the ion, the wider line width and the stronger thermal dependence of line width and line shift of Ho transitions indicate a lower phonon energy in LuAG than in YAG.

REFERENCE

[1] D.E. McCumber and M.D. Sturge, "Line width and temperature shift of the R lines in Ruby," J. Appl. Phys., 34, 1682 (1963).

Acknowledgements

This research is supported by NAS-19656 and NAG-1-955 NASA Grants, and PHY-9300205 NSF Grant.

Table 1. Stark levels of $^5I_6$ manifold of Ho^{3+} in YAG and LuAG. ΔE is the energy difference of Stark levels between YAG and LuAG.

Transition	Ho:YAG(cm^{-1})	Ho:LuAG(cm^{-1})	ΔE (cm^{-1})
Z1 -> X1	8739.5	8743.8	-4.3
Z1 -> X2	8743.6	8748.3	-4.7
Z1 -> X3	8747.6	8752.9	-5.3
Z1 -> X4	8768.3	8762.6	5.7
Z1 -> X5	8773.3	8767.1	6.3
Z1 -> X6	8776.2	8770.9	5.3
Z1 -> X7	8822.9	8816.0	6.9
(Z2 -> X7)	(8819.0)	(8811.5)	
Z1 -> X8	8845.4	8845.1	0.3
(Z2 -> X8)	(8841.3)	(8840.8)	
Z1 -> X9	8861.1	8859.1	2.0
(Z2 -> X9)	(8857.2)	(8854.7)	
Z1 -> X10	8874.0	8878.2	-1.3
Z1 -> X11	8881.4	8882.7	
(Z2 -> X11)	(8977.1)		
Z1 -> X12	8944.9	8934.4	10.5
(Z2 -> X12)	(8940.8)	(8930.0)	
Z1 -> X13	8959.8	8955.0	4.8
(Z2 -> X13)	(8955.8)	(8950.5)	

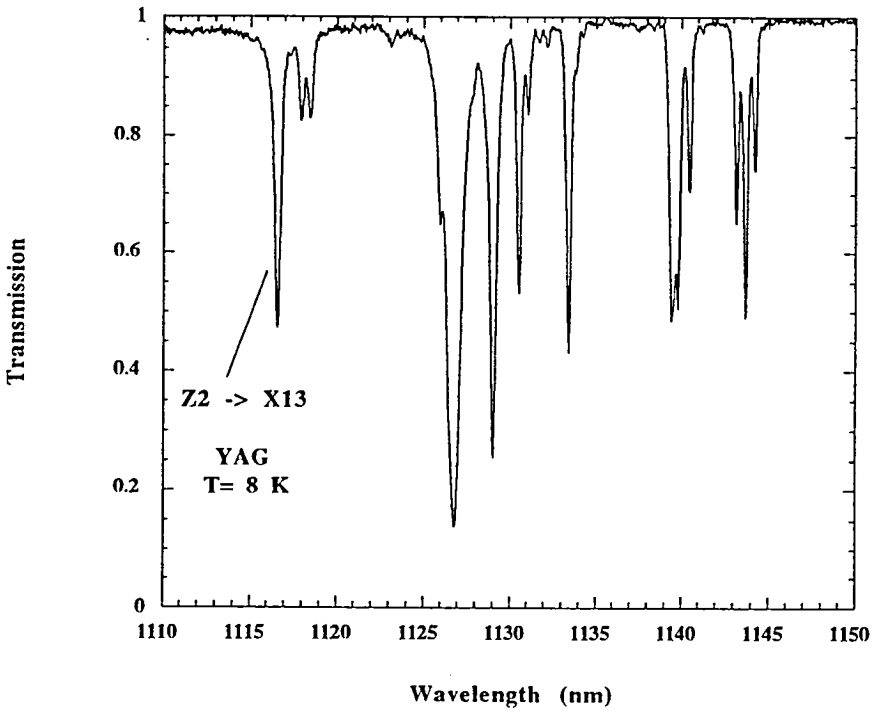

Figure 1. Transmission spectrum of $^5I_8$ -> $^5I_6$ transition of holmium in Ho(.5%):YAG at 8 K.

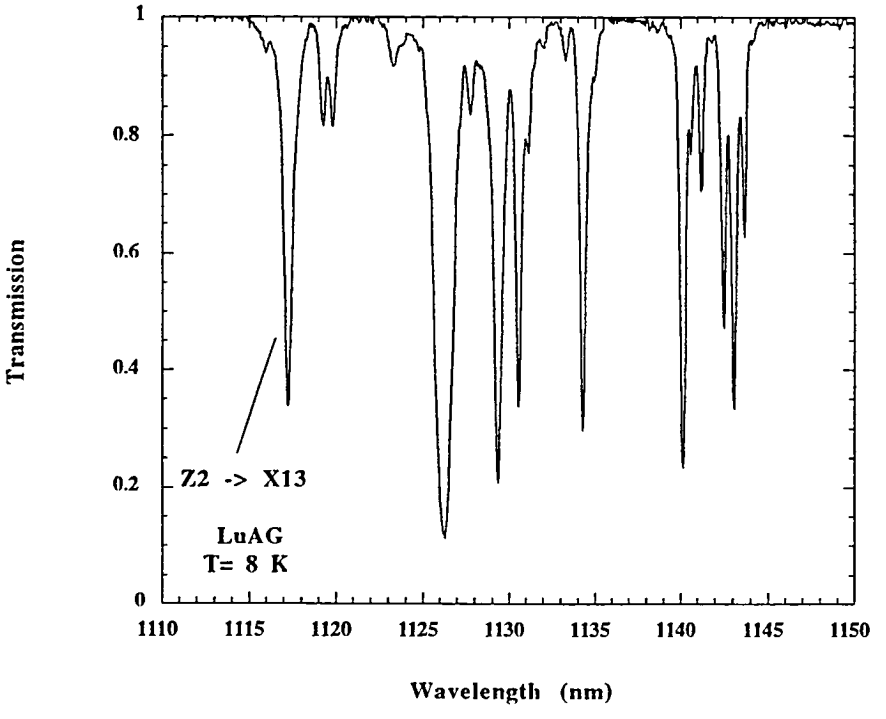

Figure 2. Transmission spectrum of $^5I_8$ -> $^5I_6$ transition of holmium in Ho(.5%):LuAG at 8 K.

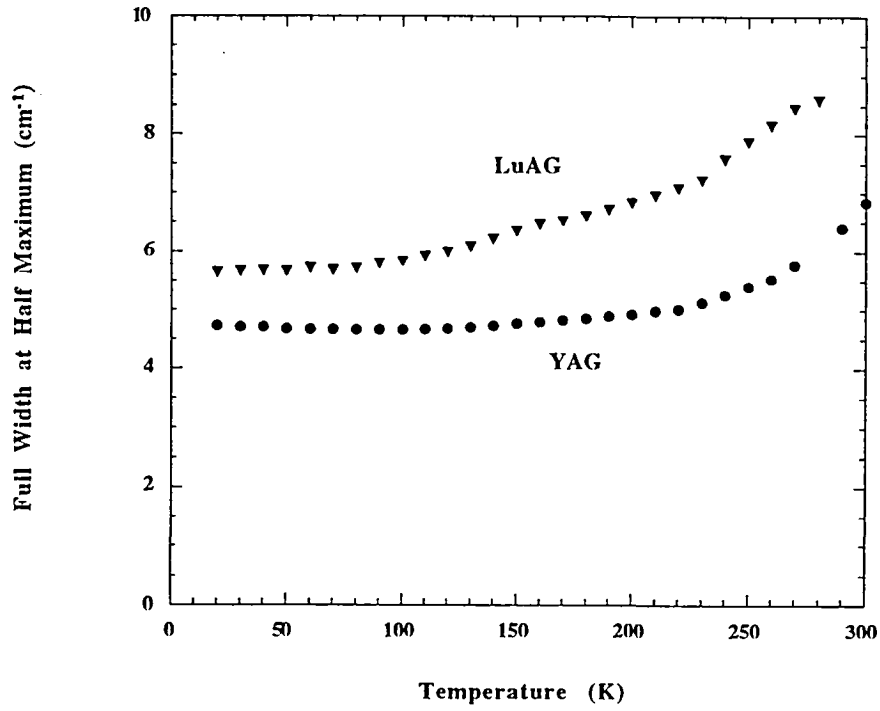

Figure 3. Comparison of thermal broadening of the Ho Z2 -> X13 transition in YAG and LuAG.

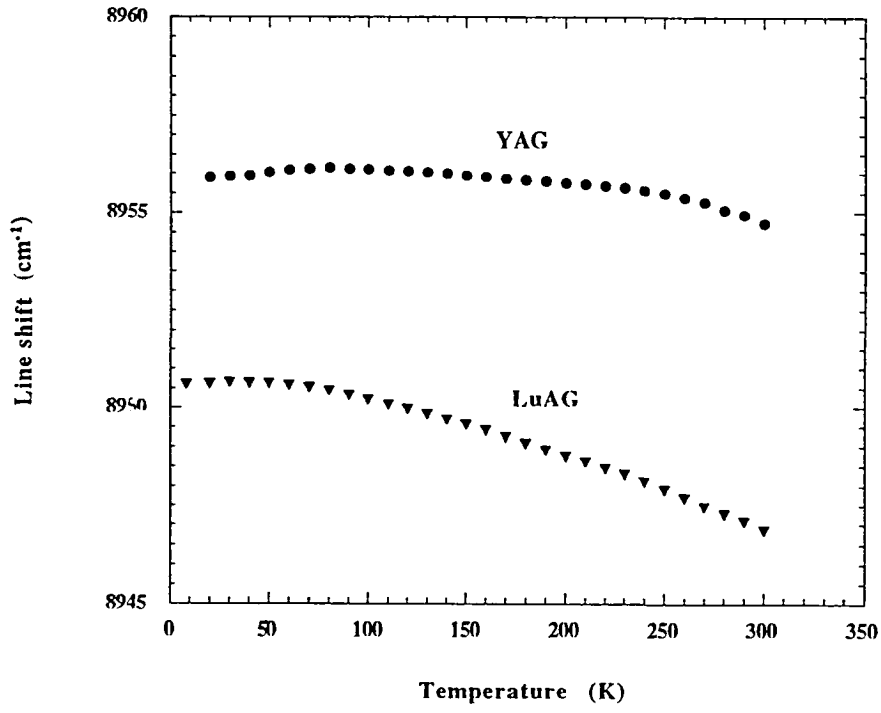

Figure 4. Comparison of thermal line shift of the Ho- Z2 -> X13 transition in YAG and LuAG.

REPORT DOCUMENTATION PAGE

Form Approved
OMB No. 0704-0188

1. AGENCY USE ONLY *(Leave blank)*	2. REPORT DATE	3. REPORT TYPE AND DATES COVERED
	October 1995	Conference Publication

4. TITLE AND SUBTITLE
Second Annual Research Center for Optical Physics (RCOP) Forum

5. FUNDING NUMBERS
410-10-04-01

6. AUTHOR(S)
Frank Allario and Doyle Temple, Editors

7. PERFORMING ORGANIZATION NAME(S) AND ADDRESS(ES)
NASA Langley Research Center
Hampton, VA 23681-0001

8. PERFORMING ORGANIZATION REPORT NUMBER
L-17505

9. SPONSORING/MONITORING AGENCY NAME(S) AND ADDRESS(ES)
National Aeronautics and Space Administration
Washington, DC 20546-0001, and
Hampton University
Hampton, VA 23668

10. SPONSORING/MONITORING AGENCY REPORT NUMBER
NASA CP-3314

11. SUPPLEMENTARY NOTES
Doyle Temple: Director, Research Center for Optical Physics, Hampton University, Hampton, VA 23668.

12a. DISTRIBUTION/AVAILABILITY STATEMENT
Unclassified–Unlimited
Subject Category—74

12b. DISTRIBUTION CODE

13. ABSTRACT *(Maximum 200 words)*

The Research Center for Optical Physics (RCOP) held its Second Annual Forum on September 23–24, 1994. The forum consisted of two days of technical sessions with invited talks, submitted talks, and a student poster session. Dr. Demetrius Venable, Executive Vice President and Provost, delivered the welcome and opening remarks. He gave a brief history of the research programs in the physics department and their relationship to RCOP. Following the opening remarks, Dr. Frank Allario, Chairman of the Technical Advisory Committee, gave the technical overview of the collaboration between RCOP and NASA Langley; Dr. Doyle Temple, Director of RCOP, gave a review of technical programs in RCOP and the mission of the program.

Participants in the technical sessions included students and researchers from CCNY/CUNY, Fisk University, Georgia Institute of Technology, Hampton University, University of Maryland, the University of Michigan, NASA Langley Research Center, North Carolina A&T State University, Steven's Institute of Technology, and NAWC-Warminster. A speech by Dr. Lynwood P. Randolph, the Manager of Information Standards at NASA Headquarters, highlighted the closing of the banquet. This document is a compilation of the invited and contributed talks and student posters.

14. SUBJECT TERMS	15. NUMBER OF PAGES
Lasers; Fiber optics; Electro-optical materials; Remote sensing	121
	16. PRICE CODE: A06

17. SECURITY CLASSIFICATION OF REPORT	18. SECURITY CLASSIFICATION OF THIS PAGE	19. SECURITY CLASSIFICATION OF ABSTRACT	20. LIMITATION OF ABSTRACT
Unclassified	Unclassified	Unclassified	Unlimited